

1  
2  
3  
4  
5

# COMPENSATED CONVEXITY METHODS FOR APPROXIMATIONS AND INTERPOLATIONS OF SAMPLED FUNCTIONS IN EUCLIDEAN SPACES: APPLICATIONS TO CONTOUR LINES, SPARSE DATA AND INPAINTING\*

KEWEI ZHANG<sup>†</sup>, ELAINE CROOKS<sup>‡</sup>, AND ANTONIO ORLANDO<sup>§</sup>

6     **Abstract.** This paper is concerned with applications of the theory of approximation and interpolation based on compensated  
7 convex transforms developed in [55]. We apply our methods to (i) surface reconstruction starting from the knowledge of finitely many  
8 level sets (or ‘contour lines’); (ii) scattered data approximation; (iii) image inpainting. For (i) and (ii) our methods give interpolations.  
9 For the case of finite sets (scattered data), in particular, our approximations provide a natural triangulation and piecewise affine  
10 interpolation. Prototype examples of explicitly calculated approximations and inpainting results are presented for both finite and  
11 compact sets. We also show numerical experiments for applications of our methods to high density salt & pepper noise reduction in  
12 image processing, for image inpainting and for approximation and interpolations of continuous functions sampled on finitely many level  
13 sets and on scattered points.

14     **Key words.** compensated convex transforms, scattered data, contour lines, interpolation, approximation, inpainting, Hausdorff  
15 stability, maximum principle, convex density radius, image inpainting, high density salt & pepper noise reduction

16     **AMS subject classifications.** 90C25, 90C26, 49J52, 52A41, 65K10

17     **1. Introduction.** This paper is concerned with the application of the compensated-convexity based theory  
18 for approximation and interpolation of sampled functions that was presented in our previous article [55] to sur-  
19 face reconstruction based on knowledge from finitely many level sets, scattered data approximation, and image  
20 inpainting.

21 In general, approximation theory is concerned with the problem of finding in the set of simple known functions one  
22 that is close in some sense to a more complicated otherwise unknown function. The variational theory is developed  
23 by specifying a priori the class of the approximating functions and the criteria that allow selecting an element  
24 of such class. In the implementation of the theory, the approximating functions generally depend on unknowns  
25 parameters that control their form, so that the problem boils down to selecting the parameters that allow meeting  
26 the chosen criteria. Such criteria are usually related to the error between the approximating functions and what  
27 is known about the function to be approximated and might contain some regularizing term that determines the  
28 regularity of the approximating function and makes the whole problem well posed.

29 Different classes of approximating functions, such as, for instance, algebraic polynomials [49], trigonometric poly-  
30 nomials [48, 49], radial basis functions [51, 11, 23], continuous piecewise polynomials [40], have been considered,  
31 and while their definition is usually motivated by good approximating properties for a given field of application,  
32 on the other hand the specific nature of a class of functions also represents a restriction that limits their general  
33 application.

34 Total variation-type models [42, 10], [17, Ch. 6] and geometric partial differential equations [13],[50, Ch. 1],[43, Ch.  
35 8] have also been used as interpolation models. Their use has been principally motivated by applications in the field  
36 of image processing and geoscience. We mention in particular the applications to salt & pepper noise reduction  
37 [14], image inpainting (by using TV-inpainting models [9, 29],[17, Ch. 6], Curvature Diffusion Driven inpainting  
38 model [16], geometric PDE based inpainting model [8] or other PDE-based models discussed in the monograph  
39 [45]) and image interpolation [6, 13, 28], among others. For the applications to geoscience, and in particular to  
40 the construction of digital elevation models, PDE based interpolation models, such as the one considered in [2],

---

\*Submitted to the editors DATE.

<sup>†</sup>School of Mathematical Sciences, University of Nottingham, University Park, Nottingham, NG7 2RD, UK  
(kewei.zhang@nottingham.ac.uk).

<sup>‡</sup>Department of Mathematics, Swansea University, Singleton Park, Swansea, SA2 8PP, UK (e.c.m.crooks@swansea.ac.uk).

<sup>§</sup>CONICET, Departamento de Bioingeniería, FACET, Universidad Nacional de Tucumán, Argentina (aorlando@herrera.unt.edu.ar).

41 where the interpolant is sought as the absolutely minimizing Lipschitz extension [5, 34] of the known values, have  
 42 also been proposed and shown to be competitive against the classical interpolation methods such as the geodesic  
 43 distance transformation method [46], the thin plate model [20, 26] and the kriging method [47].

44 As for these latter methods, although there is a well-developed mathematical theory on the existence and uniqueness  
 45 of weak solutions of variational models [4, 7, 30], and of the viscosity solution [5, 34] of the PDE based interpolation  
 46 model used in [13], the quantitative effectiveness of such methods is mostly assessed on the basis of numerical  
 47 experiments.

48 The new approximation and interpolation theory introduced in [55] is based, on the other hand, on the theory  
 49 of compensated convex transforms [52, 57, 56, 54] and can be applied to general bounded real-valued functions  
 50 sampled from either a compact set  $K \subset \mathbb{R}^n$  or the complement  $K = \mathbb{R}^n \setminus \Omega$  of a bounded open set  $\Omega$ . The  
 51 methods presented in [55] centre on the so-called average approximation that is recalled in Definition 1.1 below.  
 52 Importantly, [55] establishes error estimates for the approximation of bounded uniformly continuous functions, or  
 53 Lipschitz functions, and of  $C^{1,1}$ -functions, and proves rigorously that the approximation methods are stable with  
 54 respect to the Hausdorff distance between samples.

55 Here we apply the average approximation method developed in [55] to three important problems: level set and  
 56 scattered data approximation and interpolation, for which the sample set  $K \subset \mathbb{R}^n$  is compact, and the inpainting  
 57 problem in image processing, where the aim is to reconstruct an image in a damaged region based on the image  
 58 values in the undamaged part and the sample set  $K = \mathbb{R}^n \setminus \Omega$  is the complement of a bounded open set  $\Omega$   
 59 representing the damaged area of the image. We will also present a series of prototype examples of explicitly  
 60 calculated approximations that build insight into the behaviour of the average approximation introduced in [55],  
 61 as well as a selection of illustrative numerical experiments.

62 Before outlining the rest of the paper, we first recall the definitions of compensated convex transforms [52] and  
 63 average approximation [55]. Suppose  $f : \mathbb{R}^n \rightarrow \mathbb{R}$  is bounded. The quadratic lower and upper compensated convex  
 64 transform [52] (lower and upper transforms for short) are defined for each  $\lambda > 0$  by

$$65 \quad (1.1) \quad \begin{aligned} C_\lambda^l(f)(x) &= \text{co}[\lambda \cdot |x|^2 + f](x) - \lambda|x|^2, \\ \text{resp. } C_\lambda^u(f)(x) &= \lambda|x|^2 - \text{co}[\lambda \cdot |x|^2 - f](x), \quad x \in \mathbb{R}^n, \end{aligned}$$

66 where  $|x|$  is the standard Euclidean norm of  $x \in \mathbb{R}^n$  and  $\text{co}[g]$  denotes the convex envelope [33, 41] of a function  
 67  $g : \mathbb{R}^n \rightarrow \mathbb{R}$  that is bounded below.

68 Let  $K \subset \mathbb{R}^n$  be a non-empty closed set. Given a function  $f : \mathbb{R}^n \rightarrow \mathbb{R}$ , we denote by  $f_K : \mathbb{R}^n \supset K \rightarrow \mathbb{R}$  the  
 69 restriction of  $f$  to  $K$ , which can be thought of as a sampling of the original function  $f$ , which we would like to  
 70 approximate, on the convex hull of the set  $K$ .

71 Suppose that for some constant  $A_0 > 0$ ,  $|f_K(x)| \leq A_0$  for all  $x \in K$ . Then given  $M > 0$ , we define two bounded  
 72 functions that extend  $f_K$  to  $\mathbb{R}^n \setminus K$ , namely

$$73 \quad (1.2) \quad \begin{aligned} f_K^{-M}(x) &= f(x)\chi_K(x) - M\chi_{\mathbb{R}^n \setminus K} = \begin{cases} f_K(x), & x \in K, \\ -M, & x \in \mathbb{R}^n \setminus K; \end{cases} \\ f_K^M(x) &= f(x)\chi_K(x) + M\chi_{\mathbb{R}^n \setminus K} = \begin{cases} f_K(x), & x \in K, \\ M, & x \in \mathbb{R}^n \setminus K, \end{cases} \end{aligned}$$

74 where  $\chi_G$  denotes the characteristic function of a set  $G$ .

75 **DEFINITION 1.1.** *The **average compensated convex approximation** with scale  $\lambda > 0$  and module  $M > 0$*   
 76 *of the sampled function  $f_K : K \rightarrow \mathbb{R}$  is defined by*

$$77 \quad (1.3) \quad A_\lambda^M(f_K)(x) = \frac{1}{2} (C_\lambda^l(f_K^M)(x) + C_\lambda^u(f_K^{-M})(x)), \quad x \in \mathbb{R}^n.$$

78 In addition, we can also set  $M = +\infty$  in place of (1.2) and consider the following functions, commonly used in  
 79 convex analysis,

$$80 \quad (1.4) \quad f_K^{-\infty}(x) = \begin{cases} f(x), & x \in K, \\ -\infty, & x \in \mathbb{R}^n \setminus K; \end{cases} \quad f_K^{+\infty}(x) = \begin{cases} f(x), & x \in K, \\ +\infty, & x \in \mathbb{R}^n \setminus K. \end{cases}$$

81 and define the corresponding average approximation approximation,

$$82 \quad (1.5) \quad A_\lambda^\infty(f_K)(x) := \frac{1}{2} (C_\lambda^l(f_K^{+\infty})(x) + C_\lambda^u(f_K^{-\infty})(x)), \quad x \in \mathbb{R}^n.$$

83 By doing so, we can establish better approximation results than those obtained using  $f_K^{-M}$  and  $f_K^M$ , but  $A_\lambda^\infty(f_K)$   
 84 is not Hausdorff stable with respect to sample sets, in contrast to the basic average approximation  $A_\lambda^M(f_K)$  (see  
 85 [55, Thm. 4.12]).

86 The plan of the rest of the paper is as follows. Section 2 introduces notation and recalls key definitions and results  
 87 from our article [55], including error estimates for the average approximation  $A_\lambda^M(f_K)$  of bounded and uniformly  
 88 continuous, Lipschitz, and  $C^{1,1}$  functions. In Section 3, we consider level set interpolation and approximation, for  
 89 which  $f$  is continuous and  $K$  consists of finitely many compact level sets. We give conditions so that  $A_\lambda^M(f_K)$  is  
 90 an interpolation between level sets and also establish a maximum principle. Section 4 treats the case of scattered  
 91 data, when  $K$  is finite. In this case, we show that when  $\lambda > 0$  is sufficiently large and when  $M \gg \lambda$ ,  $A_\lambda^M(f_K)$  is a  
 92 piecewise affine interpolation of  $f_K$  in the convex hull of  $K$ . Moreover, if  $K$  is regular in the sense of the Delaunay  
 93 triangulation, we show that  $A_\lambda^M(f_K)$  agrees with the piecewise interpolation given by the Delaunay method. In  
 94 the irregular case that the Delaunay sphere  $S_r$  contains more than  $n + 1$  points in  $\mathbb{R}^n$ ,  $A_\lambda^M(f_K)$  is the average of  
 95 the maximum and minimum piecewise affine interpolation over the convex hull of  $K \cap S_r$ . Section 5 presents error  
 96 estimates for our average approximation in the context of the inpainting problem, and compares and contrasts these  
 97 estimates with the error analysis in [15]. We also give a simple one-dimensional example to illustrate the effect of  
 98 the upper and lower compensated convex transforms  $C_\lambda^u(f)$ ,  $C_\lambda^l(f)$  and the average approximation  $A_\lambda^M(f_K)$  on a  
 99 jump function, to provide insight into how jump discontinuities behave under our approach.

100 Section 6 contains explicitly calculated prototype examples in  $\mathbb{R}^2$ , including both examples where the sample set  
 101  $K$  is finite, and also examples where  $K$  is not finite. We present graphs of our calculated average approximation  
 102 for two irregular Delaunay cells, for 4 and for 8 points on the unit circle. We also present prototype examples of  
 103 contour line approximations, as well as prototypes for inpainting of functions that show that singularities such as  
 104 ridges and jumps can be preserved subject to compensated convex approximations to the original function when  
 105 the singular parts are close to each other. Section 7 discusses several numerical experiments for level set and point  
 106 clouds reconstructions of functions and images, for image inpainting, and for restoration of images with heavy salt  
 107 & pepper noise. Though such experiments are carried out only on a proof-of-concept level, we briefly report on the  
 108 comparison of our method with some state-of-art methods. In Section 8 we conclude the paper with proofs of our  
 109 main theorems stated in Sections 3, 4 and 5.

110 **2. Notation and Preliminaries.** Throughout the paper, we adopt the following notation and recall those  
 111 results from [55] that will be used here for our proofs, to make the development as self-contained as possible. For  
 112 the necessary background in convex analysis, we refer to the monographs [41, 33].

113 For a given set  $E \subset \mathbb{R}^n$ , with  $\mathbb{R}^n$  a  $n$ -dimensional Euclidean space,  $\bar{E}$ ,  $\partial E$ ,  $\overset{\circ}{E}$ ,  $E^c$  and  $\text{co}[E]$  stand for the closure,  
 114 the boundary, the interior, the complement and the convex hull of  $E$ , i.e. the smallest convex set which contains  $E$ ,  
 115 respectively. For a convex set  $E \subset \mathbb{R}^n$ , we define the dimension of  $E$ ,  $\dim(E)$ , as the dimension of the intersection  
 116 of all affine manifolds that contain  $E$ , where by affine manifold we mean a translated subspace, i.e. a set  $N$  of the  
 117 form  $N = x + S$  with  $x \in \mathbb{R}^n$  and  $S$  a subspace of  $\mathbb{R}^n$ . We then define  $\dim(N) = \dim(S)$ . We use the term of  
 118 convex body to denote a compact convex set with non-empty interior. The convex hull of a finite set of points is  
 119 called a polytope and with the notation  $\#(E)$  we denote the cardinality of the finite set  $E$ . If  $E = \{x_1, \dots, x_{k+1}\}$   
 120 and  $\dim(E) = k$ , then  $\text{co}[E]$  is called a  $k$ -dimensional simplex and the points  $x_1, \dots, x_{k+1}$  are called vertices. A

121 zero-dimensional simplex is a point; a one-dimensional simplex is a line segment; a two-dimensional simplex is a  
 122 triangle; a three-dimensional simplex is a tetrahedron. The condition that  $\dim(E) = k$  is equivalent to require that  
 123 the vectors  $x_2 - x_1, \dots, x_{k+1} - x_1$  are linearly independent.

124 The open ball centered at  $x \in \mathbb{R}^n$  and of radius  $r > 0$  is denoted by  $B(x; r) = \{y \in \mathbb{R}^n : |y - x| < r\}$  where  $|\cdot|$   
 125 stands for the Euclidean norm in  $\mathbb{R}^n$ , thus  $|x - y|$  is the distance between the points  $x, y \in \mathbb{R}^n$ . The diameter of  
 126 the set  $E \subset \mathbb{R}^n$ ,  $\text{diam}(E)$ , is then defined as  $\text{diam}(E) = \sup_{x, y \in E} |x - y|$ .

127 In this paper, we will assume, unless otherwise specified, that  $K \subset \mathbb{R}^n$  is either a compact set or the complement  
 128 of a bounded open set, that is,  $K = \Omega^c$  where  $\Omega \subset \mathbb{R}^n$  is a bounded open set. A function  $g : \text{co}[K] \subset \mathbb{R}^n \rightarrow \mathbb{R}$  is  
 129 said to be an *interpolation* of  $f_K$  if  $g = f$  in  $K$ , while for  $\lambda > 0$ , a family of functions  $g_\lambda : \text{co}[K] \subset \mathbb{R}^n \rightarrow \mathbb{R}$  is said  
 130 to *approximate*  $f$  if  $\lim_{\lambda \rightarrow +\infty} g_\lambda = f$  uniformly in  $K$ .

131 The error estimates obtained in [55] are expressed in terms of the modulus of continuity of the underlying function  
 132  $f$  to be approximated and of the convex density radius of  $K$ . For the convenience of the reader, these definitions are  
 133 recalled here. The modulus of continuity of a bounded and uniformly continuous functions  $f$  is defined as follows  
 134 [19, 32].

135 DEFINITION 2.1. *Let  $f : \mathbb{R}^n \rightarrow \mathbb{R}$  be a bounded and uniformly continuous function in  $\mathbb{R}^n$ . Then,*

$$136 \quad (2.1) \quad \omega_f : t \in [0, \infty) \rightarrow \omega_f(t) = \sup \left\{ |f(x) - f(y)| : x, y \in \mathbb{R}^n \text{ and } |x - y| \leq t \right\}$$

137 *is called the modulus of continuity of  $f$ .*

138 We also recall that the modulus of continuity of  $f$  has the following properties [32, page 19-21].

139 PROPOSITION 2.2. *Let  $f : \mathbb{R}^n \rightarrow \mathbb{R}$  be a bounded and uniformly continuous function in  $\mathbb{R}^n$ . Then the modulus  
 140 of continuity  $\omega_f$  of  $f$  satisfies the following properties:*

- $$141 \quad (2.2) \quad \begin{aligned} & (i) \quad \omega_f(t) \rightarrow \omega_f(0) = 0, \text{ as } t \rightarrow 0; \\ & (ii) \quad \omega_f \text{ is non-negative and non-decreasing continuous function on } [0, \infty); \\ & (iii) \quad \omega_f \text{ is subadditive: } \omega_f(t_1 + t_2) \leq \omega_f(t_1) + \omega_f(t_2) \text{ for all } t_1, t_2 \geq 0. \end{aligned}$$

142 Any function  $\omega$  defined on  $[0, \infty)$  and satisfying (2.2)(i), (ii), (iii) is called a *modulus of continuity*. A modulus of  
 143 continuity  $\omega$  can be bounded from above by an affine function (see [19, Lemma 6.1]), that is, there exist constants  
 144  $a > 0$  and  $b \geq 0$  such that

$$145 \quad (2.3) \quad \omega(t) \leq at + b \quad (\text{for all } t \geq 0).$$

146 As a result, given  $\omega_f$ , one can define the least concave majorant of  $\omega_f$ , which we denote by  $\omega$ , which is also a  
 147 modulus of continuity with the property (see [19])

$$148 \quad (2.4) \quad \frac{1}{2}\omega(t) \leq \omega_f(t) \leq \omega(t) \quad \text{for all } t \in [0, \infty).$$

149 The convex density radius of a point  $x \in \text{co}[K]$  with respect to the set  $K$  and the convex density radius of  $K$  in  
 150  $\text{co}[K]$  are the geometrical quantities that describe the set  $K$  with respect to its convex hull and are such properties  
 151 which enter the error estimates for our approximation operators. We recall next their definition from [55].

152 DEFINITION 2.3. *Suppose  $K \subset \mathbb{R}^n$  is a non-empty and closed set, and denote by  $\text{dist}(x; K)$  the Euclidean  
 153 distance of  $x$  to  $K$ . For  $x \in \text{co}[K]$ , consider the balls  $B(x; r)$  such that  $x \in \text{co}[\bar{B}(x; r) \cap K]$ . The convex density  
 154 radius of  $x$  with respect to  $K$  is defined as follows*

$$155 \quad (2.5) \quad r_c(x) = \inf \{r \geq 0 \text{ such that } x \in \text{co}[\bar{B}(x; r) \cap K]\},$$

156 *whereas the convex density radius of  $K$  in  $\text{co}[K]$  is defined by*

$$157 \quad (2.6) \quad r_c(K) = \sup \{r_c(x), x \in \text{co}[K]\}.$$

158 Here it is also useful to introduce the following, more geometric quantities. Let  $Q \subset \mathbb{R}^n$  be a bounded set, and  
 159 given  $x \in Q$  and  $\nu \in \mathbb{R}^n$  with  $|\nu| = 1$ , define the quantity

160 
$$d_\nu(x) = d_\nu^+(x) + d_\nu^-(x),$$

161 where

162 
$$d_\nu^+(x) = \sup \left\{ t > 0 : x + s\nu \in Q \text{ for } 0 \leq s \leq t \right\} \text{ and } d_\nu^-(x) = \sup \left\{ t > 0 : x - s\nu \in Q \text{ for } 0 \leq s \leq t \right\}.$$

163 It is then easy to see that  $d_\nu(x)$  is the length of the line segment with direction  $\nu$  passing through  $x$  and intersecting  
 164  $\partial Q$  at two points on each side. We also define

165 (2.7) 
$$d(x) = \inf \left\{ d_\nu(x), \nu \in \mathbb{R}^n, |\nu| = 1 \right\}$$

166 and the thickness of the set  $Q \subset \mathbb{R}^n$  as

167 (2.8) 
$$D_Q = \sup \left\{ d(x), x \in Q \right\}.$$

168 **REMARK 2.4.** (a) Given a non-empty bounded open set  $Q = \Omega \subset \mathbb{R}^n$ , by comparing definition (2.5) of  
 169  $r_c(x)$  and (2.8) of  $d(x)$ , it is straightforward to verify that

170 (2.9) 
$$r_c(x) \leq d(x)$$

171 for  $x \in \Omega$ .

172 (b) If the interior  $\mathring{Q} = \emptyset$ , such as in the case of a discrete set, then its thickness  $D_Q$  is zero.

173 We recall next the error estimates for our average approximation operators developed in [55] and refer to [55] for  
 174 proofs and details. For the case of  $K$  compact and  $M = +\infty$ , we have the following.

175 **THEOREM 2.5.** (See [55, Theorem 3.6]) Suppose  $f : \mathbb{R}^n \rightarrow \mathbb{R}$  is bounded and uniformly continuous, satisfying  
 176  $|f(x)| \leq A_0$  for some constant  $A_0 > 0$  and all  $x \in \mathbb{R}^n$ , and let  $K \subset \mathbb{R}^n$  be a non-empty compact set. Denote by  $\omega$   
 177 the least concave majorant of the modulus of continuity of  $f$ . Let  $a \geq 0, b \geq 0$  be such that  $\omega(t) \leq at + b$  for  $t \geq 0$ .  
 178 Then for all  $\lambda > 0$  and  $x \in \text{co}[K]$ ,

179 (2.10) 
$$|A_\lambda^\infty(f_K)(x) - f(x)| \leq \omega \left( r_c(x) + \frac{a}{\lambda} + \sqrt{\frac{2b}{\lambda}} \right).$$

180 where  $r_c(x) \geq 0$  is the convex density radius of  $x$  with respect to  $K$ . If we further assume that  $f$  is a globally  
 181 Lipschitz function with Lipschitz constant  $L > 0$ , then for all  $\lambda > 0$  and  $x \in \text{co}[K]$ ,

182 (2.11) 
$$|A_\lambda^\infty(f_K)(x) - f(x)| \leq Lr_c(x) + \frac{L^2}{\lambda}.$$

183 Section 4 will discuss an application of Theorem 2.5 to the case of scattered data approximation. We will apply  
 184 Theorem 2.5 also to the case of salt-and-pepper noise removal, where  $K$  is the compact set given by the part of  
 185 the image which is noise free. Section 7 contains a numerical experiment showing such an application.

186 A similar statement to Theorem 2.5 is obtained with  $M$  finite in the case that  $K = \Omega^c$ , where  $\Omega \subset \mathbb{R}^n$  is a  
 187 non-empty bounded open set. In this case, clearly  $\text{co}[K] = \mathbb{R}^n$  and the error estimate of the average approximation  
 188  $A_\lambda^M(f_K)$  is as follows.

189 **THEOREM 2.6.** (See [55, Theorem 3.7]) Suppose  $f : \mathbb{R}^n \rightarrow \mathbb{R}$  is bounded and uniformly continuous, satisfying  
 190  $|f(x)| \leq A_0$  for some constant  $A_0 > 0$  and all  $x \in \mathbb{R}^n$ . Let  $\Omega \subset \mathbb{R}^n$  be a bounded open set,  $d_\Omega$  the diameter of  $\Omega$

191 and  $K = \Omega^c$ . Denote by  $\omega$  the least concave majorant of the modulus of continuity of  $f$  and let  $a \geq 0$ ,  $b \geq 0$  be  
 192 such that  $\omega(t) \leq at + b$  for  $t \geq 0$ . Then for  $\lambda > 0$ ,  $M > A_0 + \lambda d_{\Omega}^2$ , and all  $x \in \mathbb{R}^n$ ,

$$193 \quad (2.12) \quad |A_{\lambda}^M(f_K)(x) - f(x)| \leq \omega \left( r_c(x) + \frac{a}{\lambda} + \sqrt{\frac{2b}{\lambda}} \right),$$

194 where  $r_c(x) \geq 0$  is the convex density radius of  $x$  with respect to  $K$ . If we further assume that  $f$  is a globally  
 195 Lipschitz function with Lipschitz constant  $L > 0$ , then for  $\lambda > 0$ ,  $M > A_0 + \lambda d_{\Omega}^2$  and all  $x \in \mathbb{R}^n$ , we have

$$196 \quad (2.13) \quad |A_{\lambda}^M(f_K)(x) - f(x)| \leq Lr_c(x) + \frac{L^2}{\lambda}.$$

197 Under an additional restriction on  $f$  and on  $K$ , it is possible to extend the results of Theorem 2.6 to the case when  
 198  $K$  is a compact set and thus to obtain error estimates independent of  $M$ . More precisely, the following result refers  
 199 to the case where we are given the values of the function  $f$  on the union of a compact set and the complement of a  
 200 bounded open set. This extension allows the application of Theorem 2.6 to the problem of inpainting, for instance.

201 **COROLLARY 2.7.** (See [55, Corollary 3.9]) Suppose  $f : \mathbb{R}^n \rightarrow \mathbb{R}$  is bounded and uniformly continuous satisfying  
 202  $|f(x)| \leq A_0$  for some constant  $A_0 > 0$  and all  $x \in \mathbb{R}^n$ . Assume that  $f(x) = c_0$  for  $|x| \geq r > 0$ , where  $c_0 \in \mathbb{R}$   
 203 and  $r > 0$  are constants. Let  $K \subset \mathbb{R}^n$  be a non-empty compact set satisfying  $K \subset \bar{B}(0; r)$ . For  $R > r$ , define  
 204  $K_R := K \cup B^c(0; R)$ . Denote by  $\omega$  the least concave majorant of the modulus of continuity of  $f$ . Let  $a \geq 0$ ,  $b \geq 0$   
 205 be such that  $\omega(t) \leq at + b$  for  $t \geq 0$ . Then for all  $\lambda > 0$ ,  $M > A_0 + \lambda(R+r)^2$  and all  $x \in \text{co}[K]$ ,

$$206 \quad (2.14) \quad |A_{\lambda}^M(f_{K_R})(x) - f(x)| \leq \omega \left( r_c(x) + \frac{a}{\lambda} + \sqrt{\frac{2b}{\lambda}} \right),$$

207 where  $r_c(x) \geq 0$  is the convex density radius of  $x$  with respect to  $K$ . If we further assume that  $f$  is a globally  
 208 Lipschitz function with Lipschitz constant  $L > 0$ , then for  $\lambda > 0$ ,  $M > A_0 + \lambda(R+r)^2$  and all  $x \in \text{co}[K]$ , we have

$$209 \quad (2.15) \quad |A_{\lambda}^M(f_{K_R})(x) - f(x)| \leq Lr_c(x) + \frac{L^2}{\lambda}.$$

210 If we further assume that  $f$  is a  $C^{1,1}$  function such that  $|Df(x) - Df(y)| \leq L|x - y|$  for all  $x, y \in \mathbb{R}^n$  and  $L > 0$   
 211 is a constant, then for  $\lambda > L$ ,  $M > A_0 + \lambda(R+r)^2$  and all  $x \in \text{co}[K]$ , we have

$$212 \quad (2.16) \quad |A_{\lambda}^M(f_{K_R})(x) - f(x)| \leq \frac{L}{4} \left( \frac{\lambda + L/2}{\lambda - L/2} + 1 \right) r_c^2(x).$$

213 Furthermore, in case (iii),  $A_{\lambda}^M(f_{K_R})$  is an interpolation of  $f_K$  in  $\mathbb{R}^n$ .

214 The conditions of Corollary 2.7 can be realized, for instance, in the case we can define  $f$  to be zero outside a large  
 215 ball containing  $K$ .

216 Theorem 2.6 and Corollary 2.7 will be applied to the case of (i) surface reconstructions from a finitely many level  
 217 sets representation and (ii) inpainting of damaged images, where  $\Omega$  is the domain to be inpainted and  $K = \Omega^c$ . We  
 218 will discuss such applications in Section 3 and Section 5, respectively, whereas Section 7 contains some numerical  
 219 experiments of both applications.

220 We conclude this section by giving the following property which will be useful in Section 4 that deals with  
 221 scattered data approximations.

222 **PROPOSITION 2.8.** (The restriction property) Let  $m \geq 1$ ,  $n \geq 1$ . Suppose  $f : \mathbb{R}^n \rightarrow \mathbb{R}$  is bounded, satisfying

223  $|f(x)| \leq M$  for some  $M > 0$  and for all  $x \in \mathbb{R}^n$ . Let  $g^{\pm M} : \mathbb{R}^n \times \mathbb{R}^m \rightarrow \mathbb{R}$  be defined, respectively, as follows

$$g^M(x, y) = \begin{cases} f(x), & x \in \mathbb{R}^n, y = 0 \in \mathbb{R}^m, \\ M, & x \in \mathbb{R}^n, y \in \mathbb{R}^m, y \neq 0; \end{cases}$$

$$g^{-M}(x, y) = \begin{cases} f(x), & x \in \mathbb{R}^n, y = 0 \in \mathbb{R}^m, \\ -M, & x \in \mathbb{R}^n, y \in \mathbb{R}^m, y \neq 0. \end{cases}$$

225 Then

$$C_\lambda^l(g^M)(x, 0) = C_\lambda^l(f)(x) \quad \text{and} \quad C_\lambda^u(g^{-M})(x, 0) = C_\lambda^u(f)(x) \quad (\text{for } x \in \mathbb{R}^n).$$

227 In the case the sampled set  $K$  is compact, the restriction property and Corollary 2.7 imply that if  $K$  is  
 228 contained in a  $k$ -dimensional plane  $E \subset \mathbb{R}^n$ , we can then calculate the average approximation operator  $A_\lambda^M(f_K(x))$   
 229 for  $x \in \text{co}[K] \subset E$  by restricting our calculations in  $E$ .

230 **3. Level Set Approximations.** We consider the case where the sampled set is given by the union of finitely  
 231 many compact level sets, that is, we know the values of a continuous function  $f$  only on finitely many compact  
 232 contour lines, and we want to study the structure of  $A_\lambda^M(f_K)$ . We will establish a result which gives a natural  
 233 bound on the value of  $A_\lambda^M(f_K)$ , ensuring that, for  $\lambda > 0$  sufficiently large, the value of  $A_\lambda^M(f_K)$  at points between  
 234 level sets is between the values of the corresponding level sets, and present an error estimate for  $A_\lambda^M(f_K)$ .

235 Let  $f : \mathbb{R}^n \rightarrow \mathbb{R}$  be a continuous function and  $a \in \mathbb{R}$ . Denote by  $\Gamma_a = \{x \in \mathbb{R}^n, f(x) = a\}$  the level set of  $f$  of level  
 236  $a$  and by  $V_a := \{x \in \mathbb{R}^n, f(x) \leq a\}$  the sublevel set of  $f$  of level  $a$ .

237 We then have the following result.

238 **THEOREM 3.1.** Suppose  $f : \mathbb{R}^n \rightarrow \mathbb{R}$  is continuous and that for  $a_0 < a_1 < \dots < a_m$ ,  $m \in \mathbb{N}$ , the level sets  
 239  $\Gamma_{a_i} = \{x \in \mathbb{R}^n, f(x) = a_i\}$  are compact for  $i = 0, 1, \dots, m$ . Denote by

$$\delta_0 = \min \left\{ \text{dist}(\Gamma_{a_i}, \Gamma_{a_j}), 0 \leq i, j \leq m, i \neq j \right\} > 0,$$

241 the minimum Euclidean distance between two different level sets. Define  $K = \cup_{i=0}^m \Gamma_{a_i}$  and denote by  $d_K$  the  
 242 diameter of  $K$ . If  $\lambda > (a_m - a_0)/\delta_0^2$  and  $M > \lambda d_K^2 + \max_K |f|$ , then

243 (i)  $A_\lambda^M(f_K)$  is an interpolation of  $f$  from  $K$  to  $\text{co}[K]$ , that is, for  $x_0 \in \Gamma_{a_i}$ ,  $i = 0, 1, \dots, m$ ,

$$(3.1) \quad A_\lambda^M(f_K)(x_0) = a_i.$$

244 (ii) For each  $x_0$  satisfying  $a_i \leq f(x_0) \leq a_{i+1}$  for some  $0 \leq i \leq m - 1$ ,

$$(3.2) \quad a_i \leq A_\lambda^M(f_K)(x_0) \leq a_{i+1}.$$

245 (iii)  $A_\lambda^M(f_K)(x_0) = a_0$  for  $x_0 \in V_{a_0}$ .

248 **REMARK 3.2.** (a) A sufficient condition for the level set  $\Gamma_a$  to be compact is that  $f$  is continuous and either  
 249  $\lim_{|x| \rightarrow \infty} f(x) = +\infty$  or  $\lim_{|x| \rightarrow \infty} f(x) = -\infty$ .

250 (b) It might happen that there is an open subset of  $\{x \in \mathbb{R}^n, a_i \leq f(x) \leq a_{i+1}\}$  on which  $A_\lambda^M(f_K)(x) = a_i$  or  
 251  $A_\lambda^M(f_K)(x) = a_{i+1}$ . Therefore Theorem 3.1 gives a weak maximum principle.

252 (c) In  $\mathbb{R}^2$ , it is not difficult to see that if two neighbouring level sets are parallel lines, then our interpolation  
 253 gives a plane passing through these two lines. However, if the function under consideration is not contin-  
 254 uous, different level-sets can ‘intersect’ each other. In general, it is not clear what the natural level-set  
 255 approximations for functions with jump discontinuity will be like. In Section 6 we will present a prototype  
 256 example of two level lines which are not parallel to each other and work out an analytical expression of the  
 257 interpolation operator  $A_\lambda^M(f_K)$  for such a case.

258 We next give an error estimate for our level set average approximation  $A_\lambda^M(f_K)$ , which is obtained by applying  
 259 Corollary 2.7 [55, Corollary 3.9]. We first introduce some further definitions that are needed for the application of  
 260 this result. Under the assumptions of Theorem 3.1, for  $i = 0, 1, \dots, m-1$ , define the open set

$$261 \quad (3.3) \quad \Omega_i = \{x \in \mathbb{R}^n, a_i < f(x) < a_{i+1}\},$$

262 and then for  $x \in \Omega_i$ , define  $d_i(x)$  using (2.8) with  $Q = \Omega_i$ . Suppose that  $V_{a_m}$  is compact, let  $R > 0$  be such that  
 263  $V_{a_m} \subset B(0; R)$ , and set  $V_R^m = V_{a_m} \cup B^c(0; R)$ . Then define the auxiliary function

$$264 \quad \tilde{f}_{V_R^m}(x) = \begin{cases} f(x), & x \in V_{a_m}, \\ a_m + 1, & x \in B^c(0; R). \end{cases}$$

265 We consider the following two cases.

- 266 (i) If  $f$  is continuous,  $\tilde{f}_{V_R^m}$  is bounded and uniformly continuous in  $V_R^m$ . Therefore, by the Tietze extension  
 267 theorem [21, pag. 149],  $\tilde{f}_{V_R^m}$  can be extended to  $\mathbb{R}^n$  as a bounded uniformly continuous function. We  
 268 denote this extension by  $\tilde{f}$  and by  $\tilde{A}_0 > 0$  an upper bound of  $|\tilde{f}|$ . Clearly,  $\tilde{f}(x) = f(x)$  for  $x \in V_{a_m}$ .  
 269 Furthermore, we denote by  $\tilde{\omega}(t)$  the least concave majorant of the modulus of continuity of  $\tilde{f}$ , which is  
 270 itself a modulus of continuity, thus satisfies the properties (2.2), and in particular, can be bounded from  
 271 above by an affine function, that is, there exist some constants  $\tilde{a} \geq 0$  and  $\tilde{b} \geq 0$  such that  $\tilde{\omega}(t) \leq \tilde{a}t + \tilde{b}$  for  
 272 all  $t \geq 0$ .
- 273 (ii) If  $f$  is Lipschitz continuous with Lipschitz modulus  $L > 0$ , then  $\tilde{f}_{V_R^m}$  is bounded and Lipschitz continuous  
 274 in  $V_R^m$  with a possibly different Lipschitz modulus  $\tilde{L}$  such that

$$275 \quad (3.4) \quad \tilde{L} \leq \max \left\{ L, \max_{V_{a_m}} |f| + |a_m + 1| \right\}.$$

276 By Kirszbraun's theorem [24, pag. 202],  $\tilde{f}_{V_R^m}$  can then be extended to  $\mathbb{R}^n$  as a bounded Lipschitz function.  
 277 Again we denote this extension by  $\tilde{f}$  and assume that  $|\tilde{f}(x)| \leq \tilde{A}_0$  for all  $x \in \mathbb{R}^n$ .

278 With the notation above, we have the following error estimates for  $A_\lambda^M(f_K)$ .

279 **PROPOSITION 3.3.** *Suppose  $f : \mathbb{R}^n \rightarrow \mathbb{R}$  is continuous and that for  $a_0 < a_1 < \dots < a_m$ , the sublevel sets  
 280  $V_{a_0} \subset V_{a_1} \subset \dots \subset V_{a_m}$  are non-empty and compact. Let  $\Gamma_{a_i}$  be the level set of  $f$  of level  $a_i$ ,  $K = \cup_{i=0}^m \Gamma_{a_i}$ , and  
 281  $d_i(x)$ ,  $\Omega_i$  be defined by (2.8), (3.3), respectively, for  $i = 0, 1, \dots, m-1$ . Denote by  $\tilde{f}$  the function defined in (i)  
 282 above, and by  $\tilde{A}_0$  an upper bound of  $|\tilde{f}|$ . If  $\lambda > a_m - a_0 + 1$  and  $M > \tilde{A}_0 + \lambda(2R + 1)^2$ , then for all  $x \in \Omega_i$ ,  
 283  $i = 0, \dots, m-1$ , we have*

$$284 \quad (3.5) \quad |A_\lambda^M(f_K)(x) - f(x)| \leq \tilde{\omega} \left( d_i(x) + \frac{\tilde{a}}{\lambda} + \sqrt{\frac{2\tilde{b}}{\lambda}} \right),$$

285 where  $\tilde{\omega}$  is the least concave majorant of the modulus of continuity of  $\tilde{f}$ . If we further assume that  $f$  is a globally  
 286 Lipschitz function of Lipschitz constant  $L > 0$ ,  $\lambda > a_m - a_0 + 1$  and  $M > \tilde{A}_0 + \lambda(2R + 1)^2$ , then for all  $x \in \Omega_i$ ,  
 287  $i = 0, \dots, m-1$ , we have

$$288 \quad (3.6) \quad |A_\lambda^M(f_K)(x) - f(x)| \leq \tilde{L}d_i(x) + \frac{\tilde{L}^2}{\lambda},$$

289 where  $\tilde{L}$  is defined by (3.4).

290 **4. Scattered Data Approximations.** We now turn our attention to the so-called case of ‘scattered data’  
 291 approximation [51] corresponding to a discrete sampled set  $K$ . Since for any function  $f : \mathbb{R}^n \rightarrow \mathbb{R}$ , the restriction  
 292  $f_K$  of  $f$  to a finite set  $K$  is always a Lipschitz function, the following result provides a sufficient condition for our  
 293 upper and lower transforms to be interpolations in this case.

294 THEOREM 4.1. Suppose  $K = \{x_1, x_2, \dots, x_m\} \subset \mathbb{R}^n$  is a finite set with distinct points and assume  $f : K \subset$   
 295  $\mathbb{R}^n \rightarrow \mathbb{R}$  is a function. Assume  $-M < f(x_j) < M$  for  $j = 1, \dots, m$  and let  $L > 0$  be the Lipschitz constant of  
 296  $f : K \subset \mathbb{R}^n \rightarrow \mathbb{R}$ . Define  $\alpha = \min\{|x_i - x_j|, x_i, x_j \in K, i \neq j\} > 0$ . Then for  $\lambda \geq L/\alpha$ ,

$$297 \quad C_\lambda^u(f_K^{-M})(x_j) = f(x_j) \quad \text{and} \quad C_\lambda^l(f_K^M)(x_j) = f(x_j) \quad \text{for } x_j \in K.$$

298 Let  $K \subset \mathbb{R}^n$  be a finite set. Without loss of generality, from now on, we assume that  $\dim(\text{co}[K]) = n$ , that is, that  
 299  $\text{co}[K] \subset \mathbb{R}^n$  is a convex body. In the case  $\dim(\text{co}[K]) = k < n$ , we can simply translate  $K$  so that  $0 \in K$ , and  
 300 let  $E_k = \text{span}(\text{co}[K])$  where  $\text{span}(\text{co}[K])$  is the  $k$ -dimensional subspace spanned by  $\text{co}[K]$ . In this case,  $E_k \subset \mathbb{R}^n$   
 301 is a supporting plane of  $\text{co}[K]$  and we only need to work in  $E_k$  given that in our interpolation problem we are  
 302 only interested in values of our approximation in  $\text{co}[K]$ . We can therefore reduce our approximation/interpolation  
 303 problem to  $E_k$  by applying Proposition 2.8.

304 In order to describe our approximation/interpolation results, we first need to introduce notions related to the  
 305 Voronoi diagram and Delaunay triangulation for a finite set  $K$  [18, 38, 22].

306 Let  $K = \{x_1, \dots, x_m\}$  be a finite set of distinct points of  $\mathbb{R}^n$ , and denote  $m = \#(K)$ . We define  $\mathcal{V}(K)$ , the Voronoi  
 307 diagram of  $K$ , to be the partition of  $\mathbb{R}^n$  into  $m$  cells, one for each point of  $K$ , with the property that a point  $x \in \mathbb{R}^n$   
 308 belongs to the cell corresponding to the point  $x_i \in K$  if  $|x - x_i| < |x - x_j|$  for each  $x_j \in K$  with  $j \neq i$ . We then  
 309 denote by  $M(K)$  the Voronoi edges of the Voronoi diagram  $\mathcal{V}(K)$  of  $K$ , meaning the set of the edges of  $\mathcal{V}(K)$  where  
 310 a point  $y \in M(K)$  if there are at least two different points  $x_i, x_j \in K$  such that  $\text{dist}(y, K) = |y - x_i| = |y - x_j| > 0$ .  
 311 Then there are finitely many points  $y_1, \dots, y_l \in M(K)$ , called Voronoi vertices and whose set is denoted by  $V(K)$ ,  
 312 with the property that there are corresponding radii  $r_1, \dots, r_l > 0$ , such that for each  $y_i \in V(K)$ , there are  
 313  $m_i \geq n + 1$  points  $x_1^i, \dots, x_{m_i}^i \in K$  such that  $\text{dist}(y_i, K) = |y_i - x_j^i| = r_i$  so that the open ball  $B(y_i; r_i)$  does not  
 314 intersect  $K$  and  $\bar{B}(y_i; r_i) \cap K = \{x_1^i, \dots, x_{m_i}^i\}$ . If we write  $K_i = \{x_1^i, \dots, x_{m_i}^i\}$  for each  $i \in \{1, \dots, l\}$ , we also have  
 315 that  $\dim(\text{co}[K_i]) = n$ ,  $\cup_{j=1}^l \text{co}[K_j] = \text{co}[K]$ , and if  $i \neq j$ , either  $\dim(\text{co}[K_i] \cap \text{co}[K_j]) < n$  or  $\text{co}[K_i] \cap \text{co}[K_j] = \emptyset$   
 316 [38].

317 For each  $i = 1, \dots, l$ ,  $\text{co}[K_i]$  is referred to as a Delaunay cell with generator  $K_i$ , centre  $y_i$  and radius  $r_i$  and the ball  
 318  $B(y_i; r_i)$  is called the associated open ball of the Delaunay cell  $\text{co}[K_i]$ . We have  $K_i = K \cap \partial B(y_i; r_i)$  while  $K \cap$   
 319  $B(y_i; r_i) = \emptyset$ . A Delaunay cell is then said regular if it is an  $n$ -dimensional simplex (so in particular, a triangle if  $n =$   
 320 2 and a tetrahedron if  $n = 3$ ). If each Delaunay cell  $\text{co}[K_i]$  in  $\text{co}[K]$  is regular, the set  $\{\text{co}[K_1], \text{co}[K_2], \dots, \text{co}[K_l]\}$   
 321 is said to be the regular Delaunay triangulation of  $\text{co}[K]$ .

322 In the following, we consider two different situations.

- 323 (i) Each Delaunay cell  $\text{co}[K_i]$  is an  $n$ -dimensional simplex, that is,  $\text{co}[K]$  has a regular Delaunay triangulation;
- 324 (ii) For some or for all  $K_i$ 's,  $\dim(\text{co}[K_i]) = \dim(\text{co}[K]) = n$  and  $\#(K_i) > n + 1$ , that is, the Delaunay cell is a  
 325 convex polytope that is not an  $n$ -dimensional simplex.

326 We will show that if (i) holds, that is, if we have a regular Delaunay triangulation of  $\text{co}[K]$ , then our average  
 327 approximation  $A_\lambda^M(f_K)$  defines the usual piecewise affine interpolation based on this Delaunay triangulation [38,  
 328 page. 191] when  $\lambda > 0$  and  $M \gg \lambda$  are sufficiently large. If (ii) occurs, our average approximation  $A_\lambda^M(f_K)$  will  
 329 be the average of the minimum and maximum piecewise affine interpolations of  $f_K$  in the cell.

330 REMARK 4.2. A remarkable difference between our average approximation  $A_\lambda^M(f_K)$  and the usual design of  
 331 piecewise affine constructions is that we do not need to know or compute the Delaunay cells in advance. Our  
 332 method simply directly generates the piecewise affine function.

333 Before we state our first structural theorem on the effect of the upper, lower and average approximations over a  
 334 regular cell, we need the following lemma.

335 LEMMA 4.3. Let  $B(x^*; r) \subset \mathbb{R}^n$  be the open ball centred at  $x^*$  with radius  $r > 0$  and  $S = \{x_1, x_2, \dots, x_m\} \subset$   
 336  $\partial B(x^*; r)$  be a finite set with distinct points and with  $\#(S) = m \geq n + 1$ . Assume  $\text{co}[S] \subset B(x^*; r)$  to be the  
 337 convex hull of  $S$  satisfying  $\dim(\text{co}[S]) = n$ . Suppose  $f_S : S \rightarrow \mathbb{R}$  is a real-valued function with Lipschitz constant  
 338  $L > 0$ . If there is an affine function  $\ell_s : \mathbb{R}^n \rightarrow \mathbb{R}$  such that  $\ell_s(x_i) = f_S(x_i)$  for all  $x_i \in S$ , then there is a constant  
 339  $C_s > 0$  such that the gradient of  $\ell$  satisfies  $|D\ell_s(x)| \leq C_s L$ .

340 REMARK 4.4. In Lemma 4.3, if  $m = n + 1$ , then  $\text{co}[S]$  is a  $n$ -dimensional simplex and there is an affine function  
 341  $\ell_s$  such that  $\ell_s(x) = f_S(x)$  for  $x \in S$ . However if  $m > n + 1$ , in general one can not find an affine function satisfying  
 342  $\ell_s(x) = f_S(x)$  for  $x \in S$ . We will deal with such a case together with a more general one in Lemma 4.9 and in  
 343 Theorem 4.11.

344 We now calculate the transforms  $C_\lambda^u(f_K^{-M})$ ,  $C_\lambda^l(f_K^M)$  and  $A_\lambda^M(f_K)$  in a regular Delaunay cell  $\text{co}[S]$  satisfying  
 345  $m = \#(S) = n + 1$  and  $\dim(\text{co}[S]) = n$ . For each regular cell  $\text{co}[S]$ , define

$$346 \quad \sigma_s = \min \left\{ |x_j - x_s| - r_s, x_j \in K \setminus S \right\} > 0$$

347 where  $x_s, r_s$  are the centre and radius respectively of the associated Delaunay ball  $B(x_s; r_s)$  of  $\text{co}[S]$ , and let  $C_s$  be  
 348 the constant given by Lemma 4.3 for the affine function  $\ell_s$  associated with  $\{(x, f_S(x)), x \in S\}$ . We then have the  
 349 following result.

350 THEOREM 4.5. Let  $K = \{x_i\}_{i=1}^m \subset \mathbb{R}^n$  be a finite set with distinct points and let  $f_K : K \rightarrow \mathbb{R}$  be a function with  
 351 Lipschitz constant  $L > 0$  and bound  $A_0 > 0$ , that is,  $|f_K(x)| \leq A_0$  for  $x \in K$ . Suppose  $S = \{x_1, x_2, \dots, x_{l+1}\} \subset K$   
 352 satisfies that  $\text{co}[S]$  is a regular Delaunay cell with associated Delaunay ball  $B(x_s; r_s)$ . Let  $\ell_s : \mathbb{R}^n \rightarrow \mathbb{R}$  be the affine  
 353 function given by Lemma 4.3 for  $S$  and  $f_K$  restricted on  $S$ . Then, for every  $x \in \text{co}[S]$ ,

$$354 \quad (4.1) \quad \begin{aligned} C_\lambda^u(f_K^{-M})(x) &= \lambda|x - x_s|^2 - \lambda r_s^2 + \ell_s(x), & C_\lambda^l(f_K^M)(x) &= \lambda r_s^2 - \lambda|x - x_s|^2 + \ell_s(x), \\ A_\lambda^M(f_K)(x) &= \frac{C_\lambda^u(f_K^{-M})(x) + C_\lambda^l(f_K^M)(x)}{2} = \ell_s(x), \end{aligned}$$

355 whenever

$$356 \quad (4.2) \quad \lambda > \frac{2A_0}{\sigma_s(2r_s + \sigma_s)} + \frac{C_s L}{\sigma_s}$$

357 and

$$358 \quad (4.3) \quad M > \lambda r_s^2 + C_s L r_s + A_0 + \frac{C_s^2 L^2}{4\lambda}.$$

359 REMARK 4.6. If we replace our functions  $f_K^{-M}$  and  $f_K^M$  by  $f_K^{-\infty}$  and  $f_K^\infty$ , respectively, defined by

$$360 \quad f_K^{-\infty}(x) = \begin{cases} f_K(x), & \text{if } x \in K, \\ -\infty, & \text{if } x \in \mathbb{R}^n \setminus K \end{cases} \quad \text{and} \quad f_K^\infty(x) = \begin{cases} f_K(x), & \text{if } x \in K, \\ +\infty, & \text{if } x \in \mathbb{R}^n \setminus K, \end{cases}$$

361 then Condition (4.2) alone is sufficient to obtain (4.1). Although by setting  $M = +\infty$  we have a mathematically  
 362 simpler statement, the resulting approximations would not, however, meet the Hausdorff stability property (see [55,  
 363 Thm. 4.12] for a Hausdorff stability theorem for  $A_\lambda^M(f_K)$ ).

364 If we further assume that for the given finite set  $K$  there is a regular Delaunay triangulation of  $\text{co}[K]$ , which thus  
 365 consists of  $n$ -dimensional simplices, we can then easily give global explicit descriptions of  $C_\lambda^u(f_K^{-M})$  and  $C_\lambda^l(f_K^M)$ ,  
 366 and hence of  $A_\lambda^M(f_K)$  in each  $n$ -dimensional Delaunay simplex. This, however, requires  $\lambda > 0$  and  $M > 0$  to be  
 367 sufficiently large.

368 COROLLARY 4.7. Let  $K \subset \mathbb{R}^n$  be a finite set with distinct points such that it admits a regular Delaunay  
 369 triangulation  $\mathcal{D}(K)$  of  $\text{co}[K]$  thus comprising of the  $n$ -dimensional simplices  $\text{co}[S_1], \dots, \text{co}[S_l]$  where  $V(K)$  the set  
 370 of vertices of the Voronoi diagram  $\mathcal{V}(K)$  of  $K$  with  $\#(V(K)) = l$ . For each Delaunay cell  $S_i$  for  $i = 1, \dots, l$ ,  
 371 consider its associated open ball  $B(y_i; r_i)$  such that  $B(y_i; r_i) \cap K = \emptyset$  and  $K \cap \bar{B}(y_i; r_i) = S_i$  for  $i = 1, \dots, l$ .  
 372 Define  $\sigma_i = \min\{|x - y_i| - r_i, x \in K \setminus S_i\}$ .

373 Let  $f_K : K \subset \mathbb{R}^n \rightarrow \mathbb{R}$  be a function with Lipschitz constant  $L > 0$  satisfying, for some  $A_0 > 0$ ,  $|f_K(x)| \leq A_0$   
 374 for all  $x \in K$ . Let  $\ell_i$  be the affine function defined in Lemma 4.3 for  $S_i$ , such that  $\ell_i(x) = f_K(x)$  for  $x \in S_i$  and  
 375  $|D\ell_i(x)| \leq C_i L$  for some constant  $C_i > 0$ ,  $i = 1, \dots, l$ . Then in each simplex  $\text{co}[S_i]$ ,  $i = 1, \dots, l$ , and for every  
 376  $x \in \text{co}[S_i]$ , we have

$$377 \quad (4.4) \quad \begin{aligned} C_\lambda^u(f_K^{-M})(x) &= \lambda|x - x_i|^2 - \lambda r_i^2 + \ell_i(x), & C_\lambda^l(f_K^M)(x) &= \lambda r_i^2 - \lambda|x - x_i|^2 + \ell_i(x), \\ A_\lambda^M(f_K)(x) &= \frac{C_\lambda^u(f_K^{-M})(x) + C_\lambda^l(f_K^M)(x)}{2} = \ell_i(x), \end{aligned}$$

378 whenever

$$379 \quad (4.5) \quad \lambda > \max_{1 \leq i \leq m} \left( \frac{2A_0}{\sigma_i(2r_i + \sigma_i)} + \frac{C_i L}{\sigma_i} \right)$$

380 and

$$381 \quad M > \max_{1 \leq i \leq m} \left( \lambda r_i^2 + C_i L r_i + A_0 + \frac{C_i^2 L^2}{4\lambda} \right).$$

382 **REMARK 4.8.** A similar observation to Remark 4.6 for Theorem 4.5 can be made for Corollary 4.7. Under the  
 383 assumptions of Corollary 4.7, condition (4.5) is sufficient to ensure that (4.4) holds with  $f_K^{-\infty}$ ,  $f_K^{\infty}$  and  $A_\lambda^\infty(f_K)$ ,  
 384 respectively, for  $i = 1, \dots, l$  and for every  $x \in \text{co}[S_i]$ .

385 Let  $S = \{x_1, \dots, x_m\} \subset \mathbb{R}^n$ . Next we study the structure of our upper, lower transforms and average approxima-  
 386 tions when the  $n$ -dimensional Delaunay cell  $\text{co}[S]$  is not a simplex, that is,  $\#(S) = m > n + 1$ . In this case, we say  
 387 that the  $n$ -dimensional Delaunay cell  $\text{co}[S]$  is not regular. Without loss of generality we may assume that there is  
 388 an open ball  $B(0; r)$  centred at 0 with radius  $r > 0$ , such that  $S \subset \partial B(0; r)$ . Let  $f_S : S \rightarrow \mathbb{R}$  be a given function,  
 389 and write  $f_S(x_i) = v_i$ ,  $i = 1, \dots, m$ . Let  $\Gamma_s = \{(x_i, v_i), i = 1, \dots, m\}$  be the graph of  $f_S$  in  $S \times \mathbb{R}$ , we may assume  
 390 that the convex envelope  $\text{co}[\Gamma_s] \subset \mathbb{R}^n \times \mathbb{R}$  of  $\Gamma_s$  is an  $n + 1$ -dimensional convex polytope, otherwise there will be a  
 391 single affine function as in Lemma 4.3 satisfying  $\ell_s(x_i) = v_i$  and we are back to the situation of Theorem 4.5.

392 Let  $D = \text{co}[S] \subset \mathbb{R}^n$  and  $\Gamma = \partial \text{co}[\Gamma_s]$  be the boundary of the convex polytope  $\text{co}[\Gamma_s]$ . We have the following result.

393 **LEMMA 4.9.** Let  $S$ ,  $f_S$  and  $\Gamma_s$  be as defined above. Then

394 (i) There are two continuous piecewise affine functions  $p_+(x)$  and  $p_-(x)$  in  $D = \text{co}[S]$  defined by

$$\begin{aligned} p_+(x) &= \max\{v, (x, v) \in \text{co}[\Gamma_s]\} \\ &= \max \left\{ \sum_{i=1}^m \lambda_i v_i, x_i \in S, \lambda_i \geq 0, i = 1, \dots, m, \sum_{i=1}^m \lambda_i = 1, \sum_{i=1}^m \lambda_i x_i = x \right\}, \\ 395 \quad p_-(x) &= \min\{v, (x, v) \in \text{co}[\Gamma_s]\} \\ &= \min \left\{ \sum_{i=1}^m \lambda_i v_i, x_i \in S, \lambda_i \geq 0, i = 1, \dots, m, \sum_{i=1}^m \lambda_i = 1, \sum_{i=1}^m \lambda_i x_i = x \right\}, \end{aligned}$$

396 where  $p_+$  and  $p_-$  are piecewise affine concave and convex functions in  $D$  respectively;

397 (ii) For every  $x \in \overset{\circ}{D}$ , the interior of  $D$ ,  $p_-(x) < p_+(x)$ .

398 (iii) The convex polytope  $D \subset \mathbb{R}^n$  has two decompositions  $D = \cup_{i=1}^k D_i^+$  and  $D = \cup_{j=1}^l D_j^-$  such that  $D_k^+$  and  $D_j^-$   
 399 are closed convex  $n$ -dimensional polytopes,  $\overset{\circ}{D}_i^+ \cap \overset{\circ}{D}_j^+ = \emptyset$  and  $\overset{\circ}{D}_i^- \cap \overset{\circ}{D}_j^- = \emptyset$  for  $1 \leq i \neq j \leq l$ . On each  $D_k^+$   
 400 (respectively,  $D_j^-$ ),  $p_+(x)$  (respectively,  $p_-(x)$ ) is an affine function, that is,  $p_+(x) := \ell_k^+(x) = a_k^+ \cdot x + b_k^+$ ,  
 401  $x \in D_k^+$  (respectively,  $p_-(x) := \ell_j^-(x) = a_j^- \cdot x + b_j^-$ ,  $x \in D_j^-$ ). Furthermore, the affine function  $\ell_k^+(x)$

- 402 (respectively,  $\ell_j^-(x)$ ) defined in  $\mathbb{R}^n$  as above, satisfies  $\ell_k^+(x) \geq p_+(x)$  (respectively,  $\ell_j^-(x) \leq p_-(x)$ ) for  
 403  $x \in D$ .  
 404 (iv) Let  $S_k^+ \subset D_k^+$  be the set of all vertices of  $D_k^+$  for  $k = 1, \dots, m$ , then  $S_k^+ \subset S$ , and  $\cup_{k=1}^m S_k^+ = S$ . On each  
 405  $S_k^+$ ,  $p_+(x) = f_S(x)$ .  
 406 (v) Let  $S_j^- \subset D_j^-$  be the set of all vertices of  $D_j^-$  for  $j = 1, \dots, l$ , then  $S_j^- \subset S$ , and  $\cup_{j=1}^l S_j^- = S$ . On each  
 407  $S_k^-$ ,  $p_-(x) = f_S(x)$ .

408 **REMARK 4.10.** In Lemma 4.9, the piecewise affine functions  $p_+$  and  $p_-$  are replacements of  $\ell_s$  in Theorem  
 409 4.5. For the average approximation, the average  $\frac{p_+ + p_-}{2}$  of the piecewise affine functions  $p_+$  and  $p_-$  gives the new  
 410 interpolation formula in  $D = \text{co}[S]$ , replacing the affine function  $\ell_s$ . This means that our interpolation  $A_\lambda^M(f_K)$   
 411 might introduce extra nodes in  $\text{co}[S]$  in a unique way, in the sense that  $D$  is the union of  $q$   $n$ -dimensional convex  
 412 polytopes  $D_i^{av}$ ,  $i \in \{1, \dots, q\}$ , such that  $\frac{p_+ + p_-}{2}$  is affine on each  $D_i^{av}$  but not all vertices of  $D_i^{av}$  are contained in  
 413  $S$ .

414 The following is a generalisation of Theorem 4.5.

415 **THEOREM 4.11.** Let  $K = \{x_i\}_{i=1}^m \subset \mathbb{R}^n$  be a finite set with distinct points and let  $f_K : K \rightarrow \mathbb{R}$  be a function  
 416 with Lipschitz constant  $L > 0$  and bound  $A_0 > 0$ , that is,  $|f(x)| \leq A_0$  for  $x \in K$ . Suppose  $S = \{x_1, x_1, \dots, x_m\} \subset K$   
 417 generates a Delaunay cell  $\text{co}[S]$  satisfying  $\dim(\text{co}[S]) = n$  and  $\dim(\text{co}[\Gamma_s]) = n + 1$ , where  $\Gamma_s = \{(x, f_K(x)), x \in S\}$   
 418 is the graph of  $f_K$  restricted to  $S$ . Let  $B(y_s; r_s)$  be the associated open ball of the cell  $\text{co}[S]$ . Let  $p_+ : \text{co}[S] \rightarrow \mathbb{R}$  be  
 419 the piecewise affine concave function and  $p_- : \text{co}[S] \rightarrow \mathbb{R}$  be the piecewise affine convex function defined in Lemma  
 420 4.9, and let  $\text{co}[S] = \cup_{k=1}^m D_k^+$  and  $\text{co}[S] = \cup_{j=1}^l D_j^-$  be the decompositions of  $\text{co}[S]$  given by Lemma 4.9. Let

$$421 \quad C_s^+ L = \max_{1 \leq k \leq m} C_k^+ L, \quad C_s^- L = \max_{1 \leq j \leq l} C_j^- L, \quad C_s L = \max\{C_s^+ L, C_s^- L\},$$

422 where  $C_k^+ L$  and  $C_j^- L$  are the positive upper bounds given by Lemma 4.3 for  $|Dp_+(x)|$  and  $|Dp_-(x)|$ , respectively,  
 423 on  $D_k^+$  and  $D_j^-$ . Let  $\sigma_s = \min\{|x - x_s| - r_s, x \in K \setminus S\} > 0$ . Then for every  $x \in \text{co}[S]$ ,

$$424 \quad (4.6) \quad \begin{aligned} C_\lambda^u(f_K^M)(x) &= \lambda|x - x_s|^2 - \lambda r_s^2 + p_+(x), & C_\lambda^l(f_K^M)(x) &= \lambda r_s^2 - \lambda|x - x_s|^2 + p_-(x), \\ A_\lambda^M(f_K)(x) &= \frac{p_+(x) + p_-(x)}{2}, \end{aligned}$$

425 whenever

$$426 \quad (4.7) \quad \lambda > \frac{2A_0}{\sigma_s(2r_s + \sigma_s)} + \frac{C_s L}{\sigma_s}$$

427 and

$$428 \quad (4.8) \quad M > \lambda r_s^2 + C_s L r_s + A_0 + \frac{C_s^2 L^2}{4\lambda}.$$

429 **REMARK 4.12.** Under the assumptions of Lemma 4.9 and Theorem 4.11, we see that  $p_+(x)$  and  $p_-(x)$  are the  
 430 maximal and minimal piecewise affine interpolations over  $\text{co}[S]$ . It is well-known [38] that in this irregular case,  
 431 there still exist Delaunay triangulations of  $\text{co}[S]$  consisting of  $n$ -dimensional simplices, but the triangulation is not  
 432 unique. The average approximation

$$433 \quad A_\lambda^M(f_K)(x) = \frac{p_+(x) + p_-(x)}{2}$$

434 given by Theorem 4.11 is exactly the average of the maximal and minimal interpolation in a Delaunay cell.

435 **5. Inpainting revisited.** Consider now inpainting of damaged areas of an image. This is the problem where  
 436 we are given an image that is damaged in some parts and we want to reconstruct the values in the damaged part on  
 437 the basis of the known values of the image. To specify the setting of the problem, let  $\Lambda \subset \mathbb{R}^n$  be a convex compact  
 438 set representing the domain of the image  $f$  which, without loss of generality, we assume to be a grayscale image,  
 439 and is thus represented by a function  $f : \Lambda \subset \mathbb{R}^n \rightarrow \mathbb{R}$ . We assume that  $f$  is bounded and uniformly continuous.  
 440 See below, in Remark 5.2 and the comments on Example 5.3, for a discussion of this assumption in the case of an  
 441 image.

442 Denote by  $\Omega \subset \Lambda$  an open set representing the damaged areas of the image and let  $K = \Lambda \setminus \Omega$ . We have then  
 443  $\Omega \subset \text{co}[K]$ .

444 On the basis of the values of  $f$  in  $K$ , we reconstruct the values of  $f$  in  $\Omega$  by using the average approximation  
 445  $A_\lambda^M(f_K)$ . In this section, we want to assess the error of this approximation.

446 The next result, which follows from an application of Corollary 2.7, is the main error estimate for our inpainting  
 447 method.

448 **PROPOSITION 5.1.** *Let  $\Lambda \subset \mathbb{R}^n$  be a convex compact set and  $\Omega \subset \Lambda$  a non-empty open set. Assume  $f : \Lambda \subset$   
 449  $\mathbb{R}^n \rightarrow \mathbb{R}$  be bounded and uniformly continuous, such that for  $A_0 > 0$  we have that  $|f(x)| \leq A_0$  for all  $x \in K = \Lambda \setminus \Omega$ .  
 450 Let  $\tilde{f}$  be a bounded and uniformly continuous extension of  $f$  to  $\mathbb{R}^n$ , derived by the Tietze extension theorem, with  
 451  $\tilde{f}(x) = c_0$  outside an open ball  $B(0; r)$  with  $r > 0$  and such that  $K \subset B(0; r)$ . For  $R > r$ , define  $K_R = K \cup B^c(0; R)$   
 452 and let  $f_{K_R}(x) = f_K(x)$  for  $x \in K$  and  $f_{K_R}(x) = c_0$  for  $x \in B^c(0; R)$ . Denote by  $\omega$  the least concave majorant  
 453 of the modulus of continuity of  $\tilde{f}$ . Let  $a \geq 0$ ,  $b \geq 0$  be such that  $\omega(t) \leq at + b$  for  $t \geq 0$ . Then for all  $\lambda > 0$ ,  
 454  $M > A_0 + \lambda(R + r)^2$  and all  $x \in \text{co}[K]$ , we have*

$$455 \quad (5.1) \quad |A_\lambda^M(f_K)(x) - \tilde{f}(x)| \leq \omega \left( r_c(x) + \frac{a}{\lambda} + \sqrt{\frac{2b}{\lambda}} \right),$$

456 where  $r_c(x) \geq 0$  is the convex density radius of  $x$  with respect to  $K$ .

457 If we further assume that  $f$  is a globally Lipschitz function with Lipschitz constant  $L > 0$ , then for  $\lambda > 0$ ,  
 458  $M > A_0 + \lambda(R + r)^2$  and all  $x \in \text{co}[K]$ , we have

$$459 \quad (5.2) \quad |A_\lambda^M(f_{K_R})(x) - f(x)| \leq Lr_c(x) + \frac{L^2}{\lambda}.$$

460 If we further assume that  $\tilde{f}$  is a  $C^{1,1}$  function such that  $|D\tilde{f}(x) - D\tilde{f}(y)| \leq L|x - y|$  for all  $x, y \in \mathbb{R}^n$  with  $L > 0$   
 461 the Lipschitz constant of  $D\tilde{f}$ , then for  $\lambda > L$ ,  $M > A_0 + \lambda(R + r)^2$  and all  $x \in \text{co}[K]$ , we have

$$462 \quad (5.3) \quad |A_\lambda^M(f_{K_R})(x) - \tilde{f}(x)| \leq \frac{L}{4} \left( \frac{\lambda + L/2}{\lambda - L/2} + 1 \right) r_c^2(x).$$

463 Furthermore, in this case,  $A_\lambda^M(f_{K_R})$  is an interpolation of  $f_K$  in  $\mathbb{R}^n$ .

464 **REMARK 5.2.** (i) Using (2.9), it follows that the estimates (5.1) and (5.3) hold with  $r_c(x)$  replaced by  
 465  $d(x)$ . Although the resulting estimates are less sharp, they have a clearer meaning in light of the geometric  
 466 interpretation of the gap  $d(x)$ .

467 (ii) While the assumption of boundedness of the image  $f$  is a plausible one, the assumption on the continuity of  $f$   
 468 seems to be less reasonable for applications to images which might have sharp changes in grayscale intensity.  
 469 However, Example 5.3 at the end of this section, illustrates the fact that our average approximation operator  
 470 well approximates jump discontinuities.

471 It is interesting to compare our error estimates (5.1) and (5.3) with the error analysis for image inpainting discussed  
 472 in [15]. Let  $\Omega \subset \mathbb{R}^2$  be a smooth domain, which is the damaged area of the image to be reconstructed, and let  $u$  be

473 a  $C^2$  function in a larger domain containing  $\bar{\Omega}$ . Let  $u_0 = u$  on  $\partial\Omega$  and consider the solution  $v$  of the boundary value  
 474 problem  $\Delta v(x) = 0$  with  $v = u_0$  on  $\partial\Omega$ . The function  $v$  is the reconstruction of  $u$  within  $\Omega$ . The error estimate  
 475 obtained in [15] is then given by

$$476 \quad (5.4) \quad |v(x) - u(x)| \leq \frac{T\beta^2}{4}, \quad x \in \Omega,$$

477 where  $T = \max\{|\Delta u(x)|, x \in \bar{\Omega}\}$  and  $\beta$  is the shorter semi-axis of any ellipse covering  $\Omega$ . [15] also contains  
 478 variations of estimate (5.4) by deforming (if possible) a general long thin domain into one for which  $\beta$  is reasonably  
 479 small.

480 Note that in light of Remark 5.2(i), the error bound (5.3) depends explicitly on  $d(x)$  and the Lipschitz constant  $L$  of  
 481 the gradient  $D\tilde{f}$ , which is comparable with the bound  $T$  for the Laplacian of  $u$ . Moreover, our assumptions on the  
 482 smoothness of the domain  $\Omega$  and the underlying function are weaker than those considered in [15]. In fact, we do  
 483 not require any smoothness of the boundary  $\partial\Omega$ . Our estimate is particularly sharp for more general thin domains  
 484 given its dependence on  $d(x)$ . As remarked in [15], the short semi-axis  $\beta^2$  used in the error estimate for harmonic  
 485 inpainting cannot be replaced by  $d^2(x)$  which better accounts for the geometric structure of the damaged area to  
 486 be inpainted. Due to the Hausdorff stability property of the average approximation (see [55, Theorem 4.12]), if  $\Omega_\epsilon$   
 487 is another domain whose Hausdorff distance to  $\Omega$  is small, we can also obtain similar results to estimate (5.3) for  
 488 such domains.

489 Reference [15] contains also error estimates for the TV inpainting model using the energy  $\int_\Omega |v(x)|dx$  under the  
 490 Dirichlet condition  $v|_{\partial\Omega} = u_0$ . However, it is not clear how such estimates can be made rigorous. Comparing  
 491 with Proposition 5.1 where we assumed the underlying function to be bounded and uniformly continuous, the TV  
 492 model, in contrast, allows the function to have jumps, thus the TV inpainting model tries to preserve such jump  
 493 discontinuities. However, such a model cannot be Hausdorff stable. Also, in order to establish the existence of  
 494 solutions for this model, we note that the boundary condition has to be relaxed. Even for the more regular minimal  
 495 graph energy  $\int_\Omega \sqrt{1 + |Dv(x)|^2}dx$ , existence of solutions for the Dirichlet problem may not be guaranteed [31].  
 496 On the other hand, the average approximation always exists and is unique. See Example 6.5 in Section 6 for an  
 497 illustration of this.

498 Compared with our model for inpainting, we also note that for the relaxed Dirichlet problem of the minimal graph  
 499 or of the TV model, as the boundary value of the solution does not have to agree with the original boundary value,  
 500 extra jumps can be introduced along the boundary. By comparison, since our average approximation is continuous,  
 501 it will not introduce such a jump discontinuity at the boundary.

502 One of the motivations for using TV related models [17] for the inpainting problem is that functions of bounded  
 503 variations can have jump discontinuities [3]. Some authors argue that continuous functions cannot be used to  
 504 model digital image related functions as functions representing images may have jumps [17]. However, from the  
 505 human vision perspective, it is hard to distinguish between a jump discontinuity, where values change abruptly,  
 506 and a continuous function with sharp changes within a very small transition layer. The following is a simple one-  
 507 dimensional example showing the effects of our upper, lower and average compensated convex transforms on a jump  
 508 function. More explicitly calculated prototype examples of inpainting by using our method over jump discontinuity  
 509 and continuous edges are given in Section 6.

510 **EXAMPLE 5.3.** Let  $f(x) = \text{sign}(x)$  be the sign function defined by  $\text{sign}(x) = 1$  if  $x > 0$ ,  $\text{sign}(x) = -1$  if  $x < 0$ .

511 For  $\lambda > 0$ , we have

$$\begin{aligned}
 C_\lambda^l(f)(x) &= \begin{cases} -1, & x \leq 0, \\ 1 - \lambda(x - \sqrt{2/\lambda})^2, & 0 \leq x \leq \sqrt{2/\lambda}, \\ 1, & x \geq \sqrt{2/\lambda}; \end{cases} \\
 C_\lambda^u(f)(x) &= \begin{cases} -1, & x \leq -\sqrt{2/\lambda}, \\ \lambda(x + \sqrt{2/\lambda})^2 - 1, & -\sqrt{2/\lambda} \leq x \leq 0, \\ 1, & x \geq 0; \end{cases} \\
 \frac{1}{2}(C_\lambda^l(f)(x) + C_\lambda^u(f)(x)) &= \begin{cases} -1, & x \leq -\sqrt{2/\lambda}, \\ \frac{\lambda}{2}(x + \sqrt{2/\lambda})^2 - 1, & -\sqrt{2/\lambda} \leq x \leq 0, \\ 1 - \frac{\lambda}{2}(x - \sqrt{2/\lambda})^2, & 0 \leq x \leq \sqrt{2/\lambda}, \\ 1, & x \geq \sqrt{2/\lambda}; \end{cases}
 \end{aligned}
 \tag{5.5}$$

513 Figure 1 displays the graphs of these transforms with  $\lambda = 100$  which give very good approximations of the  
 514 jump function with the square of the  $L^2$ -error equal to  $2\sqrt{2}/(5\sqrt{\lambda})$  for the average approximation and equal to  
 515  $\sqrt{2}/(5\sqrt{\lambda})$  for the lower and upper transform. Therefore these transforms can be used quite well to replace the jump  
 516 discontinuity. For further prototype examples of inpainting with jump discontinuity, see Section 6.

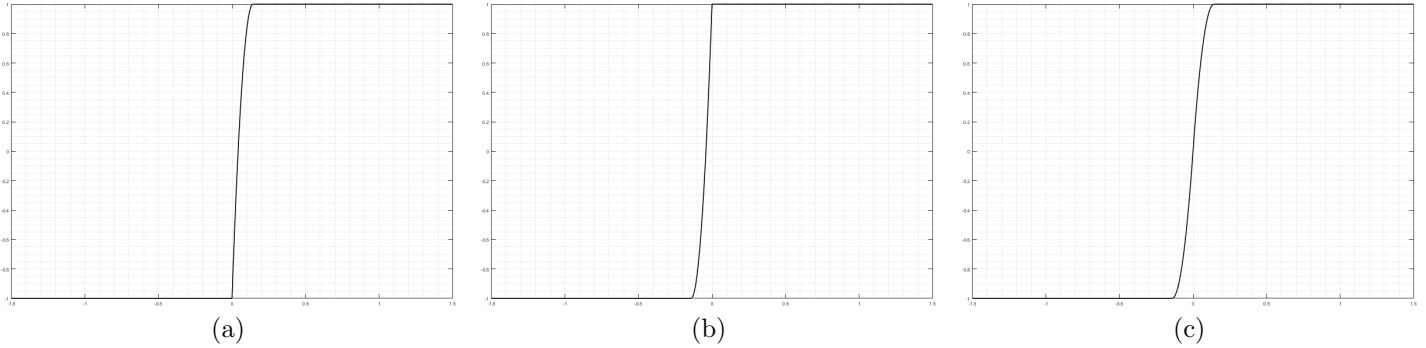


FIGURE 1. (a) Lower transform of the sign function for  $\lambda = 100$ . (b) Upper transform of the sign function for  $\lambda = 100$ . (c) Average approximation of the sign function for  $\lambda = 100$ .

517 We conclude this section by presenting a result on inpainting in bounded convex domains which we state only for  
 518 continuous functions defined on the closure of the domain. For Lipschitz and  $C^{1,1}$  functions, similar results can be  
 519 established.

520 **COROLLARY 5.4.** *Suppose  $\Omega \subset \mathbb{R}^n$  is a non-empty, bounded, open and convex set and  $U \subset \bar{U} \subset \Omega$  is an open*  
 521 *subset whose closure  $\bar{U}$  is contained in  $\Omega$ . Suppose  $f : \bar{\Omega} \rightarrow \mathbb{R}$  is a continuous function. Let  $\tilde{f}$  be any bounded*  
 522 *uniformly continuous extension of  $f$  to  $\mathbb{R}^n$  and  $\omega$  be the least concave majorant of the modulus of continuity of  $\tilde{f}$*   
 523 *which is itself a modulus of continuity. Let  $K = \bar{\Omega} \setminus U$  and define for  $M > 0$*

$$f_K^{M,\infty}(x) = \begin{cases} f(x), & x \in K, \\ M, & x \in U, \\ +\infty, & x \in \mathbb{R}^n \setminus \bar{\Omega}, \end{cases} \quad f_K^{-M,-\infty}(x) = \begin{cases} f(x), & x \in K, \\ -M, & x \in U, \\ -\infty, & x \in \mathbb{R}^n \setminus \bar{\Omega}. \end{cases}$$

525 Then the average approximation in  $\bar{\Omega}$  defined by

$$526 \quad (5.6) \quad A_\lambda^{M;\infty}(f_K)(x) = \frac{1}{2} \left( C_\lambda^l(f_K^{M,+ \infty})(x) + C_\lambda^u(f_K^{-M,- \infty})(x) \right)$$

527 for  $x \in \bar{\Omega}$  satisfies

$$528 \quad |A_\lambda^{M;\infty}(f_K)(x) - f(x)| \leq \omega(r_c(x) + a/\lambda + \sqrt{b/\lambda})$$

529 for all  $x \in \bar{\Omega}$ , where  $r_c(x)$  is the convex density radius of  $x \in \bar{\Omega}$  with respect to  $K$ .

530 **REMARK 5.5.** The average approximation defined by (5.6) is the same average approximation as defined on the  
531 bounded domain  $\bar{\Omega}$

$$532 \quad A_\lambda^M(f_K; \bar{\Omega})(x) = \frac{1}{2} \left( C_\lambda^l(f_K^M; \bar{\Omega})(x) + C_\lambda^u(f_K^{-M}; \bar{\Omega})(x) \right)$$

533 for  $x \in \bar{\Omega}$ , where  $f_K^M(x)$  and  $f_K^{-M}(x)$  are defined by (1.2), restricted to  $\bar{\Omega}$ . We can also state the average approxi-  
534 mation under the Dirichlet boundary condition in a similar way. We leave this to interested readers.

535 **6. Prototype Models.** In this section we present explicitly calculated average approximations for some  
536 particular simple functions of two variables. Recall that such approximations  $A_\lambda^\infty(f_K)$  are obtained by first finding  
537 lower and upper compensated convex transforms and then taking their arithmetic mean, and that the approximation  
538 properties of  $A_\lambda^\infty(f_K)$  hold for  $(x, y) \in \text{co}[K]$ . For some examples we also give expressions for the constituent lower  
539 and upper transforms to help illustrate the construction of the approximations. Such examples serve the dual  
540 purpose of providing insight into this new class of approximations based on compensated convexity transforms,  
541 and of verifying numerical methods for computing such approximations. In fact, in Section 7 below, we will see  
542 numerical examples that show that, at a sufficient level of magnification, the conditions that occur in practice for  
543 the approximation of general functions often look essentially like one of these prototypes.

#### 544 6.1. Simple prototypes.

545 **EXAMPLE 6.1.** These two examples give average approximations  $A_\lambda^\infty(f_K)$  for simple sampled functions over  
546 non-regular Delaunay cells. In each case, the average approximation is an interpolation of the sampled function  
547 values.

548 (i) Consider the four point set  $K = \{(\pm 1, 0), (0, \pm 1)\}$  and define  $f_K(1, 0) = f_K(0, 1) = 1$  and  $f_K(-1, 0) =$   
549  $f_K(0, -1) = -1$ . The upper and lower compensated convex transforms are then for  $\lambda > 0$

$$550 \quad \begin{aligned} C_\lambda^l(f_K^\infty)(x, y) &= \begin{cases} 2\lambda - 1 - x + y - \lambda(x^2 + y^2), & \text{if } x \geq -1, y \leq 1 \text{ and } x \leq y, \\ 2\lambda - 1 + x - y - \lambda(x^2 + y^2), & \text{if } y \geq -1, x \leq 1 \text{ and } x \geq y, \\ +\infty, & \text{if } |x| > 1 \text{ or } |y| > 1; \end{cases} \\ C_\lambda^u(f_K^{-\infty})(x, y) &= \begin{cases} -2\lambda + 1 + x + y + \lambda(x^2 + y^2), & \text{if } x \geq -1, y \geq -1 \text{ and } x + y \leq 0, \\ -2\lambda + 1 - x - y + \lambda(x^2 + y^2), & \text{if } x \leq 1, y \leq 1 \text{ and } x + y \geq 0, \\ -\infty, & \text{if } |x| > 1 \text{ or } |y| > 1. \end{cases} \end{aligned}$$

551 so that, for  $(x, y) \in D := \text{co}[K] = \{(x, y) \in \mathbb{R}^2 : |x| \leq 1, |y| \leq 1\}$ , we have

$$552 \quad A_\lambda^\infty(f_K)(x, y) = \begin{cases} y, & \text{if } x \leq y \text{ and } x + y \leq 0, \\ -x, & \text{if } x \leq y \text{ and } x + y \geq 0, \\ x, & \text{if } x \geq y \text{ and } x + y \leq 0, \\ -y, & \text{if } x \geq y \text{ and } x + y \geq 0. \end{cases}$$

553 This is the continuous piecewise affine interpolation of  $f_K$  inside the square  $D$ . The graph of  $A_\lambda^\infty(f_K)$  is  
554 shown in Figure 2(a).

555 (ii) Consider the eight point set  $K \subset \mathbb{R}^2$  consisting of the eight points on the unit circle with polar angles  $k\pi/4$ ,  
 556  $k = 0, 1, 2, \dots, 7$ , and define  $f_K(\cos(k\pi/4), \sin(k\pi/4)) = (-1)^k$ . The upper and lower compensated convex  
 557 transforms are then for  $\lambda > 0$

$$\begin{aligned}
 C_\lambda^l(f_K^\infty)(x, y) &= \begin{cases} \frac{\sqrt{2}+1}{\sqrt{2}-1} - \frac{2|y|}{\sqrt{2}-1} & \text{if } |x| \leq 1, |y| \geq 1 \text{ and } |y| + (\sqrt{2}-1)|x| \leq \sqrt{2}, \\ \frac{\sqrt{2}+1}{\sqrt{2}-1} - \frac{2|x|}{\sqrt{2}-1} & \text{if } |y| \leq -1, |x| \geq 1 \text{ and } |x| + (\sqrt{2}-1)|y| \leq \sqrt{2}, \\ 1 & \text{if } |x| \leq 1, \text{ and } |y| \leq 1 \\ 0 & \text{otherwise;} \end{cases} \\
 C_\lambda^u(f_K^{-\infty})(x, y) &= \begin{cases} \frac{\sqrt{2}+1}{\sqrt{2}-1} - \frac{\sqrt{2}|x-y|}{\sqrt{2}-1} & \text{if } |x+y| \leq \sqrt{2}, |x-y| \geq \sqrt{2} \text{ and} \\ & |x-y| + (\sqrt{2}-1)|x+y| \leq 2, \\ \frac{\sqrt{2}+1}{\sqrt{2}-1} - \frac{\sqrt{2}|x+y|}{\sqrt{2}-1} & \text{if } |x+y| \geq \sqrt{2}, |x-y| \geq \sqrt{2} \text{ and} \\ & |x+y| + (\sqrt{2}-1)|x-y| \leq 2, \\ 1 & \text{if } |x+y| \leq \sqrt{2} \text{ and } |x-y| \leq \sqrt{2} \\ 0 & \text{otherwise;} \end{cases}
 \end{aligned}$$

559 whereas  $A_\lambda^\infty(f_K)(x, y)$  is obtained by taking the arithmetic mean of  $C_\lambda^l(f_K^\infty)(x, y)$  and  $C_\lambda^u(f_K^{-\infty})(x, y)$ .  
 560 Figure 2(b) shows the graph of  $A_\lambda^\infty(f_K)$  in  $\text{co}[K]$ , which is the inside of the regular octagon with vertices  
 561 at the eight points of  $K$ . As in (i),  $A_\lambda^\infty(f_K)$  is a continuous piecewise affine interpolation of  $f_K$  in  $\text{co}[K]$ .

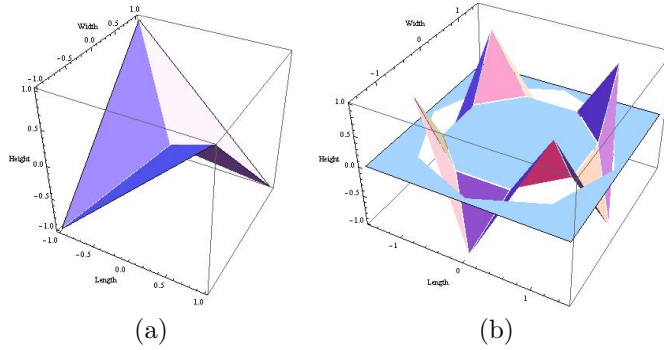


FIGURE 2. Graphs of the average approximation operators  $A_\lambda^\infty(f_K)$  in Example 6.1, when  $K$  is (a) a four point set on the circle of unit radius and (b) an eight point set on the circle of unit radius. In both (a) and (b), the average approximation operator is an interpolation operator over  $\text{co}[K]$ .

562 EXAMPLE 6.2. These two examples give average approximations  $A_\lambda^\infty(f_K)$  for unbounded sets  $K$  with  $\text{co}[K] =$   
 563  $\mathbb{R}^2$ .

564 (i) Consider the set  $K = \ell_- \cup \ell_+$  with  $\ell_- = \{(x, x), x \in \mathbb{R}\}$ ,  $\ell_+ = \{(y, -y), y \in \mathbb{R}\}$ , and define  $f_K(x, x) = -x^2$   
 565 and  $f_K(y, -y) = y^2$ . To simplify the calculations, first consider the scaled and rotated function  $g_{\tilde{K}}$  defined  
 566 on the set  $\tilde{K} = \{(x, 0), x \in \mathbb{R}\} \cup \{(0, y), y \in \mathbb{R}\}$ , with  $g_{\tilde{K}}(x, 0) = -x^2$  and  $g_{\tilde{K}}(0, y) = y^2$ . Then for  
 567  $(x, y) \in \mathbb{R}^2$ , the lower and upper compensated convex transforms of  $g_{\tilde{K}}$  are

$$568 \quad C_\lambda^l(g_{\tilde{K}}^\infty)(x, y) = y^2 + 2|x||y| - x^2, \quad C_\lambda^u(g_{\tilde{K}}^{-\infty})(x, y) = y^2 - 2|x||y| - x^2,$$

569 and the average approximation of  $g_{\bar{K}}$  is

$$570 \quad A_{\lambda}^{\infty}(g_{\bar{K}})(x, y) = \frac{1}{2} \left( C_{\lambda}^l(g_{\bar{K}}^{\infty})(x, y) + C_{\lambda}^u(g_{\bar{K}}^{-\infty})(x, y) \right) = y^2 - x^2.$$

571 The average approximation  $A_{\lambda}^{\infty}(f_K)$  of  $f_K$  is then obtained from  $A_{\lambda}^{\infty}(g_{\bar{K}})$  via a change of variables, and is

$$572 \quad A_{\lambda}^{\infty}(f_K)(x, y) = \frac{1}{2} \left( A_{\lambda}^{\infty}(g_{\bar{K}}) \left( \frac{x+y}{\sqrt{2}}, \frac{x-y}{\sqrt{2}} \right) \right) = -xy.$$

573 Figure 3(a) shows the graph of  $A_{\lambda}^{\infty}(f_K)$ .

574 (ii) Let  $K = \{(x, 0), x \in \mathbb{R}\} \cup \{(0, y), y \in \mathbb{R}\}$  and define  $f_K$  by  $f_K(x, 0) = |x|$  for  $x \in \mathbb{R}$  and  $f_K(0, y) = -|y|$   
575 for  $y \in \mathbb{R}$ . For  $(x, y) \in \mathbb{R}^2$ , the lower and upper compensated convex transforms of  $f_K$  are

$$576 \quad \begin{aligned} C_{\lambda}^l(f_K^{\infty})(x, y) &= \begin{cases} 2|x| - \frac{1}{4\lambda} - \lambda(x^2 + y^2), & \text{if } |x| + |y| \leq \frac{1}{2\lambda}, \\ |x| + 2\lambda|x||y| - |y|, & \text{if } |x| + |y| \geq \frac{1}{2\lambda}, \end{cases} \\ C_{\lambda}^u(f_K^{-\infty})(x, y) &= \begin{cases} -2|y| + \frac{1}{4\lambda} + \lambda(x^2 + y^2), & \text{if } |x| + |y| \leq \frac{1}{2\lambda}, \\ |x| - 2\lambda|x||y| - |y|, & \text{if } |x| + |y| \geq \frac{1}{2\lambda}, \end{cases} \end{aligned}$$

577 and the average approximation operator is

$$578 \quad A_{\lambda}^{\infty}(f_K)(x, y) = |x| - |y|,$$

579 which here coincides with the natural interpolation of  $f_K$  by the piecewise affine function  $f(x, y) = |x| - |y|$ ,  
580  $(x, y) \in \mathbb{R}^2$ . The graph of  $A_{\lambda}^{\infty}(f_K)$  is shown in Figure 3(b).

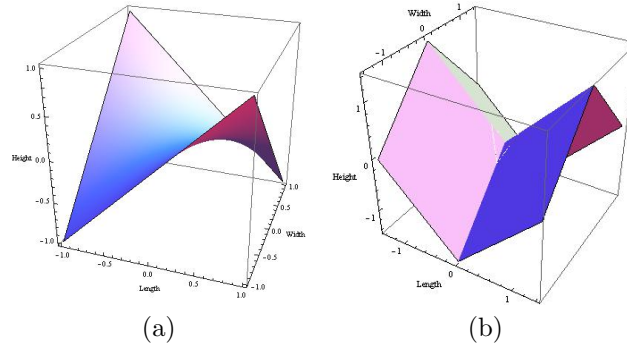


FIGURE 3. Graphs of the average approximation operators  $A_{\lambda}^{\infty}(f_K)$  in Example 6.2(i) and (ii), respectively.

581 **6.2. Inpainting prototypes.** Examples 6.3 and 6.4 are prototype models for the inpainting problem. Our  
582 question is, to what extent our method can preserve singularities on the boundary based on the given boundary  
583 values. Our calculations show that if the domain is narrow and similar singular boundary values appear on both  
584 sides of the narrow gap, the inpainting function  $A_{\lambda}^{\infty}(f_K)$  can preserve the singular shape across the gap, subject  
585 to a  $\lambda$ -dependent regularisation of the singularity due to the local smoothing effect of the compensated convex  
586 transforms.

587 **EXAMPLE 6.3.** (i) For  $r > 0$ ,  $h > 0$ , let  $K = \{(\pm r, y), |y| \leq h\} \subset \mathbb{R}^2$  i.e. two parallel line segments a  
588 distance  $r$  apart (see Figure 4(a)), and define  $f_K(\pm r, y) = 1 - |y|$ . Let  $D = \text{co}[K] = \{(x, y) \in \mathbb{R}^2 : |x| \leq$

589  $r, |y| \leq h\}$ . Then for  $\lambda > 1/2h$ ,

$$\begin{aligned}
 C_\lambda^l(f_K^\infty)(x, y) &= \begin{cases} 1 - \frac{1}{4\lambda} + \lambda r^2 - \lambda x^2 - \lambda y^2, & \text{if } |x| \leq r \text{ and } |y| \leq \frac{1}{2\lambda}, \\ 1 + \lambda r^2 - \lambda x^2 - |y|, & \text{if } |x| \leq r \text{ and } \frac{1}{2\lambda} \leq |y| \leq h, \\ +\infty & \text{otherwise,} \end{cases} \\
 C_\lambda^u(f_K^\infty)(x, y) &= \begin{cases} 1 - \lambda r^2 + \lambda x^2 - |y|, & \text{if } |x| \leq r \text{ and } |y| \leq h; \\ -\infty & \text{otherwise,} \end{cases}
 \end{aligned}$$

591 and for  $(x, y) \in D$ , the average approximation operator is

$$A_\lambda^\infty(f_K)(x, y) = \begin{cases} 1 - \frac{1}{8\lambda} - \frac{\lambda y^2}{2} - \frac{|y|}{2}, & \text{if } |x| \leq r \text{ and } |y| \leq \frac{1}{2\lambda}, \\ 1 - |y|, & \text{if } |x| \leq r, \text{ and } \frac{1}{2\lambda} \leq |y| \leq h. \end{cases}$$

593 The graph of  $A_\lambda^\infty(f_K)$  is shown in Figure 4(b).

594

595 Note that this example shows that if we only sample the two gables  $K$  of the roof, the whole roof can be  
 596 recovered well for any  $r > 0$  and  $h > 0$ . On the other hand, we will see in the next example that the  
 situation is more complicated if the other two sides,  $(x, \pm h)$  for  $|x| \leq r$ , are added to the sample set.

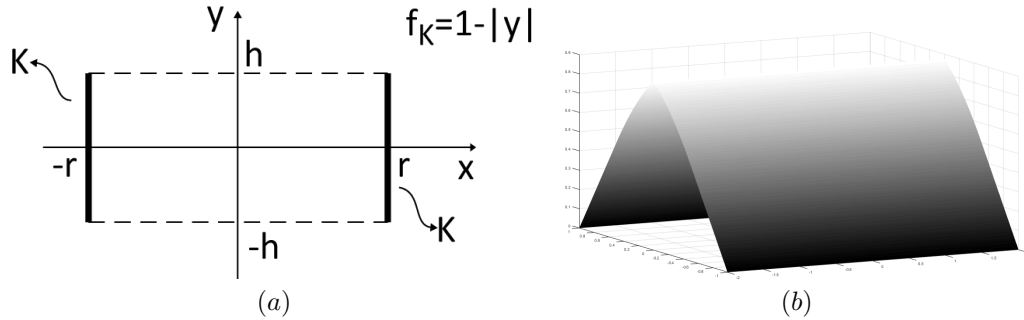


FIGURE 4. Example 6.3(i). (a) The sample set  $K$  shown in bold, with the sample function  $f_K = 1 - |y|$ . (b) Graph of  $A_\lambda^\infty(f_K)$  for  $\lambda = 1$ .

597

598 (ii) Next let  $D = \{(x, y), |x| \leq r, |y| \leq h\}$  with  $h > 0$  and  $r > 0$ , take the sample set  $K = \partial D = \{(\pm r, y), |y| \leq$   
 599  $h\} \cup \{(x, \pm h), |x| \leq r\}$ , and define

$$f_K(x, y) = \begin{cases} h - |y|, & x = \pm r, |y| \leq h, \\ 0, & y = \pm h, |x| \leq r. \end{cases}$$

601 For large  $\lambda$ , the shape of  $A_\lambda^\infty(f_K(x, y))$  in  $D$  now depends on whether  $h > r$ ,  $h < r$  or  $h = r$ .

602 (a) If  $h > r$ , the two gables of the roof  $h - |y|$  at  $x = \pm r$  are close to each other and we have a very good  
 603 approximation of the whole roof  $h - |y|$  for  $(x, y) \in D$  when  $\lambda$  is sufficiently large. For  $(x, y) \in D$ , the  
 604 approximation  $A_\lambda^\infty(f_K(x, y))$  is

$$A_\lambda^\infty(f_K)(x, y) = \begin{cases} h - \frac{1}{4\lambda} - \lambda y^2, & \text{if } |y| \leq \frac{1}{2\lambda} \text{ and } |x| \leq r, \\ h - |y|, & \text{if } \frac{1}{2\lambda} \leq |y| \leq h \text{ and } |x| \leq r, \end{cases}$$

606 which yields the explicit error estimate

$$|A_\lambda^\infty(f_K)(x, y) - f(x, y)| \leq \frac{1}{8\lambda}.$$

608

*In particular, the ridge of the roof is preserved well in this case.*

609

(b) *If  $h = r$  and  $\lambda > 0$  is large, the roof dips in the middle, while the ‘ridge’ is still preserved.*

610

(c) *If  $h < r$  and  $\lambda > 0$  is large, the roof falls inside  $D = \text{co}[K]$  and touches the ground. In this case, the ridge is no longer preserved at all.*

611

612

*In summary, the average approximation can approximate well the non-smooth function given on two sides of  $K$  provided the two gables are close enough. In this case, we could say that by symmetry we have a behaviour similar to the one seen in Example 6.3(a). As opposite, when the two gables are far apart, i.e. when  $h/r < 1$ , it is somehow the effect of  $f_K = 0$  on the sides  $y = \pm h$  to make it feel its presence, by having a zero interpolation in the middle of the domain. We stress again that this situation is different from the one seen in Example 6.3(a) where  $f_K$  was sampled only on the sides  $x = \pm r$ . Figure 5 shows the graphs of  $A_\lambda^\infty$  in each of the three cases, together with the sample set  $K$ .*

613

614

615

616

617

618

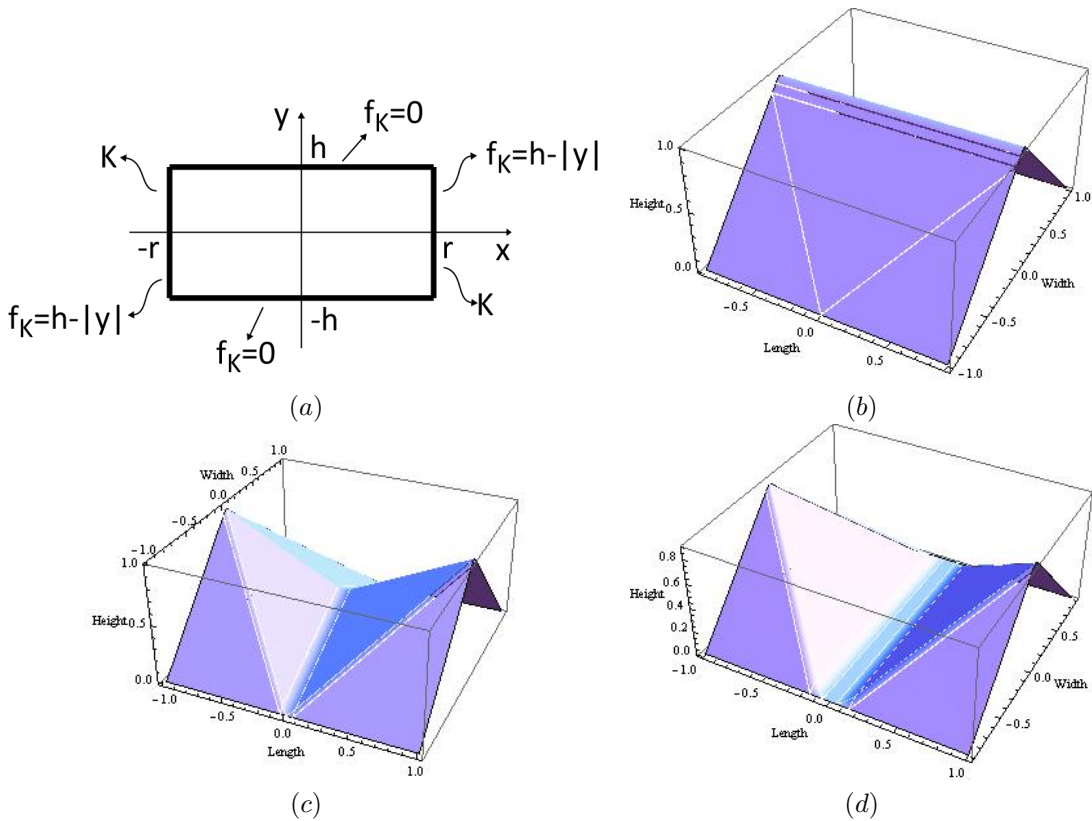


FIGURE 5. Example 6.3(ii). (a) The sample set  $K$  shown in bold, with the sample function  $f_K$ . Average approximation in  $D$  for the following parameters: (b)  $h = 1$ ,  $r = 0.9$ ,  $\lambda = 10$ . (c)  $h = 1$ ,  $r = 1$ ,  $\lambda = 10$ . (d)  $h = 0.9$ ,  $r = 1$ ,  $\lambda = 10$ .

619

A preliminary one-dimensional prototype of the inpainting of a region when the boundary values have discontinuities was given in Example 5.3. We next explore how our inpainting method can preserve jumps in a two-dimensional example.

620

621

622

EXAMPLE 6.4. Consider the inpainting of the region  $D = \{(x, y), |x| \leq r, |y| \leq h\}$ , for  $r, h > 0$ , in the case of narrow gap, that is, when  $h < r$ . The sample set is the boundary of the domain  $D$ , that is,  $K = \partial D$ , and the sample function  $f_K$  is taken as  $f_K(x, y) = \text{sign}(x)$ . Then for  $\lambda > 0$  large enough, the average approximation operator is in

623

624

625 fact given by (5.5), that is, for  $(x, y) \in D$ ,

$$626 \quad A_\lambda^\infty(f_K)(x, y) = \begin{cases} -1, & \text{if } x \leq -\sqrt{2/\lambda} \text{ and } |y| \leq h, \\ \frac{\lambda}{2}(x + \sqrt{2/\lambda})^2 - 1, & \text{if } -\sqrt{2/\lambda} \leq x \leq 0 \text{ and } |y| \leq h, \\ 1 - \frac{\lambda}{2}(x - \sqrt{2/\lambda})^2, & \text{if } 0 \leq x \leq \sqrt{2/\lambda} \text{ and } |y| \leq h, \\ 1, & \text{if } x \geq \sqrt{2/\lambda} \text{ and } |y| \leq h. \end{cases}$$

627 Figure 6(a) shows the graph of the average approximation  $A_\lambda^\infty(f_K)$  in this case. The approximation  $A_\lambda^\infty(f_K)(x, y)$   
 628 is different from  $\text{sign}(x)$  in the range  $[-\sqrt{2/\lambda}, \sqrt{2/\lambda}] \times [-h, h]$  due to the smoothing effect of the compensated  
 629 transform in the neighbourhood of the singularity. The width of such a neighbourhood depends on  $\sqrt{\lambda}^{-1}$ . The full  
 630 recovery of the sign function in  $D$  requires taking the limit  $\lim_{\lambda \rightarrow \infty} A_\lambda^\infty(f_K)(x, y)$ .

631 Note that if, on the other hand,  $h > r$ , the gap is ‘wide’ and the graph of  $A_\lambda^\infty(f_K)$  starts to collapse in the middle of  
 632 the domain, similar to what happens in Example 6.3(ii)(c). In the collapsed region, the approximation looks like an  
 633 affine function connecting the two sides  $\{x = \pm r\}$  of  $D$  on which  $f_K$  is given by the constants  $+1$ , when  $x = +r$ ,  
 634 and  $-1$ , when  $x = -r$ .

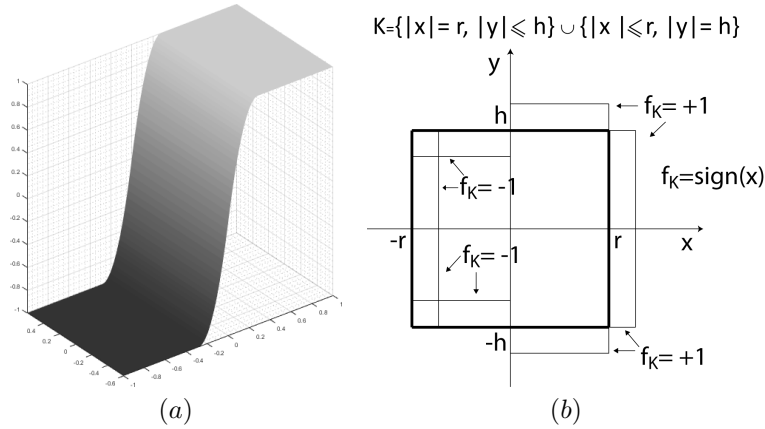


FIGURE 6. Example 6.4. Inpainting in the closed set  $D = \{(x, y), |x| \leq l, |y| \leq h\}$  by the boundary value of the sign function on the sample set  $K = \partial D$ . (a) Graph of  $A_\lambda^\infty(f_K)$  for  $h = 0.6, r = 1, \lambda = 25$ , showing that the jump is preserved across the domain  $D$ . (b) Sample set  $K$  shown in bold with the sampled function  $f_K = \text{sign}(x)$ .

636 **6.3. Level-set prototypes.** We next present prototype models for the approximation of functions sampled  
 637 on contour lines.

638 EXAMPLE 6.5. This example examines the behaviour of  $A_\lambda^\infty(f_K)$  when the contour lines of  $f$  are (i) smooth  
 639 and (ii) not smooth.

640 (i) For  $0 < r < R$ , let  $K = \Gamma_r \cup \Gamma_R$  with  $\Gamma_r$  and  $\Gamma_R$  circles of radius  $r$  and  $R$ , respectively, as displayed in  
 641 Figure 7(a), and define the sample function  $f_K$  by  $f_K(x, y) = 0$  for  $(x, y) \in \Gamma_r$  and  $f_K(x, y) = M > 0$  if

642  $(x, y) \in \Gamma_R$ . Then for  $\lambda > M/(R^2 - r^2)$ ,

$$C_\lambda^u(f_K^{-\infty})(x, y) = \begin{cases} M + \lambda(x^2 + y^2 - r^2), & \text{if } \sqrt{x^2 + y^2} \leq r, \\ \lambda(x^2 + y^2 - R^2) + \frac{M + \lambda(R^2 - r^2)}{R - r}(R - \sqrt{x^2 + y^2}), & \text{if } r \leq \sqrt{x^2 + y^2} \leq R, \end{cases}$$

643

$$C_\lambda^l(f_K^\infty)(x, y) = \begin{cases} M + \lambda(r^2 - x^2 - y^2), & \text{if } \sqrt{x^2 + y^2} \leq r, \\ \lambda(R^2 - x^2 - y^2) - \frac{\lambda(R^2 - r^2) - M}{R - r}(R - \sqrt{x^2 + y^2}), & \text{if } r \leq \sqrt{x^2 + y^2} \leq R, \end{cases}$$

644

so that for  $(x, y) \in D = \text{co}[K] = \{(x, y) : x^2 + y^2 \leq R^2\}$ , the average approximation  $A_\lambda^\infty(f_K)$  is

$$A_\lambda^\infty(f_K)(x, y) = \begin{cases} M, & \text{if } \sqrt{x^2 + y^2} \leq r, \\ \frac{M(R - \sqrt{x^2 + y^2})}{R - r}, & \text{if } r \leq \sqrt{x^2 + y^2} \leq R. \end{cases}$$

646

The graph of  $A_\lambda^\infty(f_K)$  is shown in Figure 7(b).

647

Note that a common method for the interpolation of function values assigned on contour lines is to solve the Dirichlet problem for the minimal surface equation  $\text{div} \frac{Du}{\sqrt{1+|Du|^2}} = 0$  over the annulus domain  $r \leq$

648

$\sqrt{x^2 + y^2} \leq R$  with boundary conditions  $u(x, y) = 0$  if  $(x, y) \in \Gamma_r$  and  $u(x, y) = M$  if  $(x, y) \in \Gamma_R$ . It is then known that this problem does not have a regular solution [31]. Moreover, the interpolation obtained by solving the total variation equation  $\text{div} \frac{Du}{|Du|} = 0$  faces the same type of issue, because to obtain its

649

numerical solution, the denominator  $|Du|$  is usually replaced by the term  $\sqrt{\epsilon^2 + |Du|^2}$ , thus obtaining the scaled minimal surface equation  $\text{div} \frac{Du}{\sqrt{\epsilon^2 + |Du|^2}} = 0$  whose solution, as mentioned above, may not be regular.

650

As a result, these models must be relaxed and one must look for generalised solutions [30]. In contrast, the method we propose yields the natural, easy to compute and expected interpolation  $A_\lambda^\infty(f_K)$  between the two level lines.

651

652

653

654

655

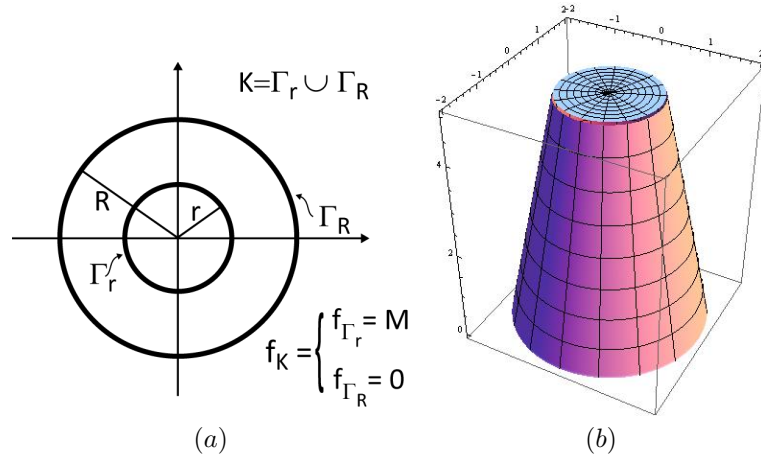


FIGURE 7. Example 6.5(i). (a) Sample set  $K$  given by the two circular level lines  $\Gamma_r$  and  $\Gamma_R$  with  $f_K(x, y) = 0$  for  $(x, y) \in \Gamma_r$  and  $f_K(x, y) = M > 0$  if  $(x, y) \in \Gamma_R$ . (b) Graph of  $A_\lambda^\infty(f_K)$  with  $r = 1$ ,  $R = 2$ ,  $M = 5$  and  $\lambda = 10$ .

656

657

658

(ii) For  $a, \lambda > 0$ , consider the sample set  $K = K_1 \cup K_2$  with  $K_1 = \{(x, y) : |y| = ax, x \geq 0\}$  and  $K_2 = \{(x, y) : |y| = a(x - \frac{\sqrt{1+a^2}}{a\sqrt{\lambda}}), x \geq \frac{\sqrt{1+a^2}}{a\sqrt{\lambda}}\}$ , and define the sample function  $f_K$  by  $f_K(x, y) = 1$  for

659  $(x, y) \in K_1$  and  $f_K(x, y) = 2$  for  $(x, y) \in K_2$ . The set  $K$  along with  $f_K$  are shown in Figure 8(a). For  
 660  $(x, y) \in D = \text{co}[K] = \{(x, y) : |y| \leq ax, x \geq 0\}$ , the average approximation operator  $A_\lambda^\infty(f_K)$  is

$$661 \quad A_\lambda^\infty(f_K)(x, y) = \begin{cases} 1, & \text{if } |y| \leq ax \text{ and } 0 \leq x \leq \frac{1}{a\sqrt{1+a^2}}, \\ 1 + \frac{\sqrt{1+a^2} \left( -\frac{1}{a\sqrt{1+a^2}} + x \right)}{a}, & \text{if } x \geq \frac{1}{a\sqrt{1+a^2}} \text{ and } \frac{x+a|y|}{\sqrt{1+a^2}} \leq \frac{1}{a\sqrt{\lambda}}, \\ 2 - \left| \frac{1}{\sqrt{\lambda}} + \frac{-ax+|y|}{\sqrt{1+a^2}} \right| & \text{if } -\frac{1}{\sqrt{\lambda}} \leq \frac{-ax+|y|}{\sqrt{1+a^2}} \leq 0 \text{ and } \frac{1}{a\sqrt{\lambda}} \leq \frac{x+a|y|}{\sqrt{1+a^2}}, \\ 2, & \text{if } \frac{-ax+|y|}{\sqrt{1+a^2}} \leq -\frac{1}{\sqrt{\lambda}} \text{ and } x \geq \frac{\sqrt{1+a^2}}{a\sqrt{\lambda}}. \end{cases}$$

662 The graph of  $A_\lambda^\infty(f_K)$  is displayed in Figure 8(b). Note that the interpolation  $A_\lambda^\infty(f_K)$  takes the constant  
 663 value 1, which is the value given on the level set  $K_1$ , inside a triangle next to the corner of  $K_1$ , which is  
 664 then pieced continuously to  $K_2$  by a continuous piecewise affine function.

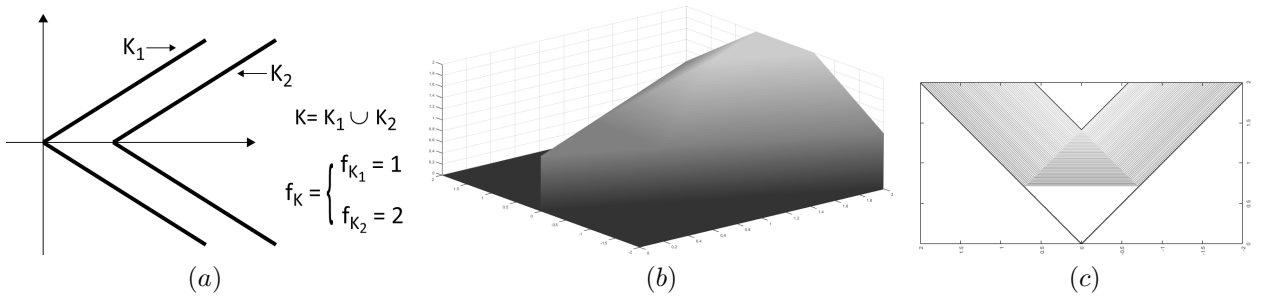


FIGURE 8. Example 6.5(ii). (a) Sample set  $K$  given by two non-smooth level sets  $K_1$  and  $K_2$  with  $a = 1$  and  $f_K(x, y) = 0$  for  $(x, y) \in K_1$  and  $f_K(x, y) = 2$  if  $(x, y) \in K_2$ . (b) Graph of  $A_\lambda^\infty(f_K)$  with  $\lambda = 1$ . (c) Isolines of  $A_\lambda^\infty(f_K)$ .

665 We conclude this section with a prototype example of level-set approximation for a function with a jump disconti-  
 666 nuity at the point  $(0, 0)$ .

667 EXAMPLE 6.6. For  $\alpha, m > 0$ , consider the sample set  $K$  given by  $K = \ell_+ \cup \ell_-$  with  $\ell_+ = \{(x, y), y = -\alpha x, x >$   
 668  $0\}$  and  $\ell_- = \{(x, y), y = \alpha x, x > 0\}$ , and define  $f_K(x, y) = m$  on  $\ell_+$  and  $f_K(x, y) = -m$  on  $\ell_-$ . The set  $K$  along  
 669 with  $f_K$  are displayed in Figure 9(a). To describe the average approximation of  $f_K$  in  $\text{co}[K] = \{(x, y), |y| \leq$   
 670  $\alpha x, x > 0\}$  which we denote by  $S_+$ , we use a parameterised description of the graph  $(x, y, A_\lambda^\infty(f_K)(x, y))$  in terms  
 671 of two new parameters. This is to avoid solving quartic equations when we find the lower and the upper transforms.  
 672 Let  $c_\lambda = 2m/\lambda$ . To calculate the lower transform  $C_\lambda^l(f_K^\infty)$  in  $S_+$  we need to find the common tangent planes for  
 673  $f_K^\infty(x, y) + \lambda(x^2 + y^2)$  of both  $\ell_+$  and  $\ell_-$ . We can write the coordinates of the convex envelope as  $(x, y, \text{co}[f_K^\infty(x, y) +$   
 674  $\lambda(x^2 + y^2)])$  by

$$675 \quad \left( \frac{(1-t_l)\sqrt{s_l^2+c_\lambda}+t_ls_l}{\sqrt{1+\alpha^2}}, \frac{-\alpha(1-t_l)\sqrt{s_l^2+c_\lambda}+\alpha t_ls_l}{\sqrt{1+\alpha^2}}, \lambda s_l^2+2\lambda(1-t_l)c_\lambda-m \right),$$

676 where  $0 \leq t_l \leq 1$  and  $s_l \geq 0$ . Similarly, the coordinates of  $(x, y, \text{co}[\lambda(x^2 + y^2) - f_K^\infty(x, y)])$  are

$$677 \quad \left( \frac{(1-t_u)s_us_u\sqrt{s_u^2+c_\lambda}}{\sqrt{1+\alpha^2}}, \frac{-\alpha(1-t_u)s_u+\alpha t_us_u\sqrt{s_u^2+c_\lambda}}{\sqrt{1+\alpha^2}}, \lambda s_u^2+2\lambda t_uc_\lambda-m \right),$$

678 where  $0 \leq t_u \leq 1$  and  $s_u \geq 0$ . However, the  $(x, y)$  coordinates in these two cases do not represent the same points.

679 Therefore we need to set them equal so that

$$680 \quad (6.1) \quad t_l = \frac{\sqrt{s_u^2 + c_\lambda} \left( \sqrt{s_l^2 + c_\lambda} - s_u \right)}{\sqrt{s_u^2 + c_\lambda} \sqrt{s_l^2 + c_\lambda} - s_u s_l}, \quad t_u = \frac{s_l \left( \sqrt{s_l^2 + c_\lambda} - s_u \right)}{\sqrt{s_u^2 + c_\lambda} \sqrt{s_l^2 + c_\lambda} - s_u s_l}.$$

681 As  $0 \leq t_l, t_u \leq 1$ , we see that  $|s_u^2 - s_l^2| \leq c_\lambda$ . Thus if we let

$$682 \quad x(s_l, s_u) = \frac{(1 - t_l) \sqrt{s_l^2 + c_\lambda} + t_l s_l}{\sqrt{1 + \alpha^2}}, \quad y(s_l, s_u) = \frac{-\alpha(1 - t_l) \sqrt{s_l^2 + c_\lambda} + \alpha t_l s_l}{\sqrt{1 + \alpha^2}},$$

683 and

$$684 \quad A_\lambda^\infty(f_K)(s_l, s_u) = \frac{1}{2} \left( \lambda(s_l^2 - s_u^2) + 2\lambda c_\lambda((1 - t_l - t_u)) \right),$$

685 the graph of the average approximation of  $f_K$  in the sector  $S_+$  defined above is

$$686 \quad \Gamma_{S_+, \lambda} = \left\{ (x(s_l, s_u), y(s_l, s_u), A_\lambda^\infty(f_K)(s_l, s_u)), s_u \geq 0, s_l \geq 0, |s_u^2 - s_l^2| \leq c_\lambda \right\},$$

687 where  $t_l$  and  $t_u$  are given by (6.1).

688 Although it is not easy to write the graph in the standard Euclidean system, observe that the graph is smooth in the  
 689 interior region  $\{(s_l, s_u), s_l > 0, s_u > 0, |s_l^2 - s_u^2| < c_\lambda\}$ . By our construction, we also note that the surface  $\Gamma_{S_+, \lambda}$   
 690 is formed by the average of two families of parameterised line segments. Also when  $\lambda > 0$  is large, outside a small  
 691 sector, say,  $S_+^\lambda = \{|y| \leq \alpha, 0 < x < 2\sqrt{2m/\lambda}\}$ , our formula is an interpolation in  $S_+ \setminus S_+^\lambda$ . Figure 9(b) shows a  
 692 portion of the graph of  $A_\lambda^\infty(f_K)$ .

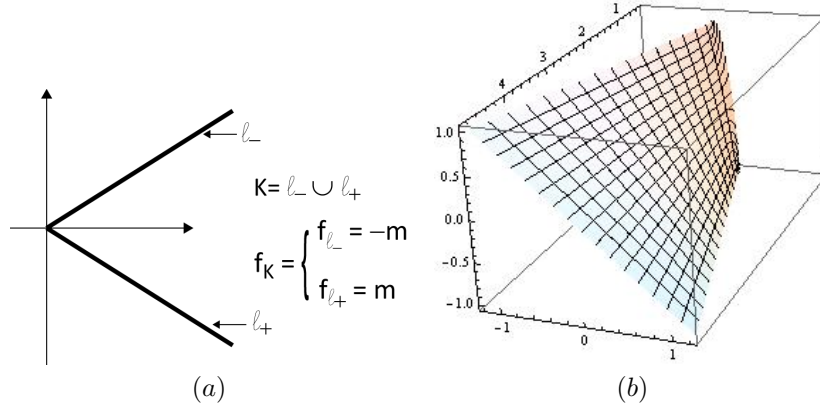


FIGURE 9. Example 6.6. (a) Sampled set  $K$  with the definition of  $f_K$  that presents a discontinuity jump at  $(0,0)$ . (b) Graph of  $A_\lambda^\infty(f_K)$  with  $\alpha = 0.25$ ,  $m = 1$  and  $\lambda = 5$ .

693 **7. Numerical Examples.** For more complicated sets  $K$  and functions  $f_K$ , the average approximation op-  
 694 erators  $A_\lambda^M(f_K)$  and  $A_\lambda^\infty(f_K)$  must be evaluated numerically. Figure 10 sketches the steps needed for their im-  
 695 plementation. It is noted that the numerical realization relies mainly on the availability of numerical schemes for  
 696 computing the upper and lower transform of a given function, which in turn means the availability of schemes to  
 697 compute the convex envelope of a function. Because of the locality property of the compensated convex transforms  
 698 (see for instance Theorem 3.10 in [57], where quantitative estimates of the neighbourhood size are also given),  
 699 it is possible to develop fast schemes that depend only on the local behaviour of the input function. This is in

700 sharp contrast to the evaluation of the convex envelope of a function which is a global evaluation. In the current  
 701 context, we consider a generalization of the scheme introduced in [37] which is briefly summarized in Algorithm 1  
 702 and described below. Given a uniform grid of points  $x_k \in \mathbb{R}^n$ , equally spaced with grid size  $h$ , let us denote by  $S_{x_k}$   
 703 the  $d$ -point stencil of  $\mathbb{R}^n$  with center at  $x_k$  defined as  $S_{x_k} = \{x_k + hr, |r|_\infty \leq 1, r \in \mathbb{Z}^n\}$  with  $|\cdot|_\infty$  the  $\ell^\infty$ -norm  
 704 of  $r \in \mathbb{Z}^n$  and  $d = \#(S)$ . At each grid point  $x_k$  we compute the convex envelope of  $f$  at  $x_k$  by an iterative scheme  
 705 where each iteration step  $m$  is given by

$$706 \quad (\text{co } f)_m(x_k) = \min \left\{ f(x_k), \sum \lambda_i (\text{co } f)_{m-1}(x_i), \sum \lambda_i = 1, \lambda_i \geq 0, x_i \in S_{x_k} \right\}$$

707 with the minimum taken between  $f(x_k)$  and only some convex combinations at the stencil grid points. For the  
 708 full algorithmic and implementation details of the scheme, the convex combinations that one needs to take, and its  
 709 convergence analysis we refer to [53].

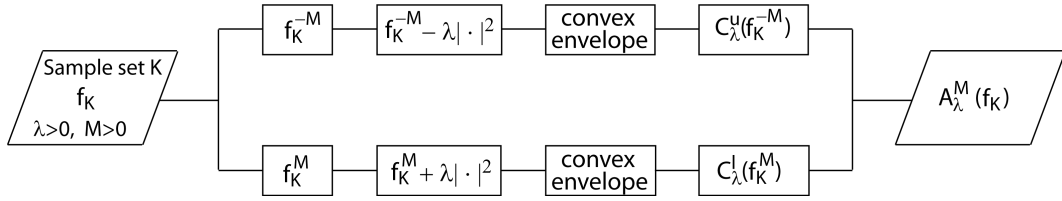


FIGURE 10. Flow chart for the numerical evaluation of  $A_\lambda^M(f_K)$ .

---

**Algorithm 1** Conceptual implementation of the scheme that computes the convex envelope of  $f$ .

---

- 1: Set  $m = 1$ ,  $(\text{co } f)_0 = f$ ,  $tol$
  - 2:  $\epsilon = \|f\|_{L^2}$
  - 3: **while**  $\epsilon > tol$  **do**
  - 4:  $\forall x_k, (\text{co } f)_m(x_k) = \min \left\{ f(x_k), \sum \lambda_i (\text{co } f)_{m-1}(x_i), \sum \lambda_i = 1, \lambda_i \geq 0, x_i \in S_{x_k} \right\}$
  - 5:  $\epsilon = \|(\text{co } f)_m - (\text{co } f)_{m-1}\|_{L^2}$
  - 6:  $m \leftarrow m + 1$
  - 7: **end while**
- 

710 In this section, we present some illustrative numerical experiments of the applications described above, namely,  
 711 for surface reconstruction from contour lines, point clouds and image inpainting. For the first two applications, we  
 712 discuss examples of approximation of a smooth function, of a continuous but non-differentiable function and of a  
 713 discontinuous function. The quality of the approximation is measured by computing the relative  $L^2$ -error

$$714 \quad (7.1) \quad \epsilon = \frac{\|f - A_\lambda^M(f_K)\|_{L^2(\Omega)}}{\|f\|_{L^2(\Omega)}},$$

715 where  $f$  is the original function that we want to approximate and  $A_\lambda^M(f_K)$  is the average approximation of the  
 716 sample  $f_K$  of  $f$  over  $K$ . We mainly postpone a thorough comparison with other state-of-art methods to forthcoming  
 717 papers, just giving some first comparisons with the AMLE method presented in [2, 13] and applied to surface  
 718 reconstruction and image inpainting. Image denoising for salt & pepper noise and image inpainting were solved by  
 719 the TV-model described in [14] and in [29], respectively.

720 We conclude this short introduction by stating that at least for the examples and methods we have considered  
 721 here, we have observed higher accuracy of the  $A_\lambda^M(f_K)$  interpolant and the faster execution time for its numerical  
 722 evaluation compared to the other methods.

723 **7.1. Surface reconstruction from contour lines.** We describe next some numerical experiments on surface  
 724 reconstruction from sectional contours. This is the problem of reconstructing the graph of a function  $f$  by knowing  
 725 only some contour lines of  $f$ , and has applications in medical imaging, computer graphics, reverse engineering and  
 726 terrain modelling, among others. The underlying function  $f : \mathbb{R}^2 \supset \Omega \rightarrow \mathbb{R}$  is assumed to have various regularity  
 727 properties. Consider first the reconstruction of an infinitely differentiable function given by the Franke test function  
 728 [25], and then the reconstruction of functions with less regularity. In addition to the relative  $L^2$ -error  $\epsilon$  defined by  
 729 (7.1), which gives a measure of how close  $A_\lambda^M(f_K)$  is to  $f$ , we also compute

$$730 \quad (7.2) \quad \epsilon_K = \frac{\|f_K - A_\lambda^M(f_K)_K\|_{L^2(K)}}{\|f_K\|_{L^2(K)}},$$

731 where  $f_K$  is the sample function and  $A_\lambda^M(f_K)_K$  the restriction of  $A_\lambda^M(f_K)$  to  $K$ , to assess the quality of  $A_\lambda^M(f_K)$   
 732 as an interpolant of  $f_K$ . We will thus verify that in the examples where  $f$  is continuous, the average approximation  
 733  $A_\lambda^M(f_K)$  represents an interpolation of  $f_K$ , consistently with the theoretical results established in Section 3.

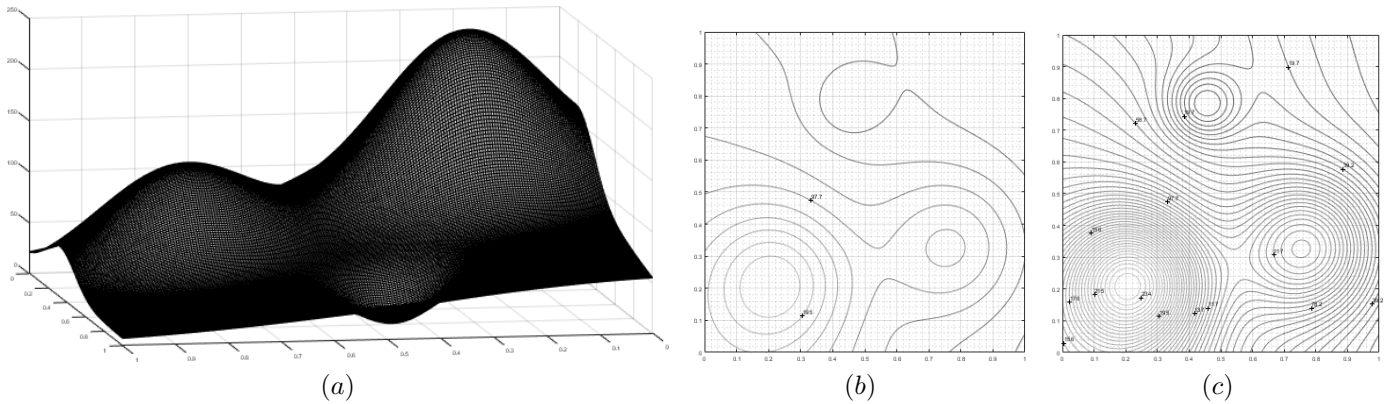


FIGURE 11. Example 7.1.1. (a) Graph of the Franke test function  $f$  defined by Equation (7.3). (b) Sample set  $K$  of 10-contour lines of  $f$  at equally spaced heights equal to  $(\max(f) - \min(f))/10$ , defining the sample function  $f_K$ . (c) Sample set  $K$  of 50-contour lines of  $f$  at equally spaced heights equal to  $(\max(f) - \min(f))/50$ , defining the sample function  $f_K$ .

734 **7.1.1. Franke test function.** The Franke function was introduced in [25] as one of the test functions for  
 735 the evaluation of methods for scattered data interpolation [26]. The function consists of two Gaussian peaks and  
 736 a sharper Gaussian dip superimposed on a surface sloping toward the first quadrant [25] and is defined by

$$737 \quad (7.3) \quad f(x, y) = \frac{3}{4}e^{-((9x-2)^2+(9y-2)^2)/4} + \frac{3}{4}e^{-((9x+1)^2/49+(9y+1)^2/10)} + \frac{1}{2}e^{-((9x-7)^2/4-(9y-3)^2)/4} \\ - \frac{1}{5}e^{-((9x-4)^2+(9y-7)^2)}.$$

738 Consider  $f$  defined in the unit square  $\Omega = ]0, 1]^2$ . Its graph is displayed in Figure 11(a). Approximations using  
 739 two different sets of contour lines have been computed by applying the methods described in this paper and by  
 740 the AMLE model introduced in [13] and applied in [2] to the interpolation of digital elevation models. The two  
 741 sets of contour lines consist of 10 and 50 equally spaced level lines, respectively. Given the smoothness of  $f$ , the  
 742 isolines are also smooth curves. The two sample sets are displayed in Figure 11(b) and Figure 11(c), respectively,  
 743 whereas the graph of the corresponding average approximations  $A_\lambda^M(f_K)$  are shown in Figure 12(a) and Figure  
 744 12(c). Figure 12(b) and Figure 12(d) display, on the other hand, the corresponding contour lines which, compared  
 745 to the same equally spaced level lines of  $f$  displayed in Figure 11(c) show a good quality of the reconstruction given  
 746 by  $A_\lambda^M(f_K)$ . This is also confirmed by the values of the relative  $L^2$ -error  $\epsilon$  equal to 0.01986 and 0.00218 for the

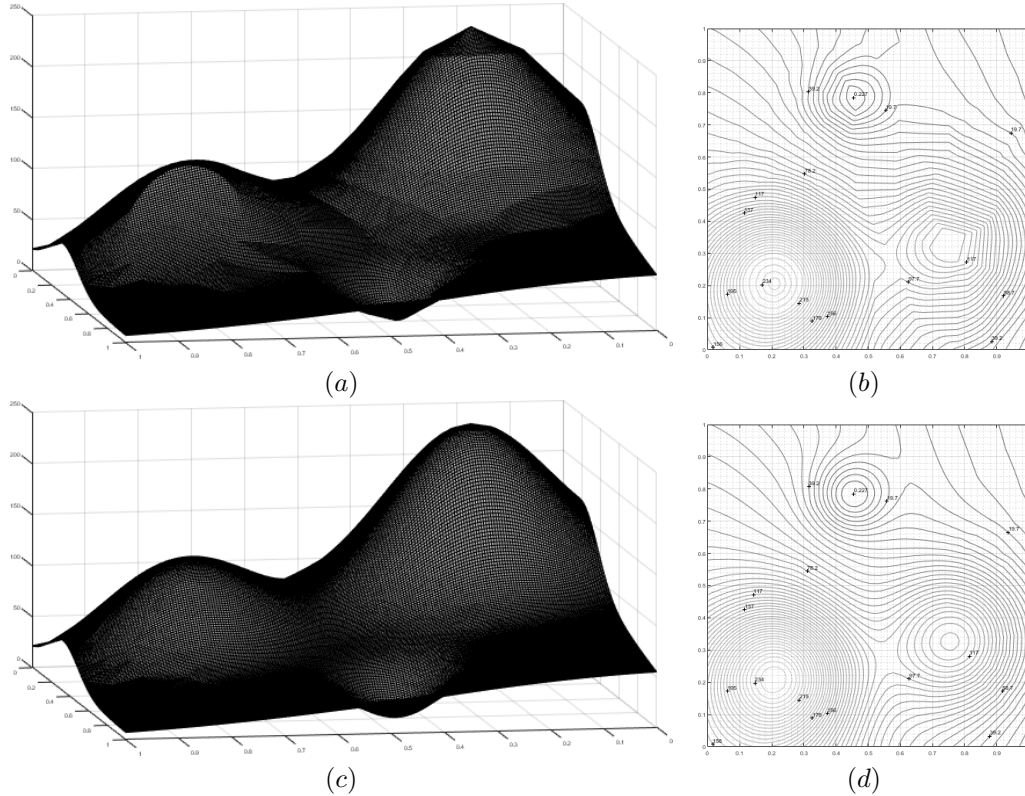


FIGURE 12. Example 7.1.1. (a) Graph of the interpolation function  $A_\lambda^M(f_K)$  computed for  $\lambda = 1 \cdot 10^4$ ,  $M = 1 \cdot 10^5$ , and corresponding to the set  $K$  of 10-contour lines of  $f$  displayed in Figure 11(b). Relative  $L^2$ -Errors:  $\epsilon = 0.01986$ ,  $\epsilon_K = 3.33 \cdot 10^{-15}$ . (b) Isolines of  $A_\lambda^M(f_K)$  at equally spaced heights equal to  $(\max(f) - \min(f))/50$ . (c) Graph of the interpolation function  $A_\lambda^M(f_K)$  computed for  $\lambda = 1 \cdot 10^4$ ,  $M = 1 \cdot 10^5$ , and corresponding to the set  $K$  of 50-contour lines of  $f$  displayed in Figure 11(d). Relative  $L^2$ -Errors:  $\epsilon = 0.0021$ ,  $\epsilon_K = 2.62 \cdot 10^{-15}$ . (d) Isolines of  $A_\lambda^M(f_K)$  at equally spaced heights equal to  $(\max(f) - \min(f))/50$ .

747 two sample sets  $K$  of contour lines, respectively. Note the clear reduction of error by increasing the density of the  
 748 data set. For the two average approximations, the value of  $\epsilon_K$  is of the order of  $10^{-15}$ , confirming that the average  
 749 approximation  $A_\lambda^M(f_K)$  interpolates exactly  $f_K$ .

750 Figure 13 displays the reconstruction obtained by the AMLE method. The numerical results were obtained  
 751 by using the MatLab code described in [39]. In this case, for a number of iterations equal to  $10^6$ , we found a  
 752 relative  $L^2$ -error higher than the one generated by  $A_\lambda^M(f_K)$  with  $\epsilon$  equal to 0.0338 and 0.0101 for the two sample  
 753 set  $K$  of 10 and 50 level lines, respectively. Consistently with the findings of [35], also here we find that the AMLE  
 754 interpolation generates additional kinks which are not present in  $f$  and might be the cause for the reduced quality  
 755 of the approximation compared to  $A_\lambda^M(f_K)$ .

756 **7.1.2. Continuous piecewise affine function.** We describe now the approximation of the continuous piece-  
 757 wise affine function  $f$  associated with the triangulation shown in Figure 14(a) where also the node values of  $f$  are  
 758 given while Figure 14(b) displays the graph of  $f$ . Two different sample sets of contour lines have been considered.  
 759 One consists of 6 isolines whereas the other one is formed by 15 isolines. The isolines are not equally spaced  
 760 and are displayed in Figure 14(c) and Figure 14(d), respectively, whereas the graphs of the corresponding average  
 761 approximations  $A_\lambda^M(f_K)$  are shown in Figure 15(a) and Figure 15(c) along with the isolines corresponding to 50  
 762 equally spaced isolevels. In this example the isolines are not smooth curves so that locally, around their singulari-  
 763 ties, for the interpretation of the results, it can be useful to recall and compare with the behaviour of the average  
 764 approximation described in the Prototype Example 6.5(ii) in Section 6. The average approximation displays a step

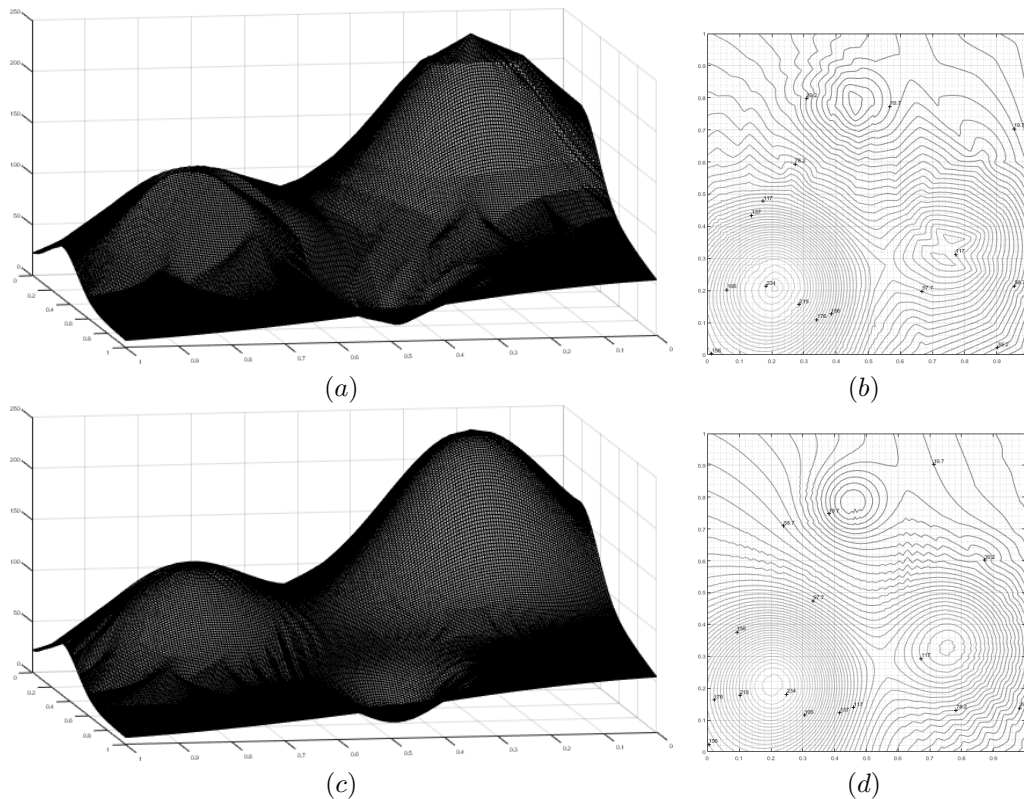


FIGURE 13. *Example 7.1.1.* (a) Graph of the AMLE interpolation function of  $f_K$  with  $K$  the set of 10-contour lines of  $f$  displayed in Figure 11(b). Relative  $L^2$ -Error  $\epsilon = 0.0338$ . (b) Isolines of the AMLE interpolation function of  $f_K$  at equally spaced heights equal to  $(\max(f) - \min(f))/50$ . (c) Graph of the AMLE interpolation function of  $f_K$  with  $K$  the set of 50-contour lines of  $f$  displayed in Figure 11(d). Relative  $L^2$ -Error  $\epsilon = 0.0101$ . (d) Isolines of the AMLE interpolation function of  $f_K$  at equally spaced heights equal to  $(\max(f) - \min(f))/50$

765 which reduces by increasing the number of isolines. Note that these steps are also visible in the Matlab display  
 766 of the graph of the function  $f$ , thus they are errors of the interpolation scheme that is used. We find that for  
 767 the reconstruction of the function sampled on the 6-contour line set, the relative  $L^2$ -error  $\epsilon$  is equal to 0.019302.  
 768 This value reduces to 0.004805 for the reconstruction of the function sampled on the 15-contour line set  $K$ . For  
 769 both these two examples, it is confirmed that the average approximation  $A_\lambda^M(f_K)$  interpolates  $f_K$  given that the  
 770 computed value of  $\epsilon_K$  is of the order of  $10^{-16}$ .

771 The AMLE method appears yielding slightly better results for the reconstruction from the sample set  $K$  of 6  
 772 contour lines. In this case, we find a relative  $L^2$ -error  $\epsilon$  equal to 0.01675, slightly lower than the one produced by  
 773  $A_\lambda^M(f_K)$ . Figure 16(a) displays the graph of the AMLE interpolant which does not contain steps along the edges  
 774 of the pyramid, whereas Figure 16(b) shows its isolines for 50 levels of equally spaced heights. For the AMLE  
 775 interpolant of the sample set  $K$  of 15 contour lines, whose graph is displayed in Figure 16(c) and the isolines in  
 776 Figure 16(d), the relative  $L^2$ -error  $\epsilon$  is equal to 0.00713, which is slightly higher than the one produced by  $A_\lambda^M(f_K)$   
 777 for the same sample set  $K$ . Note also here the appearance of additional kinks in the graph of the AMLE interpolant  
 778 which might reduce the global quality of the AMLE approximation compared to  $A_\lambda^M(f_K)$ .

779 **7.1.3. Discontinuous piecewise affine function.** The approximation of discontinuous functions has not  
 780 been covered by the theoretical developments of Section 3, where we assumed  $f$  to be continuous. Now we present  
 781 a test case where we examine how our average approximation performs numerically and verify that also in this

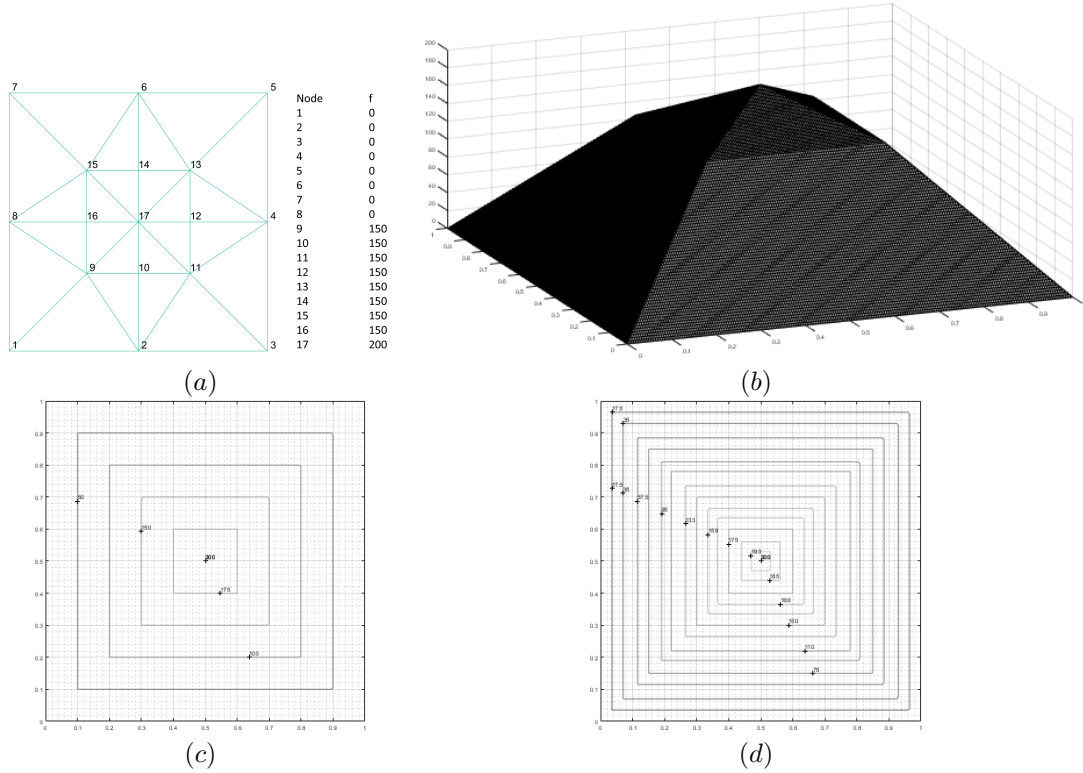


FIGURE 14. *Example 7.1.2.* (a) Triangulation with nodal values used to construct a continuous piecewise affine function. (b) Graph of  $f$  associated with the triangulation defined in (a). (c) Sample set  $K$  of 6-contour line of  $f$ , defining the sample function  $f_K$ . (d) Sample set  $K$  of 15-contour line of  $f$ , defining the sample function  $f_K$ .

782 case  $A_\lambda^M(f_K)$  represents a continuous interpolation of  $f_K$ . We consider the following discontinuous piecewise affine  
 783 function

$$784 \quad f : (x, y) \in ]0, 1[^2 \rightarrow 200, \quad f(x, y) = \begin{cases} x + y - 1, & \text{if } 1/2 \leq x \leq 1, \quad 1/2 \leq y \leq 1 \\ x - y - 1/2 & \text{if } 1/2 \leq x \leq 1, \quad 0 \leq y < 1/2 \\ -x + y - 1/2 & \text{if } 0 \leq x < 1/2, \quad 1/2 \leq y \leq 1 \\ -x - y & \text{if } 0 \leq x < 1/2, \quad 0 \leq y < 1/2 \end{cases}$$

785 whose graph is displayed in Figure 17(b) while Figure 17(a) shows the equation of  $f$  in each of its affine parts.

786 We compare the reconstruction of  $f$  for two sample sets  $K$ , one formed by 20 equally spaced isolines and  
 787 the other by 100 equally spaced isolines. Such sets are displayed in Figure 17(c) and Figure 17(d), respectively.  
 788 Notably, for both sample sets  $K$ ,  $A_\lambda^M(f_K)$  coincides exactly with the original function  $f$ . We find, indeed, for  
 789 both sample sets  $K$ ,  $\epsilon$  and  $\epsilon_K$  the order  $10^{-15}$  by taking  $\lambda = 10^7$ ,  $M = 10^6$ . This occurs because of an exact  
 790 sampling of the discontinuity jump, thus we are able to reproduce exactly the affine parts of  $f$ , consistently with  
 791 the theoretical findings of Section 3. Furthermore, given the high value of  $\lambda$  and recalling the behaviour of the  
 792 jump in the Prototype Example 5.3, we are able to describe the sharp discontinuity.

793 For the case where we do not have an exact sampling of the discontinuity jump, we refer to Example 7.2.3  
 794 concerning the surface reconstruction from point clouds with sampling points not necessarily on the discontinuity.

795 A different behaviour is displayed by the AMLE interpolation. Consistently with the observations in [35], the

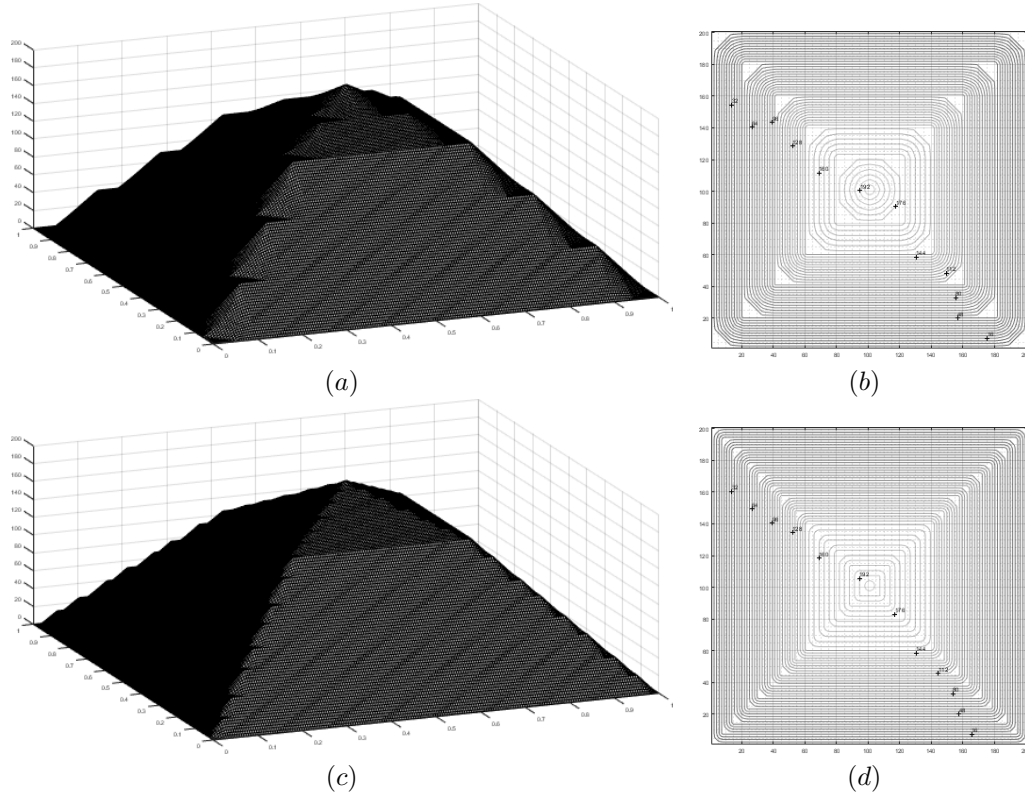


FIGURE 15. *Example 7.1.2.* (a) Graph of the interpolation function  $A_\lambda^M(f_K)$  with  $K$  given in Figure 14(c), and  $\lambda = 1 \cdot 10^5$ ,  $M = 1 \cdot 10^5$ ,  $tol = 10^{-9}$ . Relative  $L^2$ -Errors:  $\epsilon = 0.019302$ ,  $\epsilon_K = 4.50 \cdot 10^{-16}$ . (b) Isolines of  $A_\lambda^M(f_K)$  at equally spaced heights equal to  $(\max(f) - \min(f))/50$ . (c) Graph of the interpolation function  $A_\lambda^M(f_K)$  with  $K$  given in Figure 14(d), and  $\lambda = 1 \cdot 10^5$ ,  $M = 1 \cdot 10^5$ ,  $tol = 10^{-9}$ . Relative  $L^2$ -Errors:  $\epsilon = 0.004805$ ,  $\epsilon_K = 8.68 \cdot 10^{-16}$ . (d) Isolines of  $A_\lambda^M(f_K)$  at equally spaced heights equal to  $(\max(f) - \min(f))/50$ .

796 level lines of the AMLE interpolant are smooth [44], thus discontinuities cannot be recovered. A better visual  
 797 appreciation of this fact is obtained by looking at the graphs of the AMLE interpolant shown in Figure 18(a) and  
 798 Figure 18(c) for the two sample sets  $K$ , and at their isolines displayed in Figure 18(b) and Figure 18(d), respectively.  
 799 The isolines at the two sides of the jump should ‘end’ in the discontinuity but they are somehow enforced to join  
 800 each other by the continuous isolines of the AMLE interpolant. In this case we find values of the relative  $L^2$ -error  
 801  $\epsilon$ , with  $\epsilon = 0.1071$  and  $\epsilon = 0.06738$  for the two sample sets, respectively.

802 Table 1 summarizes the relative  $L^2$ -errors of  $A_\lambda^M(f_K)$  and the AMLE interpolant for the examples considered  
 803 in this section.

804 **7.2. Scattered data approximation.** We turn now to some numerical experiments on scattered data ap-  
 805 proximation. In particular, in the terminology of [36], we consider the problem of function reconstruction from  
 806 point clouds, where the sample points that form the set  $K$  do not meet any particular condition as to spacing or  
 807 density. As in the previous section, the set of test problems consists of three test functions with different regularity:  
 808 an infinitely differentiable function given by the Franke test function, a continuous piecewise affine function and a  
 809 discontinuous piecewise affine function. The three test functions are all to be approximated in  $\Omega = ]0, 1[^2$ . In the  
 810 numerical implementation of the method, the domain  $\Omega$  is discretized with a grid of  $201 \times 201$  points and the two  
 811 sample sets  $K$  are obtained by sampling the grid points using a random number generator with different levels of  
 812 density. The two sample sets  $K$ , corresponding to a coarse and a dense sampling, are displayed in Figure 19(a)  
 813 and Figure 19(b), respectively. The reason for taking such a regular discretization of  $\Omega$  is because the numerical

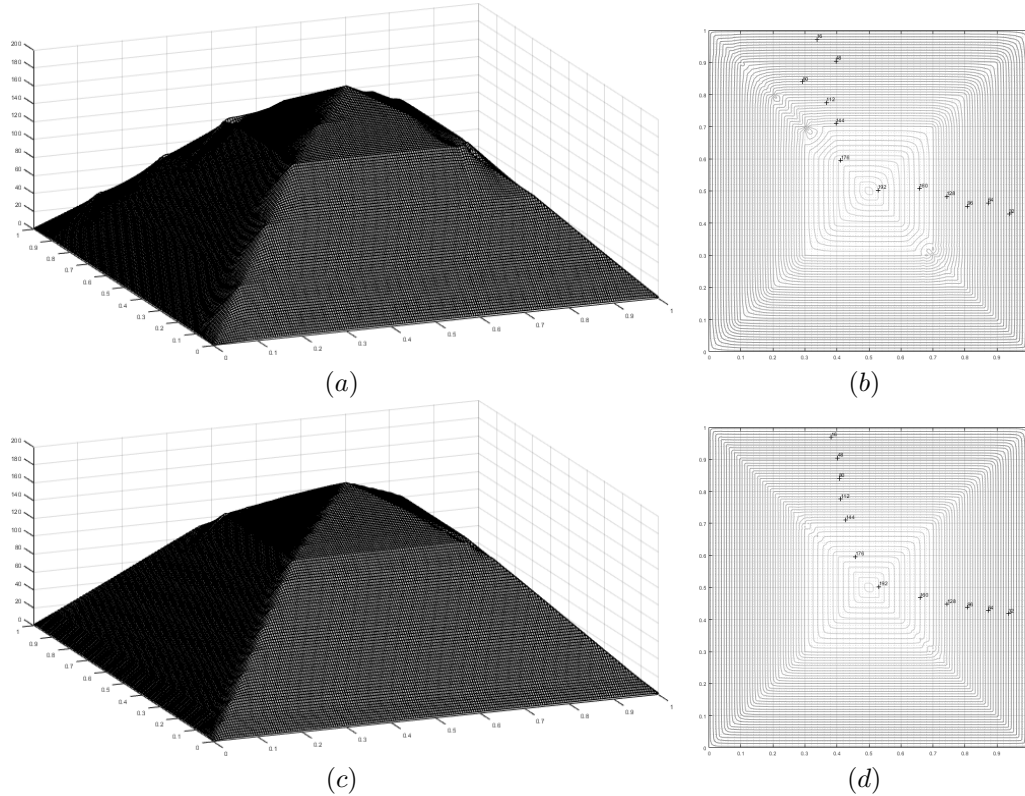


FIGURE 16. Example 7.1.2. (a) Graph of the AMLE interpolation function of  $f_K$  with  $K$  the set of 6-contour lines of  $f$  displayed in Figure 14(c). Relative  $L^2$ -Error  $\epsilon = 0.01675$ . (b) Isolines of the AMLE interpolant at equally spaced heights equal to  $(\max(f) - \min(f))/50$ . (c) Graph of the AMLE interpolation function of  $f_K$  with  $K$  the set of 15-contour lines of  $f$  displayed in Figure 14(d). Relative  $L^2$ -Error  $\epsilon = 0.0071297$ . (d) Isolines of the AMLE interpolant at equally spaced heights equal to  $(\max(f) - \min(f))/50$ .

$f$	$K$	$\epsilon$	
		$A_\lambda^M(f_K)$	AMLE
F	10 level lines	0.0199	0.0338
	50 level lines	0.0021	0.0101
CPA	6 level lines	0.0193	0.0167
	15 level lines	0.0048	0.0071
DPA	20 level lines	$8.7 \cdot 10^{-15}$	0.1071
	100 level lines	$1.5 \cdot 10^{-16}$	0.0674

TABLE 1

Summary of the accuracy of the compensated convexity based interpolant  $A_\lambda^M(f_K)$  and of the AMLE interpolant for the Examples considered in Section 7.1. Legend:  $K$  Sample set.  $\epsilon$  Relative  $L^2$ -error.  $\epsilon_K$  Relative  $L^2$ -error on the sample set  $K$ .  $F$  Franke test function (Example 7.1.1).  $CPA$  Continuous piecewise affine function (Example 7.1.2).  $DPA$  Discontinuous piecewise affine function (Example 7.1.3).

814 scheme we use to compute the convex envelope (see Algorithm 1), is particularly suitable for applications to image  
 815 processing where such discrete geometry is related to the image resolution.

816 For the measure of the global quality of the approximation  $A_\lambda^M(f_K)$  we compute the relative  $L^2$ -error  $\epsilon$  defined  
 817 by Eq. (7.1) whereas we will use the relative  $L^2$ -error  $\epsilon_K$  defined by

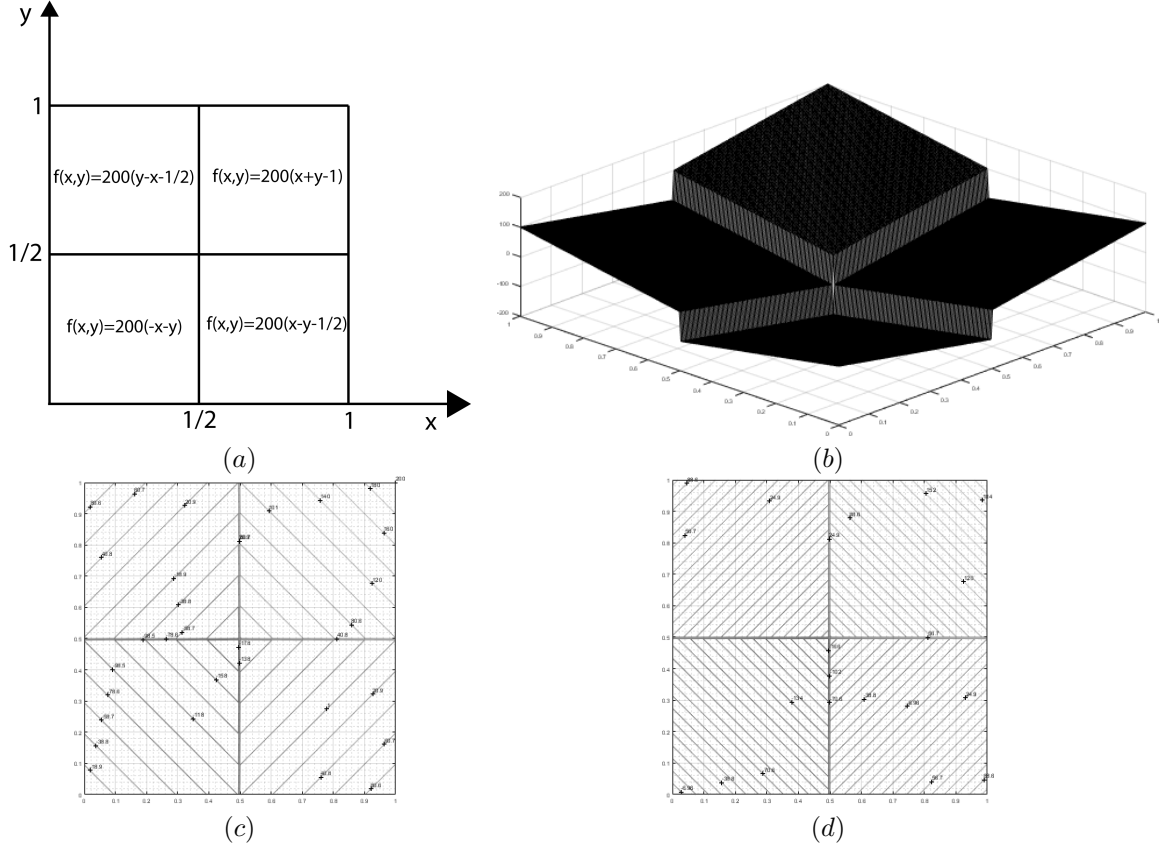


FIGURE 17. *Example 7.1.3.* (a) Equations of each affine part of  $f$ . (b) Graph of  $f$ . (c) Sample set  $K$  of 20-contour line of  $f$  at equally spaced heights equal to  $(\max(f) - \min(f))/20$ , defining the sample function  $f_K$ . (d) Sample set  $K$  of 50-contour lines of  $f$  at equally spaced heights equal to  $(\max(f) - \min(f))/50$ , defining the sample function  $f_K$ ;

$$818 \quad (7.4) \quad \epsilon_K = \frac{\sqrt{\sum_{k \in K} |f(x_k) - A_\lambda^M(f_K)(x_k)|^2}}{\sqrt{\sum_{k \in K} |f(x_k)|^2}}$$

819 to assess the quality of  $A_\lambda^M(f_K)$  as interpolant of  $f_K$ . In this case too, we will find that the average approximation  
 820  $A_\lambda^M(f_K)$  is an interpolation of  $f_K$ , consistently with the theoretical findings of Section 4. We then conclude this  
 821 section by giving an example of digital elevation model reconstruction starting from real data, and another of salt  
 822 & pepper noise removal as an application of scattered data approximation to image processing.

823 **7.2.1. Franke test function.** In this example, the Franke test function  $f$  defined by Eq. (7.3) is sampled  
 824 over the two sets  $K$  of scattered points displayed in Figure 19(a) and Figure 19(b), respectively. For the resulting  
 825 sample functions  $f_K$  we compute the corresponding average approximations  $A_\lambda^M(f_K)$  whose graphs are displayed  
 826 in Figure 20, along with the respective isolines. Specifically, the comparison of the isolines of  $A_\lambda^M(f_K)$  displayed  
 827 in Figure 20(b) and in Figure 20(d) for the coarse and dense sample sets  $K$ , respectively, with the isolines of the  
 828 Franke function  $f$  displayed in Figure 11(d), allows a visual appreciation of the quality of the reconstruction. This

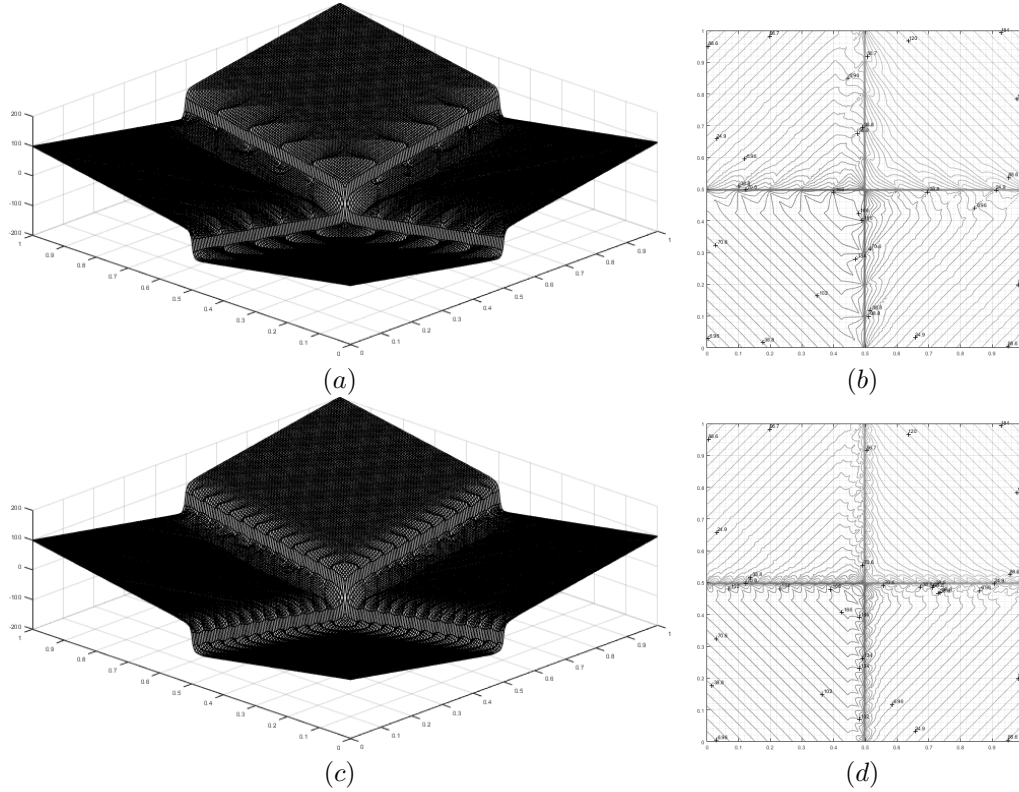


FIGURE 18. *Example 7.1.3.* (a) Graph of the AMLE interpolation function of  $f_K$  with  $K$  the set of 20-contour lines of  $f$  displayed in Figure 17(c). Relative  $L^2$ -Error  $\epsilon = 0.1071$ . (b) Isolines of the AMLE interpolant at equally spaced heights equal to  $(\max(f) - \min(f))/50$ . (c) Graph of the AMLE interpolation function of  $f_K$  with  $K$  the set of 50-contour lines of  $f$  displayed in Figure 17(d). Relative  $L^2$ -Error  $\epsilon = 0.06738$ . (d) Isolines of the AMLE interpolant at equally spaced heights equal to  $(\max(f) - \min(f))/50$ .

829 is also confirmed by the computed values of the relative  $L^2$ -error  $\epsilon$ . For the coarse sample set we get  $\epsilon = 0.0206$   
 830 whereas, for the denser sample set,  $\epsilon = 0.00157$ . Finally, also in this case, we verify that  $A_\lambda^M(f_K)$  is an interpolant  
 831 of  $f_K$  given that for both approximations the relative  $L^2$ -error  $\epsilon_K$  defined by Eq. (7.4) is of the order of  $10^{-15}$ .

832 The AMLE method as introduced in [13] can be applied also in this case for the interpolation of isolated points.  
 833 In fact, this is one of its particular feature out of the pde based interpolators. The graphs of the AMLE interpolants  
 834 for the two sample sets are displayed in Figure 21, which contains also the plot of the corresponding isolines for 50  
 835 level lines of equally spaced heights. The plot of these isolines, once compared with the same isolines of  $f$  displayed  
 836 in Figure 11(c), allows a visual assessment of the quality of the reconstruction. As in the Example 7.1.1 concerning  
 837 with the reconstruction from contour lines, we note also here the introduction of artificial artefacts in the form of  
 838 krinks in the graph of the interpolant, which, in contrast, are not present in the graph of  $A_\lambda^M(f_K)$ . For the coarse  
 839 and dense sampling set we find that the relative  $L^2$ -error of the AMLE interpolant amounts to  $\epsilon = 0.05764$  and  
 840  $\epsilon = 0.010902$ , respectively, which are slightly higher than the values produced by  $A_\lambda^M(f_K)$ .

841 **7.2.2. Continuous piecewise affine function.** The continuous piecewise affine function  $f$  introduced in  
 842 Section 7.1.2 is evaluated here over the two sample sets  $K$  of Figure 19(a) and Figure 19(b), defining two test cases  
 843 of sample function  $f_K$ . The graph of the corresponding average approximation  $A_\lambda^M(f_K)$  is displayed in Figure 22  
 844 along with the respective isolines whereas Figure 23 shows those of the AMLE interpolating along with its isolines  
 845 of equally spaced heights. The drawing of the isolines allows a visual assessment of the quality of the reconstruction  
 846 if these are compared to the isolines of the original function  $f$  displayed in Figure 15(c). A first observation about  
 847 the graphs of  $A_\lambda^M(f_K)$  is the nearly absence of the steps along the edges of the pyramid due to the constraint

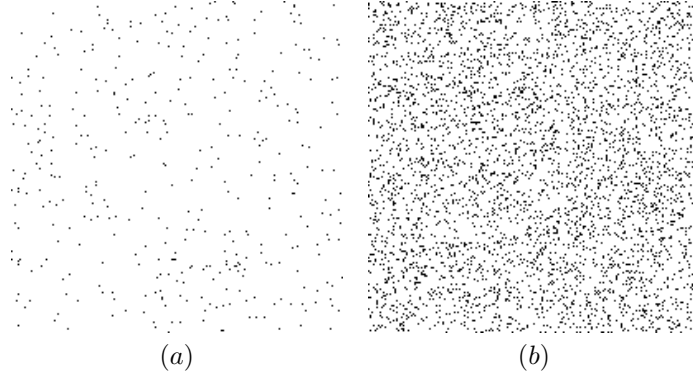


FIGURE 19. Set  $K$  of sample points of a grid of  $201 \times 201$  points in  $]0, 1[^2$  for two levels of sampling density: (a) Coarse sampling with 400 grid points out of 40401. (b) Dense sampling with 4061 grid points out of 40401.

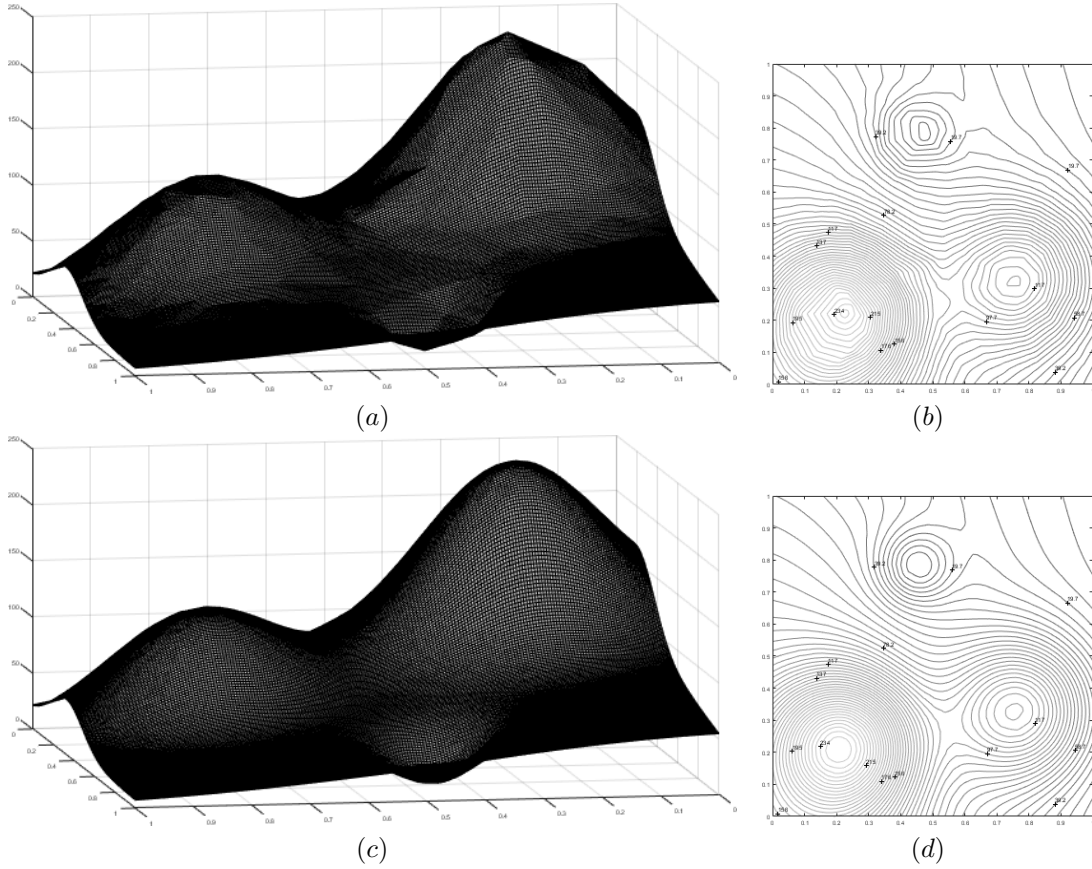


FIGURE 20. Example 7.2.1. (a) Graph of  $A_\lambda^M(f_K)$  for  $\lambda = 1 \cdot 10^4$ ,  $M = 1 \cdot 10^5$  and the set  $K$  of Figure 19(a). Relative  $L^2$ -Errors:  $\epsilon = 0.020252$ ,  $\epsilon_K = 5.31 \cdot 10^{-15}$ . (b) Isolines of  $A_\lambda^M(f_K)$  at equally spaced heights equal to  $(\max(f) - \min(f))/50$ . (c) Graph of  $A_\lambda^M(f_K)$  for  $\lambda = 5 \cdot 10^3$ ,  $M = 1 \cdot 10^5$  and the set  $K$  of Figure 19(b) Relative  $L^2$ -Errors:  $\epsilon = 0.0015548$ ,  $\epsilon_K = 4.13 \cdot 10^{-15}$ . (d) Isolines of  $A_\lambda^M(f_K)$  at equally spaced heights equal to  $(\max(f) - \min(f))/50$ .

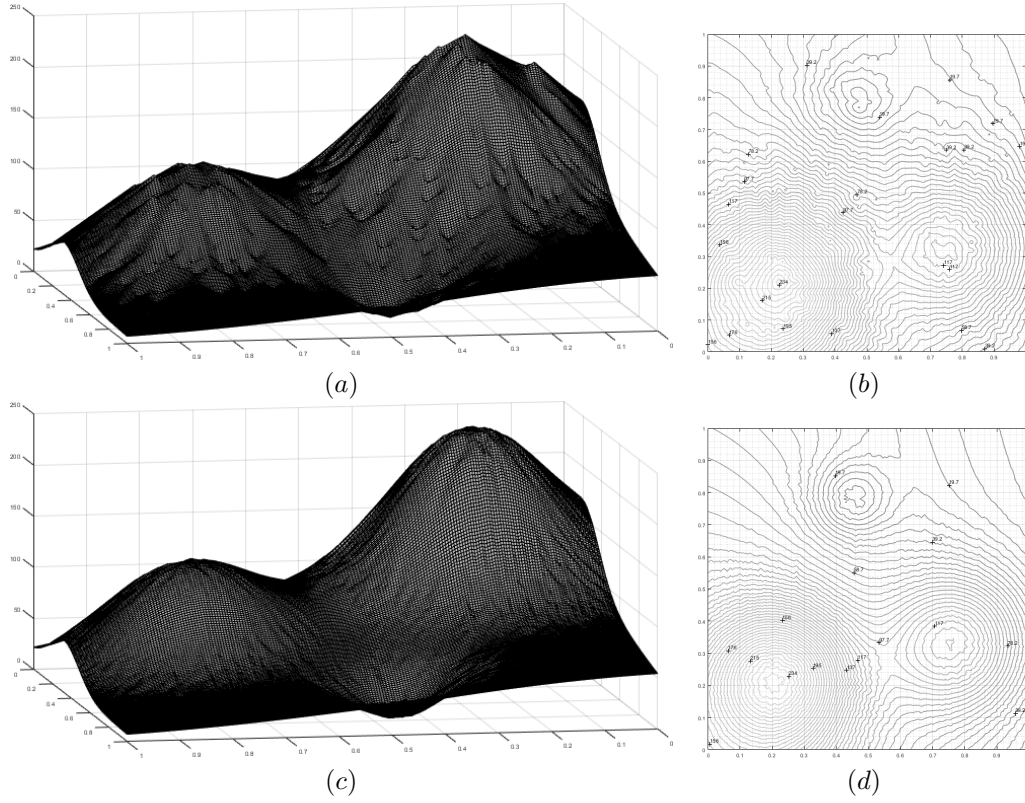


FIGURE 21. *Example 7.2.1.* (a) Graph of the AMLE interpolation function of  $f_K$  with  $K$  the set of scattered points displayed in Figure 19(a). Relative  $L^2$ -Error:  $\epsilon = 0.05764$ . (b) Isolines of the AMLE interpolant at equally spaced heights equal to  $(\max(f) - \min(f))/50$ . (c) Graph of the AMLE interpolation function of  $f_K$  with  $K$  the set of scattered points displayed in Figure 19(b). Relative  $L^2$ -Error:  $\epsilon = 0.010902$ . (d) Isolines of the AMLE interpolant at equally spaced heights equal to  $(\max(f) - \min(f))/50$ .

848 enforced by the fixed contour lines, on the contrary the graphs of the AMLE interpolant present, even for this  
 849 example, artefacts in the form of artificial krinks and valleys. The relative  $L^2$ -error  $\epsilon$  produced by  $A_\lambda^M(f_K)$  is  
 850 equal to 0.0215 for the coarse sample set and to 0.00390 for the denser sample set, whereas it is  $\epsilon = 0.053594$   
 851 and  $\epsilon = 0.012515$  for the AMLE interpolant of the coarse and dense sample set, respectively. Compared with the  
 852 reconstruction of  $f$  from contour lines, where the sample points can be considered to be somehow organized, we  
 853 observe that both the reconstructed function  $A_\lambda^M(f_K)$  and the AMLE interpolant appear to be less regular, which  
 854 reflects the fact that the sample points are scattered over  $\Omega$  without any requirement of spacing or density. This  
 855 effect clearly reduces by increasing the density of the sample points, though for the AMLE interpolant we note  
 856 that the relative  $L^2$ -errors for the two cases of sampling density remains of the same order of magnitude. For this  
 857 example too, we finally verify that  $A_\lambda^M(f_K)$  is an interpolation of  $f_K$  given that the relative  $L^2$ -error  $\epsilon_K$  is of the  
 858 order  $10^{-16}$  for both the two test cases.

859 **7.2.3. Discontinuous piecewise affine function.** The discontinuous piecewise affine function  $f$  introduced  
 860 in Section 7.1.3 is evaluated here over the two sample sets  $K$  displayed in Figure 19(a) and Figure 19(b), to form  
 861 two sample functions  $f_K$  corresponding to a coarse and a dense sample set, respectively. The graph of  $A_\lambda^M(f_K)$   
 862 is displayed in Figure 24 for the two cases, along with their isolines, whereas Figure 25 shows the graph of the  
 863 AMLE interpolants along with their isolines with equally spaced heights. Also here, it is useful to compare such  
 864 isolines with those of the original function  $f$  displayed in Figure 18(d) for a visual assessment of the quality of  
 865 the reconstructions. Unlike the reconstruction of  $f$  from contour lines, where we had the exact sampling of the  
 866 discontinuity which was coincident with the grid lines, here we note an irregular behaviour for  $A_\lambda^M(f_K)$  around the

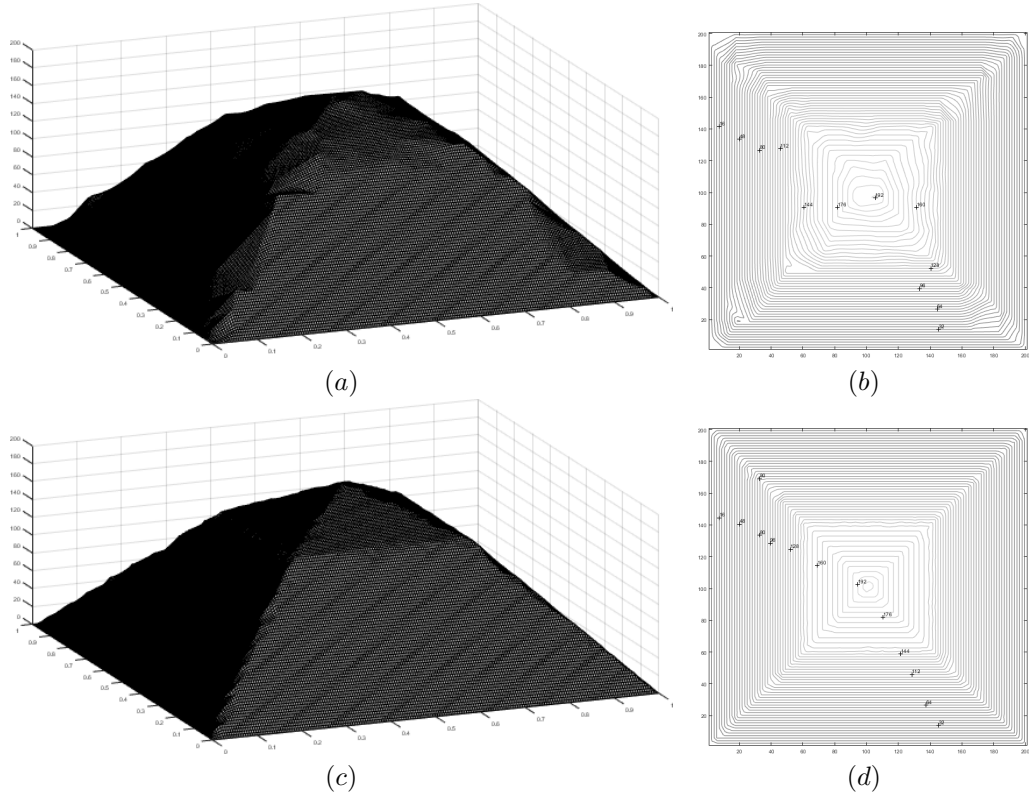


FIGURE 22. *Example 7.2.2.* (a) Graph of  $A_\lambda^M(f_K)$  for  $\lambda = 5 \cdot 10^4$ ,  $M = 1 \cdot 10^5$  and the set  $K$  of Figure 19(a). Relative  $L^2$ -Errors:  $\epsilon = 0.021574$ ,  $\epsilon_K = 4.4626 \cdot 10^{-16}$ . (b) Isolines of  $A_\lambda^M(f_K)$  at equally spaced heights equal to  $(\max(f) - \min(f))/50$ . (c) Graph of  $A_\lambda^M(f_K)$  for  $\lambda = 5 \cdot 10^4$ ,  $M = 1 \cdot 10^5$  and the set  $K$  of Figure 19(b). Relative  $L^2$ -Errors:  $\epsilon = 0.003914$ ,  $\epsilon_K = 6.2983 \cdot 10^{-16}$ . (d) Isolines of  $A_\lambda^M(f_K)$  at equally spaced heights equal to  $(\max(f) - \min(f))/50$ .

867 discontinuities of  $f$ . Such irregular behaviour reduces by increasing the sampling density, especially if such density  
 868 increase occurs in the neighborhood of the singularities. On the other hand, the AMLE interpolant displays around  
 869 the singularities a behaviour similar to the one obtained from the contour lines, with the difference that now the  
 870 transition from one affine part of  $f$  to the other appears to be smoother. As for the accuracy of the reconstructions,  
 871 for  $A_\lambda^M(f_K)$  we find that  $\epsilon = 0.173$  for the coarse sample set and  $\epsilon = 0.0901$  for the denser sample set, whereas  
 872 the relative  $L^2$ -error  $\epsilon_K$  on both sample sets  $K$  is of the order of  $10^{-16}$ , confirming that again,  $A_\lambda^M(f_K)$  is an  
 873 interpolant of  $f_K$ . For the AMLE interpolant, even in this case, we find higher values for the relative  $L^2$ -error, with  
 874  $\epsilon = 0.22577$  and  $\epsilon = 0.13897$  for the coarser and denser sample set, respectively. We note also the introduction of  
 875 artificial artefacts in the graph of the AMLE interpolant.

876 The relative  $L^2$ -errors obtained for scattered data approximation using  $A_\lambda^M$  and AMLE interpolation are  
 877 summarized in Table 2 for the examples considered in this section.

878 **7.2.4. DEM Reconstruction.** We consider here the problem of producing a Digital Elevation Map from a  
 879 sample of the the NASA SRTM global digital elevation model of Earth land. The data provided by the National  
 880 Elevation Dataset [27] contain geographical coordinates (latitude, longitude and elevation) of points sampled at  
 881 one arc-second intervals in latitude and longitude. For our experiments, we choose the region defined by the  
 882 coordinates  $[N 40^\circ 48' 50'', N 40^\circ 52' 50''] \times [E 14^\circ 45' 50'', E 14^\circ 50' 00'']$  extracted from the SRTM1 cell  $N40E014.hgt$   
 883 [1]. Such region consists of an area with extension  $7.413 \text{ Km} \times 5.844 \text{ km}$  and height varying between 266 m and  
 884 1600 m, with variegated topography features. In the digitization by the US Geological Survey, each pixel represents

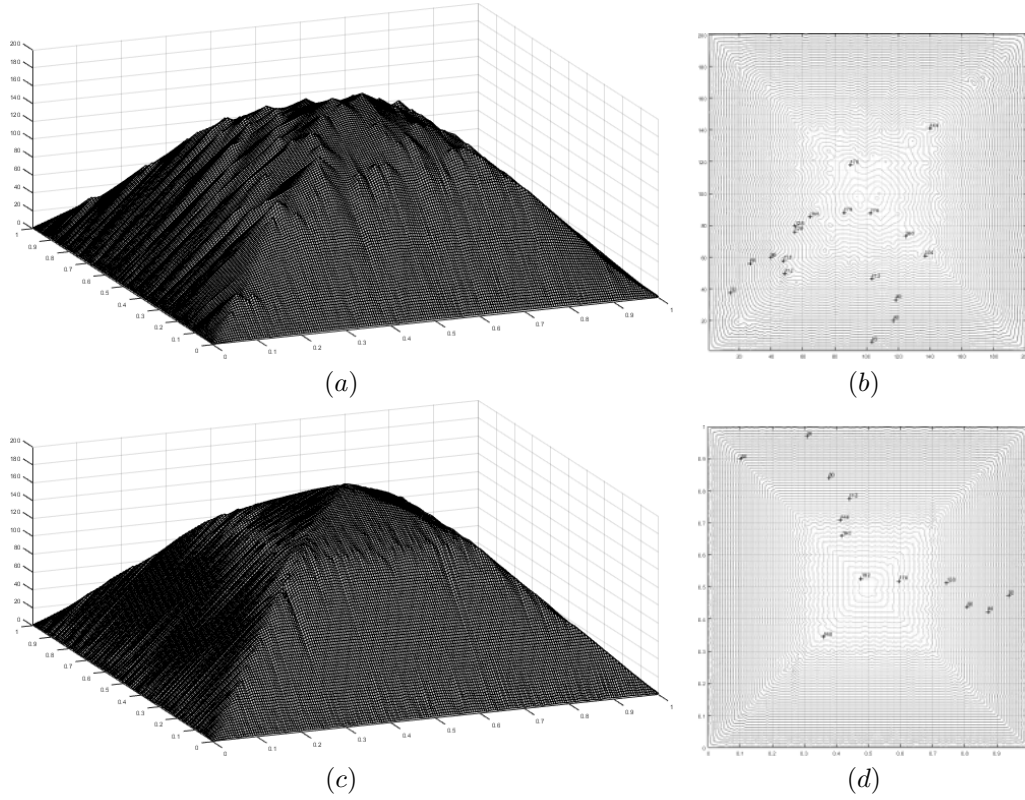


FIGURE 23. Example 7.2.2. (a) Graph of the AMLE interpolation function of  $f_K$  with  $K$  the set of scattered points displayed in Figure 19(a). Relative  $L^2$ -Error:  $\epsilon = 0.053594$ . (b) Isolines of the AMLE interpolant at equally spaced heights equal to  $(\max(f) - \min(f))/50$ . (c) Graph of the AMLE interpolation function of  $f_K$  with  $K$  the set of scattered points displayed in Figure 19(b). Relative  $L^2$ -Error:  $\epsilon = 0.012515$ . (d) Isolines of the AMLE interpolant at equally spaced heights equal to  $(\max(f) - \min(f))/50$ .

$f$	$K$	$\epsilon$	
		$A_\lambda^M(f_K)$	AMLE
F	coarse	0.0203	0.0576
	dense	0.0016	0.0109
CPA	coarse	0.0216	0.0536
	dense	0.0039	0.0125
DPA	coarse	0.1673	0.2258
	dense	0.0876	0.1390

TABLE 2

Accuracy of the interpolation for the examples considered in Section 7.2. Legenda:  $K$  Sample set.  $\epsilon$  Relative  $L^2$ -error.  $\epsilon_K$  Relative  $L^2$ -error on the sample set  $K$ .  $F$  Franke test function (Example 7.1.1).  $CPA$  Continuous piecewise affine function (Example 7.1.2).  $DPA$  Discontinuous piecewise affine function (Example 7.1.3).

Sample set	$\epsilon$	
	$A_\lambda^M(f_K)$	AMLE
$K_1$	0.0156	0.02137
$K_2$	0.0117	0.02261

TABLE 3

Relative  $L^2$ -error for the DEM Reconstruction from the two sample sets using the  $A_\lambda^M(f_K)$  and the AMLE interpolant.

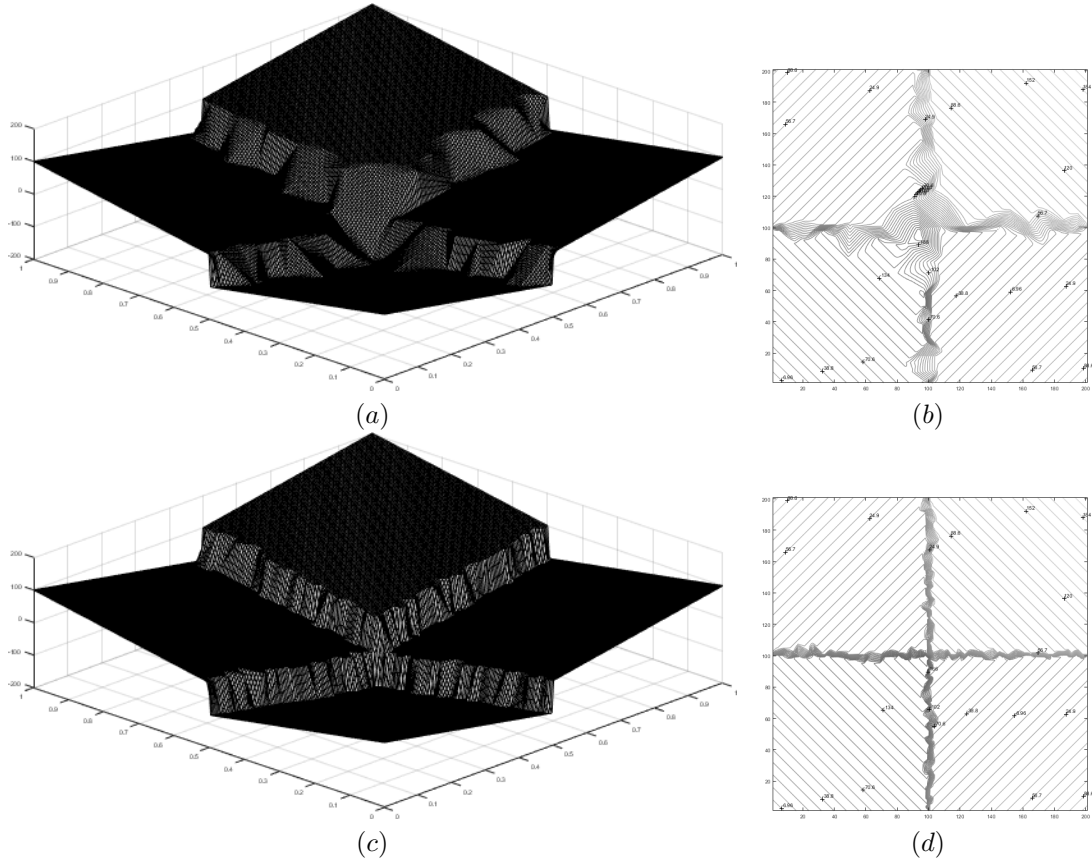


FIGURE 24. Example 7.2.3. (a) Graph of  $A_\lambda^M(f_K)$  for  $\lambda = 1 \cdot 10^7$ ,  $M = 1 \cdot 10^5$  and the set  $K$  of Figure 19(a). Relative  $L^2$ -Errors:  $\epsilon = 0.16729$ ,  $\epsilon_K = 1.2849 \cdot 10^{-16}$ . (b) Isolines of  $A_\lambda^M(f_K)$  at equally spaced heights equal to  $(\max(f) - \min(f))/50$ . (c) Graph of  $A_\lambda^M(f_K)$  for  $\lambda = 1 \cdot 10^7$ ,  $M = 1 \cdot 10^5$  and the set  $K$  of Figure 19(b). Relative  $L^2$ -Errors:  $\epsilon = 0.088589$ ,  $\epsilon_K = 1.459 \cdot 10^{-16}$ . (d) Isolines of  $A_\lambda^M(f_K)$  at equally spaced heights equal to  $(\max(f) - \min(f))/50$ .

885 a  $30\text{ m} \times 30\text{ m}$  patch. Figure 26(a) displays the elevation model from the SRTM1 data which we refer in the following  
 886 to as the ground truth model. We will take a sample  $f_K$  of such data, make the reconstruction using the  $A_\lambda^M(f_K)$   
 887 and the AMLE interpolant, and compare them with the ground truth model. In the numerical experiments, we  
 888 consider two sample data, characterized by different data density and typo of information. The first, which we  
 889 refer to as sample set  $K_1$ , consists only of level lines at regular height interval of 66 m and contains the 19% of  
 890 the ground truth real digital data. The second sample set, denoted by  $K_2$ , has been formed by taking randomly  
 891 the 30% of the points belonging to the level lines of the set  $K_1$  and scattered points corresponding to 5% density  
 892 so that the sample set  $K_2$  amounts to about 9% of the ground truth points. The two sample sets  $K_1$  and  $K_2$   
 893 are shown in Figure 26(b) and Figure 26(c), respectively. The graph of the  $A_\lambda^M(f_K)$  interpolant and of the AMLE  
 894 interpolant for the two sample sets along with the respective isolines at equally spaced heights equal to 66 m,  
 895 are displayed in Figure 27 and Figure 28, respectively, whereas Table 3 contains the values of the relative  $L^2$ -error  
 896 between such interpolants and the ground truth model. Though both reconstructions are comparable visually to  
 897 the ground truth model, a closer inspection of the pictures show that the reconstruction from the synthetic data,  
 898 the AMLE interpolant does not reconstruct correctly the mountains peaks, which appear to be smoothed, and  
 899 introduce artificial ridges along the slopes of the mountains. In contrast, the  $A_\lambda^M(f_K)$  interpolant appears to better  
 900 for capturing features of the ground truth model. Finally, we also note that though the sample set  $K_1$  contains a  
 901 number of ground truth points higher than the sample set  $K_2$ , the reconstruction from  $K_2$  appears to be better

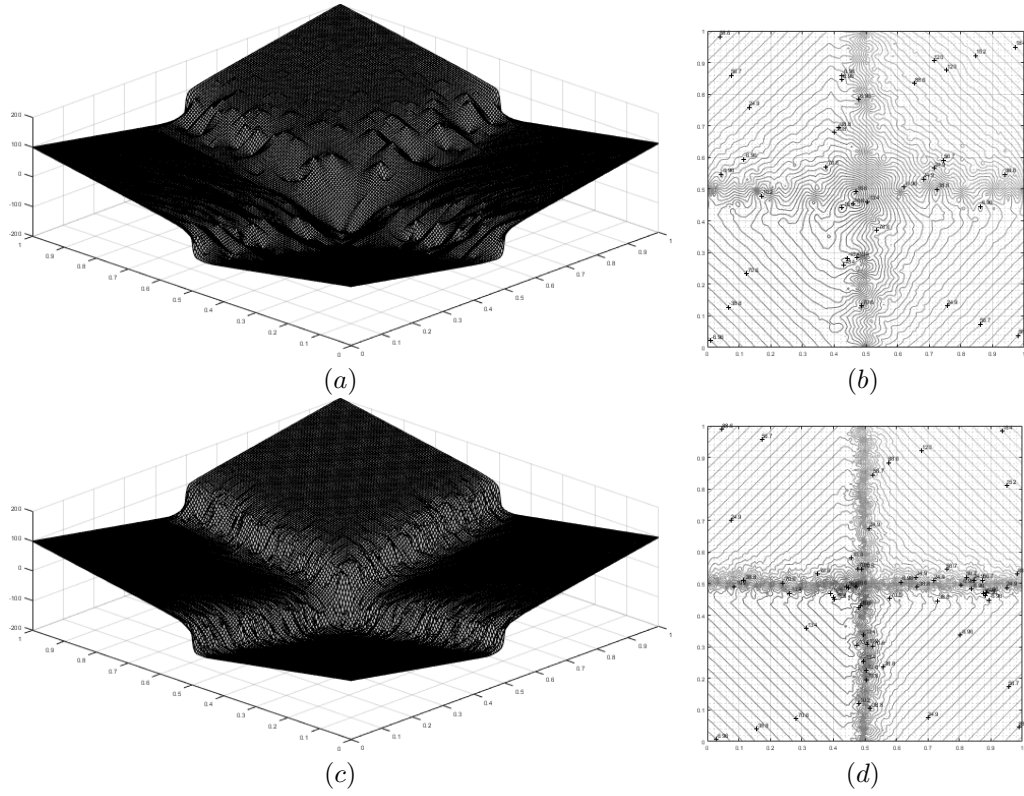


FIGURE 25. *Example 7.2.3.* (a) Graph of the AMLE interpolation function of  $f_K$  with  $K$  the set of scattered points displayed in Figure 19(a). Relative  $L^2$ -Error:  $\epsilon = 0.22577$ . (b) Isolines of the AMLE interpolant at equally spaced heights equal to  $(\max(f) - \min(f))/50$ . (c) Graph of the AMLE interpolation function of  $f_K$  with  $K$  the set of scattered points displayed in Figure 19(b). Relative  $L^2$ -Error:  $\epsilon = 0.13897$ . (d) Isolines of the AMLE interpolant at equally spaced heights equal to  $(\max(f) - \min(f))/50$ .

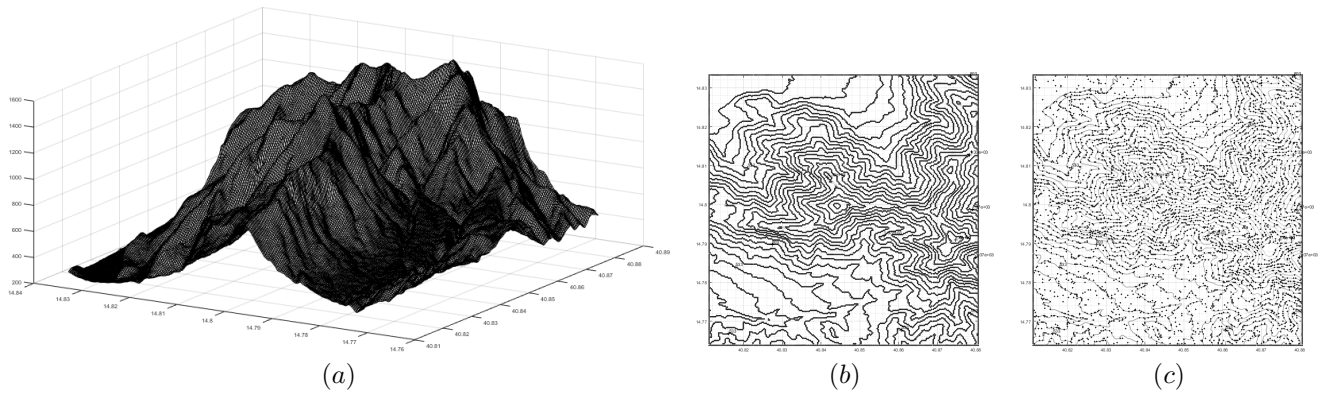


FIGURE 26. *Example 7.2.4.* Reconstruction of real-world digital elevation maps. (a) Ground truth model from USGS-STRM1 data relative to the area with geographical coordinates;  $[N 40^\circ 48' 50'', N 40^\circ 52' 50''] \times [E 14^\circ 45' 50'', E 14^\circ 50' 00'']$ . (b) Sample set  $K_1$  formed by only level lines at regular height interval of 66m. The set  $K_1$  contains 19% of the ground truth points. (c) Sample set  $K_2$  formed by taking randomly 30% of the points belonging to the level lines of the set  $K_1$  and scattered points corresponding to 5% density. The sample set  $K_2$  contains 9% of the ground truth points.

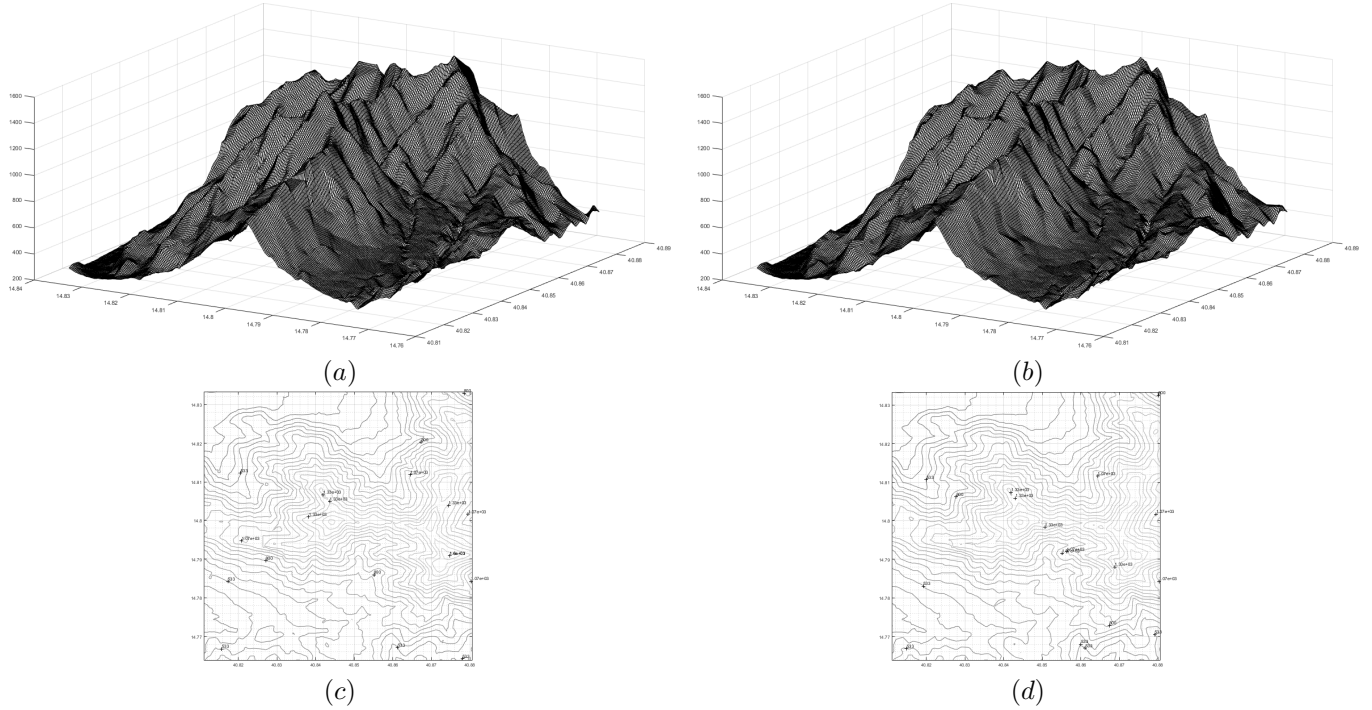


FIGURE 27. *Example 7.2.4. Reconstruction of real-world digital elevation maps. (a) Graph of  $A_\lambda^M(f_K)$  for sample set  $K_1$ . Parameters:  $\lambda = 1 \cdot 10^3$ ,  $M = 1 \cdot 10^6$ . Relative  $L^2$ -Errors:  $\epsilon = 0.01560$ ,  $\epsilon_K = 0$ . (b) Graph of  $A_\lambda^M(f_K)$  for sample set  $K_2$ . Parameters:  $\lambda = 1 \cdot 10^3$ ,  $M = 1 \cdot 10^6$ . Relative  $L^2$ -Errors:  $\epsilon = 0.01117$ ,  $\epsilon_K = 0$ . (c) Isolines of  $A_\lambda^M(f_K)$  from sample set  $K_1$  at regular heights of 66 m. (d) Isolines of  $A_\lambda^M(f_K)$  from sample set  $K_2$  at regular heights of 66 m.*

902 than the one obtained from  $K_1$ . This behaviour was found for both interpolations, though it is more notable in the  
 903 case of the  $A_\lambda^M(f_K)$  interpolant. By taking scattered data, we are able to get a better characterization of irregular  
 904 surfaces, compared to the one obtained from a structured representation such as provided by the level lines.

905 **7.2.5. Salt & Pepper Noise Removal.** As an application of scattered data approximation to image pro-  
 906 cessing, we consider here the restoration of an image corrupted by salt & pepper noise. This is an impulse type noise  
 907 that is caused, for instance, by malfunctioning pixels in camera sensors or faulty memory locations in hardware,  
 908 so that information is lost at the faulty pixels and the corrupted pixels are set alternatively to the minimum or  
 909 to the maximum value of the range of the image values. When the noise density is low, about less than 40%, the  
 910 median filter is quite effective for restoring the image. However, this filter loses its denoising power for higher noise  
 911 density given that details and features of the original image are smeared out. In those cases, other techniques  
 912 must be applied; one possibility is the two-stage TV-based method proposed in [14]. In the following numerical  
 913 experiments, we consider the image displayed in Figure 29(a) with size  $512 \times 512$  pixels, damaged by 70% salt &  
 914 pepper noise. The resulting corrupted image is displayed in Figure 29(b) where only 78643 pixels out of the total  
 915 262144 pixels carry true information. The true image values represent our sample function  $f_K$  whereas the set of  
 916 the true pixels forms our sample set  $K$ . To assess the restoration performance we use the peak signal-to-noise ratio  
 917 (PSNR) which is expressed in the units of dB and, for an 8-bit image, is defined by

$$918 \quad (7.5) \quad \text{PSNR} = 10 \log_{10} \frac{255^2}{\frac{1}{mn} \sum_{i,j} |f_{i,j} - r_{i,j}|^2}$$

919 where  $f_{i,j}$  and  $r_{i,j}$  denote the pixels values of the original and restored image, respectively, and  $m, n$  denote the  
 920 size of the image  $f$ . In our numerical experiments, we have considered the following cases. The first one assumes

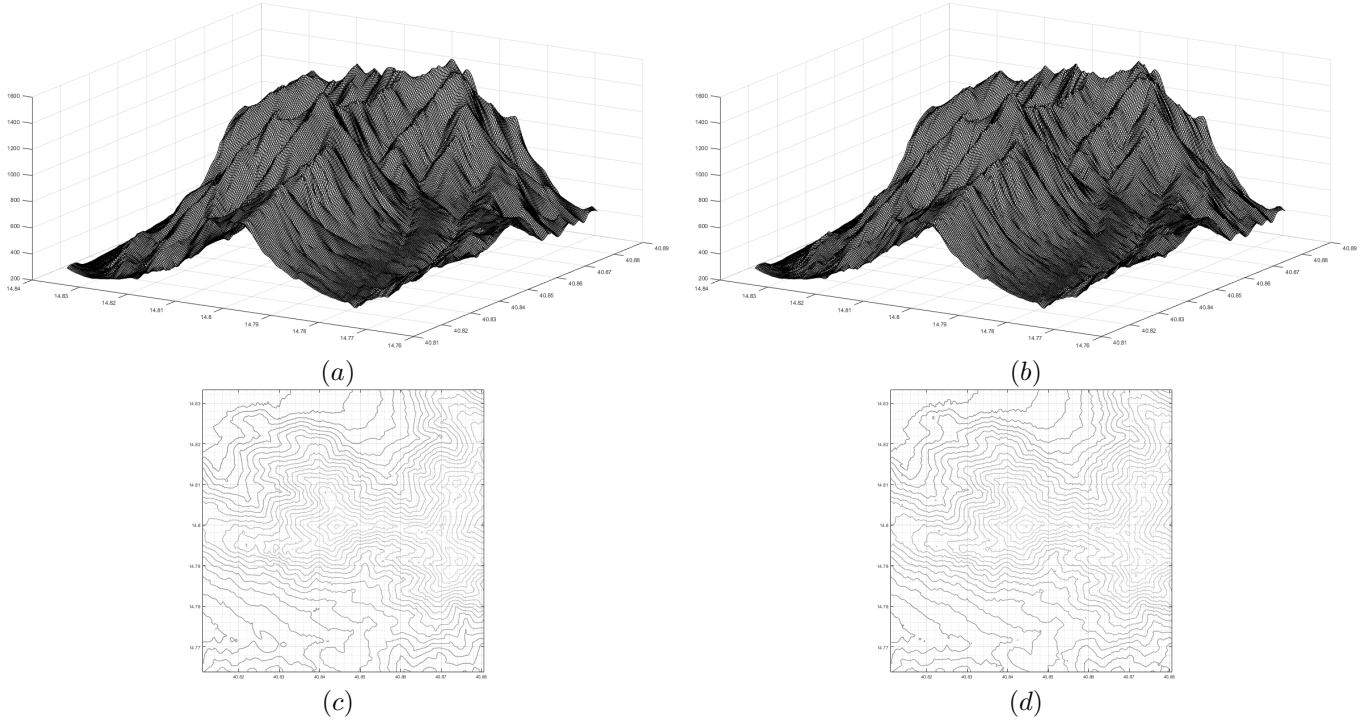


FIGURE 28. *Example 7.2.4. Reconstruction of real-world digital elevation maps. (a) Graph of the AMLE Interpolant from set  $K_1$ . Relative  $L^2$ -Error:  $\epsilon = 0.0214$ . (b) Graph of the AMLE Interpolant from set  $K_2$ . Relative  $L^2$ -Error:  $\epsilon = 0.0226$ . (c) Isolines of the AMLE Interpolant from sample set  $K_1$  at regular heights of 66 m. (d) Isolines of the AMLE Interpolant from sample set  $K_2$  at regular heights of 66 m.*

921 the set  $K$  to be given by the noise-free interior pixels of the corrupted image together with the boundary pixels of  
 922 the original image. In the second case,  $K$  is just the set of the noise-free pixels of the corrupted image, without  
 923 any special consideration on the image boundary pixels. In analysing this second case, to reduce the boundary  
 924 effects produced by the application of Algorithm 1, we have applied our method to an enlarged image and then  
 925 restricted the resulting restored image to the original domain. The enlarged image has been obtained by padding  
 926 a fixed number of pixels before the first image element and after the last image element along each dimension,  
 927 making mirror reflections with respect to the boundary. The values used for padding are all from the corrupted  
 928 image. In our examples, we have considered two versions of enlarged images, obtained by padding the corrupted  
 929 image with 2 pixels and 10 pixels, respectively. Table 4 compares the values of the PSNR of the restored images  
 930 by our method and the TV-based method applied to the corrupted image with noise-free boundary and to the two  
 931 versions of the enlarged images with the boundary values of the enlarged images given by the padded noisy image  
 932 data. We observe that there are no important variations in the denoising result between the different methods of  
 933 treating the image boundary. This is also reflected by the close value of the PSNR of the resulting restored images.  
 934 For 70% salt & pepper noise, Figure 29(c) displays the restored image  $A_\lambda^M(f_K)$  with  $K$  equal to the true set that  
 935 has been enlarged by two pixels, whereas Figure 29(d) shows the restored image by the TV-based method [12, 14]  
 936 using the same set  $K$ . Although the visual quality of the images restored from 70% noise corruption is comparable  
 937 between our method and the TV-based method, the PSNR using our method is higher than that for the TV-based  
 938 method in all of the experiments reported in Table 4. An additional advantage of our method is its speed. Our  
 939 method does not require initialisation which is in contrast with the two-stage TV-based method, for which the  
 940 initialisation, for instance, is given by the restored image using an adaptive median filter.

941 Finally, to demonstrate the performance of our method in some extreme cases of very sparse data, we consider

942 cases of noise density equal to 90% and 99%. Figure 30 displays the restored image by the compensated convexity  
 943 based method and by the TV-based method for cases where  $K$  are padded by two pixels and ten pixels for 90% and  
 944 99% noise level, respectively. As far as the visual quality of the restored images is concerned, and to the extent that  
 945 such judgement can make sense given the high level of noise density, the inspection of Figure 30 seems to indicate  
 946 that  $A_\lambda^M(f_K)$  gives a better approximation of details than the TV-based restored image. This is also reflected by  
 947 the values of the PSNR index in Table 4.

Noise Density	PSNR					
	$K$ with noise-free boundary		$K$ padded by two pixels		$K$ padded by ten pixels	
	$A_\lambda^M(f_K)$	TV	$A_\lambda^M(f_K)$	TV	$A_\lambda^M(f_K)$	TV
70% (6.990 dB)	31.910 dB	31.175 dB	31.865 dB	31.134 dB	31.869 dB	31.136 dB
90% (5.901 dB)	27.574 dB	26.625 dB	27.506 dB	26.564 dB	27.513 dB	26.566 dB
99% (5.492 dB)	22.076 dB	20.595 dB	21.761 dB	20.469 dB	21.972 dB	20.492 dB

TABLE 4

Comparison of PSNR of the restored images by the compensated convexity based method ( $A_\lambda^M(f_K)$ ) and by the two-stage TV-based method (TV), for different sets  $K$ .

948 **7.3. Image inpainting.** As an example of image inpainting, we consider the problem of removing text  
 949 overprinted on the image displayed in Figure 31(a). If we denote by  $P$  the set of pixels containing the overprinted  
 950 text, and by  $\Omega$  the domain of the whole image, then  $K = \Omega \setminus P$  is the set of the true pixels and the inpainting  
 951 problem is in fact the problem of reconstructing the image over  $P$  from knowing  $f_K$ , if we denote by  $f$  the original  
 952 image values. To assess the performance of our reconstruction compared to state-of-art inpainting methods, we  
 953 compare our method with the total variation based image inpainting method solved by the split Bregman method  
 954 described in [29] and with the AMLE inpainting reported in [45]. The restored image  $A_\lambda^M(f_K)$  obtained by our  
 955 compensated convexity method is displayed in Figure 31(b), the restored image by the AMLE method is shown  
 956 in Figure 31(d) whereas 31(c) presents the restored image by the the split Bregman inpainting method. All the  
 957 restored images look visually quite good. However, if we use the PSNR as a measure of the quality of the restoration,  
 958 we find that  $A_\lambda^M(f_K)$  has a value of PSNR equal to 42.2066 dB, the split Bregman inpainting restored image gives  
 959 a value for PSNR = 41.0498 dB, whereas the AMLE restored image has PSNR equal to 39.4405 dB.

960 Finally, to assess how well  $A_\lambda^M(f_K)$  is able to preserve image details and not to introduce unintended effects  
 961 such as image blurring and staircase effects, Figure 32 displays details of the original image and of the restored  
 962 images by the three methods. Once again, the good performance of  $A_\lambda^M(f_K)$  can be appreciated visually.

## 963 8. Proofs of the Main Results.

964 *Proof.* (Proposition 2.8) We write  $(x, y) \in \mathbb{R}^{n+m}$  with  $x \in \mathbb{R}^n$  and  $y \in \mathbb{R}^m$ . We only prove the result for the  
 965 upper transform as the proof of the lower transform is similar. By the definition of the upper transform, we have

$$966 \quad \text{co}[\lambda \cdot |\cdot|^2 - f](x) = \lambda|x|^2 - C_\lambda^u(f(x)), \quad x \in \mathbb{R}^n.$$

967 We show that  $\text{co}[\lambda \cdot |\cdot|^2 - f](x)$  is also the convex envelope of the function  $\lambda(|x|^2 + |y|^2) - g^{-M}(x, y)$  restricted to  
 968  $z = 0$ . By definition,

$$969 \quad \lambda|x|^2 - C_\lambda^u(f(x)) = \text{co}[\lambda \cdot |\cdot|^2 - f](x) \leq \lambda|x|^2 - f(x) \leq \lambda(|x|^2 + |y|^2) - g^{-M}(x, y)$$

970 as  $f(x) \geq g^{-M}(x, y)$  for all  $x \in \mathbb{R}^n$  and  $y \in \mathbb{R}^m$ . Thus for  $y = 0$ ,

$$971 \quad \text{co}[\lambda \cdot |\cdot|^2 - f](x) \leq \text{co}[\lambda(|x|^2 + |y|^2) - g^{-M}(x, y)]|_{y=0}.$$

972 On the other hand,

$$973 \quad \text{co}[\lambda(|x|^2 + |y|^2) - g^{-M}(x, y)]|_{y=0} \leq \lambda|x|^2 - g^{-M}(x, 0) = \lambda|x|^2 - f(x).$$

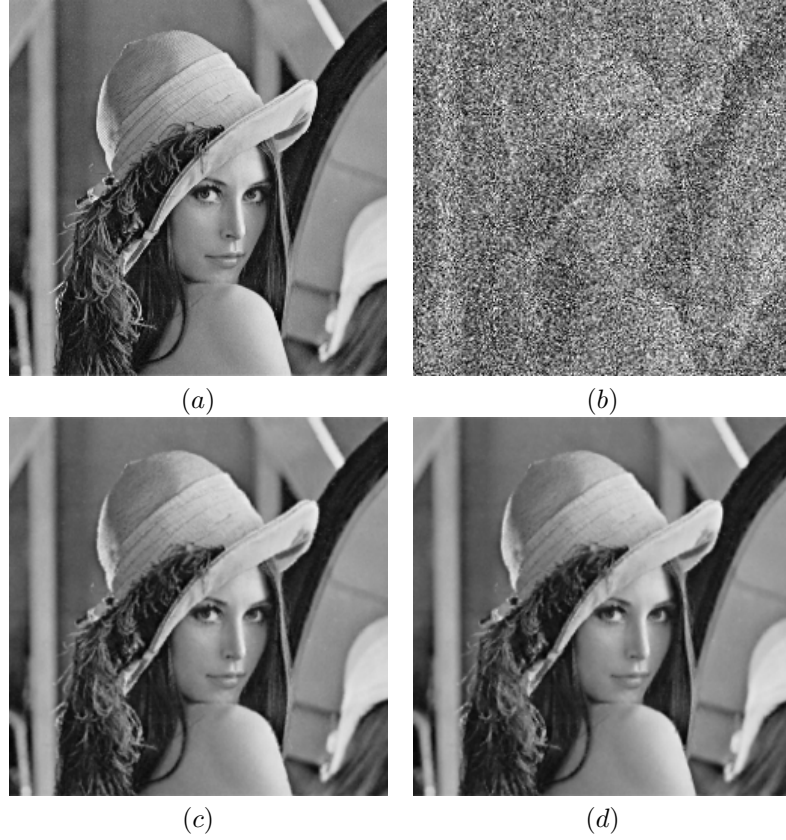


FIGURE 29. *Example 7.2.5.* (a) Original image with size  $512 \times 512$ ; (b) Original image covered by a salt & pepper noise density of 70%. PSNR = 6.99 dB; (c) Restored image  $A_\lambda^M(f_K)$  with  $K$  the set of the pixels not corrupted by the salt & pepper noise when the corrupted image is enlarged symmetrically by two pixels on each side,  $\lambda = 15$  and  $M = 1E13$ . PSNR = 31.865 dB. If the boundary pixels were noise-free, the corresponding restored image would have PSNR = 31.910 dB. (d) Restored image by the two-stage TV-based method described in [12, 14] with  $K$  the set of the pixels not corrupted by the salt & pepper noise when the corrupted image is enlarged symmetrically by two pixels on each side. PSNR = 31.134 dB. If the boundary pixels were noise-free, the corresponding restored image would have PSNR = 31.175 dB.

974 Since the restriction of a convex function to a linear subspace remains convex, we also see that

$$975 \quad \text{co}[\lambda(|x|^2 + |y|^2) - g^{-M}(x, y)]|_{y=0} \leq \text{co}[\lambda \cdot |\cdot|^2 - f](x).$$

976 Thus

$$977 \quad \text{co}[\lambda(|x|^2 + |y|^2) - g^{-M}(x, z)]|_{y=0} = \text{co}[\lambda \cdot |\cdot|^2 - f](x),$$

978 hence the conclusion follows.  $\square$

*Proof.* (**Theorem 3.1**) Note first that it follows from the fact that  $a_0 < a_1 < \dots < a_m$ ,  $m \in \mathbb{N}$ , that  $V_{a_i} \subset V_{a_j}$  for all  $0 \leq i < j \leq m$ . Also, by the translation invariant property of compensated convex transforms, we may assume without loss of generality that  $x_0 = 0$ , so that

$$C_\lambda^l(f_K^M)(0) = \text{co}[f_K^M + \lambda \cdot |\cdot|^2](0), \quad C_\lambda^u(f_K^{-M})(0) = \text{co}[\lambda \cdot |\cdot|^2 - f_K^{-M}](0).$$

979 (i): Suppose that  $x_0 = 0 \in \Gamma_{a_k}$  and consider the constant function  $\ell(x) = a_k$ . Clearly  $a_k = f_K^M(0) + \lambda|0|^2$ . Next  
 980 we show that  $a_k \leq f_K^M(x) + \lambda|x|^2$  for  $x \in \Gamma_{a_j}$  for  $j \neq k$ . Thus we need to prove that  $a_k \leq a_j + \lambda|x|^2$ . Since  $0 \in \Gamma_{a_k}$   
 981 and  $x \in \Gamma_{a_j}$ , we have  $|x|^2 \geq \delta_0^2$ . Under our assumption on  $\lambda$ , we see that  $a_k \leq a_j + \lambda|x|^2$  holds. Since  $a_k < M$ , we



FIGURE 30. *Example 7.2.5. Restoration of 90% corrupted image (PSNR = 5.901 dB) by: (a) Restored image  $A_\lambda^M(f_K)$ , with  $K$  the set of the pixels not corrupted by the salt & pepper noise when the corrupted image is enlarged symmetrically by two pixels on each side,  $\lambda = 15$  and  $M = 1E13$ . PSNR = 27.506 dB. (b) Restored Image by the two-stage TV-based method described in [12, 14] with the same set  $K$  as in (a). PSNR = 26.564 dB. Restoration of 99% corrupted image (PSNR = 5.492 dB) by: (c) Restored image  $A_\lambda^M(f_K)$ , with  $K$  the set of the pixels not corrupted by the salt & pepper noise when the corrupted image is enlarged symmetrically by ten pixels on each side,  $\lambda = 15$  and  $M = 1E13$ . PSNR = 21.972 dB. (d) Restored Image by the two-stage TV-based method described in [12, 14] with the same set  $K$  as in (c). PSNR = 20.492 dB.*

982 have  $a_k \leq f_K^M(x) + \lambda|x|^2$  for all  $x \in \mathbb{R}^n$ , hence  $C_\lambda^l(f_K^M)(0) = a_k$ . Similarly we can show that  $C_\lambda^u(f_K^{-M})(0) = a_k$ , so  
 983 that  $A_\lambda^M(f_K)(0) = a_k$ .

984

985 (ii): Since (i) clearly ensures that (3.2) holds whenever  $f(x_0) = a_i$  for some  $0 \leq i \leq m$ , it remains to consider  
 986  $x_0 = 0$  such that  $a_i < f(x_0) < a_{i+1}$  for some  $0 \leq i \leq m - 1$ . Now define

$$987 \quad (8.1) \quad f_{K_i^-}^M(x) = \begin{cases} f_K^M(x), & x \notin \Gamma_{a_{i+1}}, \\ a_i, & x \in \Gamma_{a_{i+1}}; \end{cases} \quad f_{K_i^+}^M(x) = \begin{cases} f_K^M(x), & x \notin \Gamma_{a_i}, \\ a_{i+1}, & x \in \Gamma_{a_i}. \end{cases}$$

988 Clearly  $f_{K_i^-}^M(x) \leq f_K^M(x) \leq f_{K_i^+}^M(x)$  and  $f_{K_i^-}^{-M}(x) \leq f_K^{-M}(x) \leq f_{K_i^+}^{-M}(x)$  for  $x \in \mathbb{R}^n$ , so that

$$989 \quad (8.2) \quad C_\lambda^l(f_{K_i^-}^M)(x) \leq C_\lambda^l(f_K^M)(x) \leq C_\lambda^l(f_{K_i^+}^M)(x), \quad C_\lambda^u(f_{K_i^-}^{-M})(x) \leq C_\lambda^u(f_K^{-M})(x) \leq C_\lambda^u(f_{K_i^+}^{-M})(x), \quad x \in \mathbb{R}^n$$

990 and hence by definition,

$$991 \quad (8.3) \quad A_\lambda^M(f_{K_i^-})(x) \leq A_\lambda^M(f_K)(x) \leq A_\lambda^M(f_{K_i^+})(x), \quad x \in \mathbb{R}^n.$$

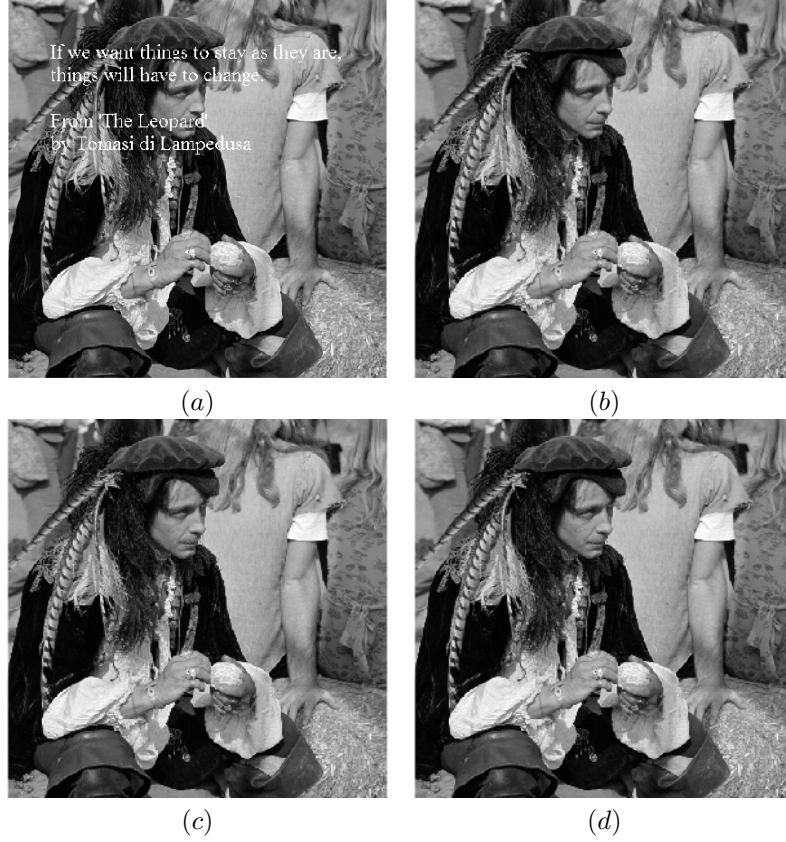


FIGURE 31. *Example 7.3. Inpainting of the text overprinted on an image: (a) Original image with overprinted text. (b) Restored image  $A_{\lambda}^M(f_K)$  with  $K$  the set to be inpainted,  $\lambda = 250$  and  $M = 1 \cdot 10^4$ . Computed value for PSNR = 42.2066 dB; Relative  $L^2$ -error  $\epsilon = 0.016139$ . (c) Restored image by the AMLE method described in [45, 39]. Computed value for PSNR = 39.4405 dB. Relative  $L^2$ -error  $\epsilon = 0.022192$ . (d) Restored image by the Split Bregman inpainting method described in [29]. Computed value for PSNR = 41.0498 dB. Relative  $L^2$ -error  $\epsilon = 0.018438$ .*

992 Next we will prove that

993 (8.4) 
$$A_{\lambda}^M(f_{K_i^-})(0) = a_i, \quad A_{\lambda}^M(f_{K_i^+})(0) = a_{i+1}.$$

994 We first show that  $\text{co}[f_{K_i^-}^M + \lambda|\cdot|^2](0) \geq a_i$ . Clearly  $a_i \leq a_i + \lambda|x|^2 = f_{K_i^-}^M(x) + \lambda|x|^2$  for  $x \in \Gamma_{a_i} \cup \Gamma_{a_{i+1}}$ . For  
 995  $x \in \Gamma_{a_j}$  with  $j \neq i, i + 1$ ,  $a_i \leq a_j + \lambda|x|^2$  if  $a_i - a_j \leq \lambda|x|^2$ . This inequality holds if  $a_m - a_0 \leq \lambda\delta_0^2$ , that is, for  
 996  $\lambda \geq (a_m - a_0)/\delta_0^2$  which is what we have assumed. The inequality  $|x| \geq \delta_0$  for  $x \in \Gamma_{a_j}$  can be proved by applying  
 997 the intermediate value theorem to  $f$ . If  $j < i$ , as  $f(0) > a_i$  and  $f(x) = a_j < a_i$ , we have, by the intermediate value  
 998 theorem, that there is some  $\xi \in (0, 1)$  such that  $f(\xi x) = a_i$ , that is,  $\xi x \in \Gamma_{a_i}$ . Thus  $|x| > (1 - \xi)|x| = |x - \xi x| \geq \delta_0$   
 999 as  $x \in \Gamma_{a_j}$  and  $\xi x \in \Gamma_{a_i}$ . If  $j > i + 1$ , we have  $f(0) < a_{i+1}$  and  $f(x) = a_j > a_{i+1}$ . Again we can use the same  
 1000 method to show that  $|x| \geq \delta_0$ .

1001 By definition of the convex envelope, we see that there is an affine function  $\ell$  such that  $\ell(x) \leq f_{K_i^-}^M(x) + \lambda|x|^2$   
 1002 for  $x \in \mathbb{R}^n$  and  $\ell(0) = \text{co}[f_{K_i^-}^M + \lambda|\cdot|^2](0)$ . From the proof above, we see that  $\ell(0) \geq a_i$ . Furthermore, if we let  
 1003  $K_l = \{x \in \mathbb{R}^n, \ell(x) = f_{K_i^-}^M(x) + \lambda|x|^2\}$ , then  $0 \in \text{co}[K_l]$  and  $\ell(x) = \text{co}[f_{K_i^-}^M + \lambda|\cdot|^2](x)$  for  $x \in \text{co}[K_l]$ .

1004 By [55, Proposition 3.3], we see that  $K_l \subset K$ . Now we show that  $K_l \subset \Gamma_{a_i} \cup \Gamma_{a_{i+1}}$ . If this is not the case, then  
 1005  $K_l \cap \Gamma_{a_k} \neq \emptyset$  for some  $k \notin \{i, i + 1\}$ . We consider two different cases: (a):  $k < i$  and (b):  $k > i + 1$ . For the case

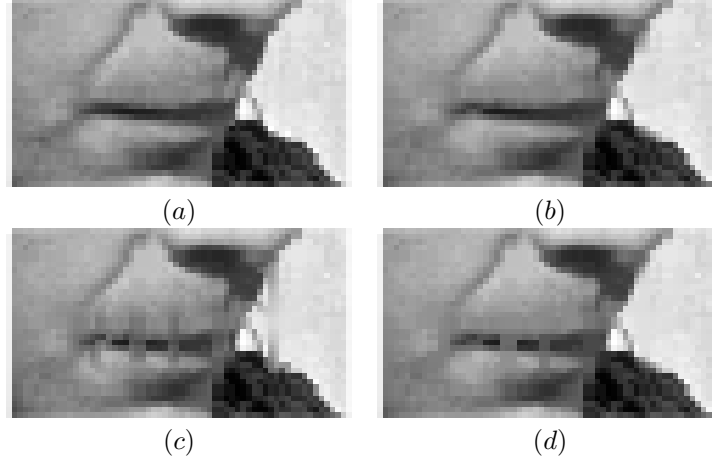


FIGURE 32. *Example 7.3. Comparison of a detail of the original image with the corresponding detail of the restored images according to the compensated convexity method and the TV-based method: (a) Lips detail of the original image without overprinted text. (b) Lips detail of the restored image  $A_\lambda^M(f_K)$ . (c) Lips detail of the AMLE-based restored image. (d) Lips detail of the TV-based restored image.*

1006 (a), we see that there is some  $x^* \in K_l \cap \Gamma_{a_k}$ . Thus  $\ell(x^*) = a_k + \lambda|x^*|^2$ . As  $f(0) > a_i$  and  $f(x^*) = a_k < a_i$ , similar  
 1007 to the proof above, by the intermediate value theorem, we have that there is some  $\xi \in (0, 1)$  such that  $f(\xi x^*) = a_i$ .  
 1008 Therefore,  $\xi x^* \in \Gamma_{a_i}$  so that  $\ell(\xi x^*) \leq f_{K_i}^M(\xi x^*)$ . This implies

$$1009 \quad (8.5) \quad (1 - \xi)\ell(0) + \xi\ell(x^*) \leq a_i + \lambda|\xi x^*|^2.$$

1010 As  $\ell(0) \geq a_i$  and  $\ell(x^*) = a_k + \lambda|x^*|^2$  so that (8.5) implies that

$$1011 \quad (8.6) \quad (1 - \xi)a_i + \xi(a_k + \lambda|x^*|^2) \leq a_i + \lambda|\xi x^*|^2$$

1012 that is

$$1013 \quad (8.7) \quad \xi(1 - \xi)\lambda|x^*|^2 \leq \xi(a_i - a_k).$$

1014 Thus we have found that for  $0 < \xi < 1$

$$1015 \quad (8.8) \quad \lambda(1 - \xi)|x^*|^2 \leq (a_i - a_k).$$

1016 Since  $\lambda(1 - \xi)|x^*|^2 \geq \lambda(1 - \xi)^2|x^*|^2 \geq \lambda\delta_0^2$  and  $a_i - a_k \leq a_m - a_0$ , we have  $\lambda\delta_0^2 \leq a_m - a_0$ , which contradicts our  
 1017 assumption on  $\lambda$ .

1018 If the case (b) occurs, we have  $f(0) < a_{i+1}$  and  $f(x^*) = a_k > a_{i+1}$ . Again by the intermediate value theorem, there  
 1019 is some  $\xi \in (0, 1)$  such that  $f(\xi x^*) = a_{i+1}$ . However note that here the value of  $f_{K_i}^M$  on  $\Gamma_{a_{i+1}}$  is  $a_i$ . Therefore  
 1020 a similar argument to that for case (a) will lead to a contradiction. Thus in both cases we have proved that  
 1021  $K_l \subset \Gamma_{a_i} \cup \Gamma_{a_{i+1}}$ .

1022 Now we consider  $C_\lambda^u(f_{K_i}^{-M})(0) = \text{co}[\lambda|\cdot|^2 - f_{K_i}^{-M}](0)$ . Let  $\hat{\ell}$  be the affine function such that  $\hat{\ell}(x) \leq \lambda|x|^2 - f_{K_i}^{-M}(x)$ ,  
 1023  $\hat{\ell}(0) = \text{co}[\lambda|\cdot|^2 - f_{K_i}^{-M}](0)$  and let  $K_u = \{x \in K, \hat{\ell}(x) = \lambda|x|^2 - f_{K_i}^{-M}(x)\}$ . Again we have  $\hat{\ell}(0) \geq -a_i$  and we can

1024 also show that  $K_u \subset \Gamma_{a_i} \cup \Gamma_{a_{i+1}}$ . By the definition of the convex envelope, we have

$$\begin{aligned}
 & \text{co}[f_{K_i^-}^M + \lambda|\cdot|^2](0) \\
 &= \inf \left\{ \sum_{k=1}^{n+1} \lambda_k \left( f_{K_i^-}^M(x_k) + \lambda|x_k|^2 \right), x_k \in \mathbb{R}^n, \lambda_k \geq 0, \sum_{k=1}^{n+1} \lambda_k = 1, \sum_{k=1}^{n+1} \lambda_k x_k = 0 \right\} \\
 &= \inf \left\{ \sum_{k=1}^{n+1} \lambda_k \left( f_{K_i^-}^M(x_k) + \lambda|x_k|^2 \right), x_k \in K_l, \lambda_k \geq 0, \sum_{k=1}^{n+1} \lambda_k = 1, \sum_{k=1}^{n+1} \lambda_k x_k = 0 \right\} \\
 1025 \quad (8.9) \quad &= \inf \left\{ \sum_{k=1}^{n+1} \lambda_k \left( f_{K_i^-}^M(x_k) + \lambda|x_k|^2 \right), x_k \in K_l \cup K_u, \lambda_k \geq 0, \sum_{k=1}^{n+1} \lambda_k = 1, \sum_{k=1}^{n+1} \lambda_k x_k = 0 \right\} \\
 &= a_i + \inf \left\{ \sum_{k=1}^{n+1} \lambda_k \lambda |x_k|^2, x_k \in K_l \cup K_u, \lambda_k \geq 0, \sum_{k=1}^{n+1} \lambda_k = 1, \sum_{k=1}^{n+1} \lambda_k x_k = 0 \right\} \\
 &=: a_i + C_0.
 \end{aligned}$$

1026 Similarly, we have  $\text{co}[\lambda|\cdot|^2 - f_{K_i^-}^{-M}](0) = -a_i + C_0$ , and hence

$$1027 \quad (8.10) \quad A_\lambda^M(f_{K_i^-})(0) = \frac{1}{2} \left( \text{co}[f_{K_i^-}^M + \lambda|\cdot|^2](0) - \text{co}[\lambda|\cdot|^2 - f_{K_i^-}^{-M}](0) \right) = a_i.$$

1028 By using the same argument as above, we can also show that  $A_\lambda^M(f_{K_i^+})(0) = a_{i+1}$  and this proves (8.4).

1029

1030 (*iii*): Suppose  $f(0) < a_0$ . If we let  $\ell$  be the affine function such that  $\ell(x) \leq f_K^M(x) + \lambda|x|^2$ ,  $\ell(0) = \text{co}[f_K^M + \lambda|\cdot|^2](0)$   
 1031 and let  $K_l = \{x \in \text{co}[K], \ell(x) = f_K^M(x) + \lambda|x|^2\}$ , then in this special case we only need to show that  $K_l \subset \Gamma_{a_0}$ .  
 1032 As  $a_0 < a_1 < \dots < a_m$ , we only need to rule out one possibility that  $K_l \cap \Gamma_i \neq \emptyset$  for any  $0 < i \leq m$ . By following  
 1033 the arguments of the proof of (*ii*)(*b*), we can show that  $K_l \subset \Gamma_0$ . Similarly we can also show that  $K_u \subset \Gamma_0$ ,  
 1034 where  $K_u = \{x \in \text{co}[K], \hat{\ell}(x) = \lambda|x|^2 - f_K^{-M}(x)\}$  for the affine function  $\hat{\ell}$  such that  $\hat{\ell}(x) \leq \lambda|x|^2 - f_K^{-M}(x)$  and  
 1035  $\hat{\ell}(0) = \text{co}[\lambda|\cdot|^2 - f_K^{-M}](0)$ . The proof is then similar to that of part (*ii*). Note that here we do not have to  
 1036 introduce functions  $f_{K_0^+}^M$  and  $f_{K_0^-}^M$  as in (*ii*) given that the condition we have is  $f(0) < a_0$  while in (*ii*) we had  
 1037  $a_i < f(0) < a_{i+1}$ .  $\square$

1038 *Proof.* (Proposition 3.3) (*i*): Without loss of generality, we may assume  $x_0 = 0 \in \Omega_i$ . Now note that Corollary  
 1039 2.7, applied with  $f, r$  and  $R$  given by  $\tilde{f}, R$  and  $R + 1$  respectively, gives that

$$1040 \quad (8.11) \quad |A_\lambda^M(\tilde{f}_{K_{R+1}})(0) - \tilde{f}(0)| \leq \tilde{\omega} \left( r_c(0) + \frac{\tilde{a}}{\lambda} + \sqrt{\frac{2\tilde{b}}{\lambda}} \right).$$

1041 Then since  $0 \in \Omega_i \subset V_{a_m}$ , it follows that  $\tilde{f}(0) = f(0)$ , and also that  $r_c(0) \leq d_i(0)$ , by (2.9). To prove (3.5), it thus  
 1042 remains to show that  $A_\lambda^M(\tilde{f}_{K_{R+1}})(0) = A_\lambda^M(f_K)(0)$ . To see this, note first that by arguments similar to those in  
 1043 the proof of [55, Theorem 3.7], we have that

$$1044 \quad (8.12) \quad C_\lambda^l(\tilde{f}_{K_{R+1}}^M)(0) = \sum_{k=1}^{n^*} \lambda_k (\tilde{f}_{K_{R+1}}^M(x_k) + \lambda|x_k|^2)$$

1045 for some  $2 \leq n^* \leq n + 1$ ,  $\lambda_k > 0$ ,  $x_k \in K_{R+1}$ ,  $k = 1, 2, \dots, n^*$ , with  $\sum_{k=1}^{n^*} \lambda_k = 1$  and  $\sum_{k=1}^{n^*} \lambda_k x_k = 0$ . Now if  
 1046  $x_k \in K$  for each  $1 \leq k \leq n^*$ , then  $\tilde{f}_{K_{R+1}}^M(x_k) = f_K^M(x_k)$ , and hence  $C_\lambda^l(\tilde{f}_{K_{R+1}}^M)(0) = C_\lambda^l(f_K^M)(0)$ . So suppose, for  
 1047 contradiction, that  $x_{k_0} \in K_{R+1} \setminus K = B^c(0; R + 1)$ . Then there exists an affine function  $\ell$  such that

$$1048 \quad \ell(y) \leq \tilde{f}_{K_{R+1}}^M(y) + \lambda|y|^2 \text{ for all } y \in \mathbb{R}^n, \quad \ell(x_k) = \tilde{f}_{K_{R+1}}^M(x_k) + \lambda|x_k|^2, \quad 1 \leq k \leq n^*,$$

1049 so that

$$1050 \quad \ell(x_{k_0}) = \tilde{f}_{K_{R+1}}^M(x_{k_0}) + \lambda|x_{k_0}|^2 = a_m + 1 + \lambda|x_{k_0}|^2.$$

1051 Since  $\tilde{f}_{K_{R+1}}^M(y) = a_m + 1$  for all  $y \in B^c(0, R+1)$ ,  $\ell$  must be the unique tangent plane to the function  $y \rightarrow a_m + 1 + \lambda|y|^2$   
1052 at  $y = x_{k_0}$ , namely

$$1053 \quad \ell(y) = a_m + 1 + \lambda|x_{k_0}|^2 + 2\lambda x_{k_0} \cdot (y - x_{k_0}), \quad y \in \mathbb{R}^n.$$

1054 Now it follows from the fact that this plane does not touch the graph of  $y \rightarrow a_m + 1 + \lambda|y|^2$  at any other point  
1055 that  $x_k \notin B^c(0, R+1)$  for  $1 \leq k \leq n^*$ ,  $k \neq k_0$ , and hence, since  $n^* \geq 2$ , there must exist  $x_{\hat{k}}$ ,  $\hat{k} \neq k_0$ , with  $x_{\hat{k}} \in \Gamma_{a_j}$   
1056 for some  $1 \leq j \leq m$  and  $\ell(x_{\hat{k}}) = \tilde{f}_{K_{R+1}}^M(x_{\hat{k}}) + \lambda|x_{\hat{k}}|^2 = a_j + \lambda|x_{\hat{k}}|^2$ . But then

$$1057 \quad a_m + 1 + \lambda|x_{k_0}|^2 + 2\lambda x_{k_0} \cdot x_{\hat{k}} - 2\lambda|x_{k_0}|^2 = a_j + \lambda|x_{\hat{k}}|^2,$$

1058 and hence, since  $x_{k_0} \in B^c(0; R+1)$  and  $x_{\hat{k}} \in B(0, R)$ ,

$$1059 \quad a_m - a_j + 1 = \lambda(|x_{\hat{k}}|^2 - 2x_{k_0} \cdot x_{\hat{k}} + |x_{k_0}|^2) = \lambda|x_{\hat{k}} - x_{k_0}|^2 > \lambda,$$

1060 which contradicts the assumption on  $\lambda$ . Likewise,  $C_\lambda^u(\tilde{f}_{K_{R+1}}^{-M})(0) = C_\lambda^u(\tilde{f}_K^{-M})(0)$ , and hence  $A_\lambda^M(\tilde{f}_{K_{R+1}})(0) =$   
1061  $A_\lambda^M(f_K)(0)$ , as required.

1062 (ii): The proof of the Lipschitz case follows similar arguments. □

1063 *Proof. (Theorem 4.1)* Similar to the proof of Theorem 3.1(i), we fix  $x_{j_0} \in K$  and let  $f_\lambda(x) = \lambda|x - x_{j_0}|^2 -$   
1064  $f_K^{-M}(x)$ . Define  $\ell(x) = -f(x_{j_0})$  for all  $x \in \mathbb{R}^n$ . Then  $\ell$  is a constant function, so is affine. Clearly  $\ell(x_{j_0}) = f_\lambda(x_{j_0})$ .  
1065 We need to prove that

$$1066 \quad (8.13) \quad \ell(x) \leq f_\lambda(x)$$

1067 for all  $x \in \mathbb{R}^n$  so that  $\text{co}[f_\lambda](x_{j_0}) = \ell(x_{j_0}) = -f(x_{j_0})$ , hence  $C_\lambda^u(f_K^{-M})(x_{j_0}) = f(x_{j_0})$ . Inequality (8.13) is equivalent  
1068 to

$$1069 \quad -f(x_{j_0}) \leq \lambda|x - x_{j_0}|^2 - f_K^{-M}(x), \quad x \in \mathbb{R}^n.$$

1070 If  $x \in \mathbb{R}^n \setminus K$ ,  $f_K^M(x) = -M$ . Since  $-f(x_{j_0}) < M < \lambda|x - x_{j_0}|^2 + M$ , we clearly have  $\ell(x) \leq f_\lambda(x)$  for all  
1071  $x \in \mathbb{R}^n \setminus K$ . If  $x_j \in K$  and  $x_j \neq x_{j_0}$ , we need to prove that

$$1072 \quad -f(x_{j_0}) \leq \lambda|x_j - x_{j_0}|^2 - f(x_j), \quad \text{or equivalently,} \quad f(x_j) - f(x_{j_0}) \leq \lambda|x_j - x_{j_0}|^2.$$

1073 Since  $\alpha = \min\{|x_i - x_j|, x_i, x_j \in K, x_i \neq x_j\}$ , then if  $\lambda > L/\alpha$ , we have

$$1074 \quad f(x_j) - f(x_{j_0}) \leq L|x_j - x_{j_0}| \leq \lambda\alpha|x_j - x_{j_0}| \leq \lambda|x_j - x_{j_0}|^2,$$

1075 which completes the proof. □

1076 *Proof. (Lemma 4.3)* We may write  $\ell_s(x) = a \cdot x + b$  with  $a \in \mathbb{R}^n$  and  $b \in \mathbb{R}$ . We see that  $D\ell_s(x) = a$  and we  
1077 need to give an estimate of  $|a|$ . Since we have  $\ell_s(x_i) = f_S(x_i)$  and  $|\ell_s(x_i) - \ell_s(x_1)| = |f_S(x_i) - f_S(x_1)| \leq L|x_i - x_1|$ ,  
1078 we see that  $|a \cdot (x_i - x_1)| \leq L|x_i - x_1|$  for  $i = 1, 2, \dots, k$ . As  $\dim(\text{co}[S]) = n$ , there are at least  $n$ -vectors, say  
1079  $\{x_2 - x_1, \dots, x_{n+1} - x_1\}$ , which are linearly independent and hence form a basis of  $\mathbb{R}^n$ . If we let  $\{e_1, \dots, e_n\}$  be  
1080 any orthonormal basis of  $\mathbb{R}^n$ , there is an  $n \times n$  invertible matrix  $A = (a_{ij})_{i,j=1}^n$  such that  $e_i = \sum_{j=1}^n a_{ij}(x_{j+1} - x_1)$ .  
1081 Hence

$$1082 \quad |a \cdot e_i| \leq \sum_{j=1}^n |a_{ij}| |a \cdot (x_{j+1} - x_1)| \leq L \left( \sum_{j=1}^n |a_{ij}|^2 \right)^{1/2} \left( \sum_{j=1}^n |x_{j+1} - x_1|^2 \right)^{1/2}.$$

1083 Therefore, the Euclidean norm of  $a$  satisfies  $|a| \leq L|A|(\sum_{j=1}^n |x_i - x_0|^2)^{1/2}$ , where  $|A|$  denotes the Frobenius norm  
1084 of the matrix  $A$ , and can then take  $C_s = |A|(\sum_{j=1}^n |x_i - x_0|^2)^{1/2}$ , which completes the proof. □

1085 *Proof.* (**Theorem 4.5**) We prove the result for the upper transform. The proof of the lower transform follows  
 1086 similar arguments.

1087 Let us consider the affine function  $\lambda r_s^2 - \ell_s(x)$ . For  $x \in S$ , clearly

$$1088 \quad (8.14) \quad \lambda r_s^2 - \ell_s(x) = \lambda r_s^2 - f_K(x) = \lambda|x - x_s|^2 - f_K^{-M}(x).$$

1089 If we can show that  $\lambda r_s^2 - \ell_s(x) < \lambda|x - x_s|^2 - f_K^{-M}(x)$  for  $x \in \mathbb{R}^n \setminus S$ , then one obtains

$$1090 \quad (8.15) \quad \text{co}[\lambda|\cdot - x_s|^2 - f_K^{-M}](x) = \lambda r_s^2 - \ell_s(x)$$

1091 for  $x \in \text{co}[S]$  and the proof for the upper transform then follows.

1092 We consider two different cases: (i)  $x \in K \setminus S$  and (ii)  $x \in \mathbb{R}^n \setminus K$ .

1093 For the case (i), let  $x \in K \setminus S$ . We need then to prove that

$$1094 \quad (8.16) \quad \lambda r_s^2 - \ell_s(x) < \lambda|x - x_s|^2 - f_K(x),$$

1095 or, equivalently, that

$$1096 \quad (8.17) \quad \lambda r_s^2 - \ell_s(x) + f_K(x) < \lambda|x - x_s|^2.$$

1097 We have the following estimates for the left hand side of (8.17).

$$1098 \quad (8.18) \quad \begin{aligned} \lambda r_s^2 - \ell_s(x) + f_K(x) &\leq \lambda r_s^2 + |\ell_s(x) - \ell_s(x_s)| + |\ell_s(x_s)| + A_0 \\ &\leq \lambda r_s^2 + C_s L|x - x_s| + C_s Lr_s + 2A_0. \end{aligned}$$

1099 We have used the fact that for any  $x^* \in S$ ,

$$1100 \quad (8.19) \quad |\ell_s(x_s)| \leq |\ell_s(x_s) - \ell_s(x^*)| + |\ell_s(x^*)| \leq C_s Lr_s + A_0$$

1101 as  $\ell_s(x^*) = f_K(x^*)$ . Therefore (8.17) holds if

$$1102 \quad (8.20) \quad \lambda r_s^2 + C_s L|x - x_s| + C_s Lr_s + 2A_0 < \lambda|x - x_s|^2.$$

1103 Note that  $|x - x_s| \geq r_s + \sigma_s$ . Let us consider the function

$$1104 \quad (8.21) \quad g(t) = \lambda t^2 - \lambda r_s^2 - C_s L t - C_s L r_s - 2A_0.$$

1105 If we can find conditions for  $\lambda$  such that  $g(r_s + \sigma_s) > 0$  and  $g'(t) > 0$  when  $t \geq r_s + \sigma_s$ , then (8.20) holds and (8.17)  
 1106 will be satisfied.

1107 We see that  $g(r_s + \sigma_s) > 0$  is equivalent to

$$1108 \quad (8.22) \quad \lambda[(r_s + \sigma_s)^2 - r_s^2] > C_s L(2r_s + \sigma_s) + 2A_0.$$

1109 This last inequality is equivalent to (4.2). Thus (8.17) holds and thus  $g(r_s + \sigma_s) > 0$ .

1110 Next we have  $g'(t) = 2\lambda t - C_s L$ . Since  $g'(t)$  itself is an increasing function, we only need to show that  $g'(r_s + \sigma_s) > 0$ ,  
 1111 which is equivalent to

$$1112 \quad (8.23) \quad \lambda > \frac{C_s L}{2(r_s + \sigma_s)},$$

1113 which follows from (4.2). This completes the proof for case (i).

1114

1115 (ii): Let  $x \in \mathbb{R}^n \setminus K$ , hence  $-f_K^{-M}(x) = M$ . We need to prove that

$$1116 \quad (8.24) \quad \lambda r_s^2 - \ell_s(x) < \lambda|x - x_s|^2 + M.$$

1117 Again we have

$$1118 \quad (8.25) \quad \lambda r_s^2 - \ell_s(x) \leq \lambda r_s^2 + C_s L|x - x_s| + C_s L r_s + A_0.$$

1119 Therefore we prove (ii) if

$$1120 \quad (8.26) \quad \lambda r_s^2 + C_s L|x - x_s| + C_s L r_s + A_0 < \lambda|x - x_s|^2 + M.$$

1121 Since (4.2) is satisfied, then by inspection it is easy to verify that (8.26) holds for all non-negative numbers  
1122  $|x - x_s| \geq 0$ , which completes the proof.  $\square$

1123 *Proof. (Lemma 4.9) (i):* We see that both  $p_+$  and  $p_-$  are well-defined functions in  $D$  and clearly  $p_-(x) \leq v \leq$   
1124  $p_+(x)$  for every  $(x, v) \in \text{co}[\Gamma_s]$ . It is also easy to see that the two different expressions for  $p_+(x)$  and respectively  
1125 for  $p_-(x)$  are equal.  
1126

1127 (ii): Since  $\text{co}[\Gamma_s]$  is a convex polytope, we have, for any  $x_1, x_2 \in D$  and for every  $0 < t < 1$ , that

$$1128 \quad t(x_1, p_+(x_1)) + (1-t)(x_2, p_+(x_2)) = (tx_1 + (1-t)x_2, tp_+(x_1) + (1-t)p_+(x_2)) \in \text{co}(\Gamma_s)$$

1129 as both  $D$  and  $\text{co}[\Gamma_s]$  are convex. Furthermore, by definition of  $p_+$ ,  $tp_+(x_1) + (1-t)p_+(x_2) \leq p_+(tx_1 + (1-t)x_2)$ .  
1130 Thus  $p_+$  is concave in  $D$ , hence is continuous in  $D$ . Similarly we can show that  $p_-$  is convex, hence continuous in  
1131  $D$ . Also  $p_+$  and  $p_-$  are both piecewise affine functions. In fact, since  $\text{co}[\Gamma_s]$  is a convex polytope,  $\text{co}[\Gamma_s]$  has finitely  
1132 many closed  $n$ -dimensional faces. We may write  $\partial \text{co}[\Gamma_s] = \Gamma_+ \cup \Gamma_- \cup \Gamma_0$ , where  $\Gamma_+ = \cup_{k=1}^m F_k^+$ ,  $\Gamma_- = \cup_{j=1}^l F_j^-$   
1133 and  $\Gamma_0 = \cup_{r=1}^s F_r^0$  with  $F_k^+$ ,  $F_j^-$  and  $F_r^0$   $n$ -faces of  $\text{co}[\Gamma_s]$ . For  $F_k^+$ , there is an affine function  $\ell_k^+ : \mathbb{R}^n \rightarrow \mathbb{R}$  such  
1134 that  $\ell_k^+(x) = v$  if  $(x, v) \in F_k^+$  and  $\ell_k^+(x) > v$  if  $(x, v) \in \text{co}[\Gamma_s] \setminus (F_k^+)$ . Similarly, for  $F_j^-$ , there is an affine function  
1135  $\ell_j^- : \mathbb{R}^n \rightarrow \mathbb{R}$  such that  $\ell_j^-(x) = v$  if  $(x, v) \in F_j^-$  and  $\ell_j^-(x) < v$  if  $(x, v) \in \text{co}[\Gamma_s] \setminus (F_j^-)$ . Every  $F_r^0$  is an  $n$ -face  
1136 whose normal vectors are in  $\mathbb{R}^n \times \{0\} \subset \mathbb{R}^n \times \mathbb{R}$ , that is,  $F_r^0$  is perpendicular to  $D \times \{0\}$ . Since the vertices of each  
1137  $F_k^+$  are extreme points of  $\text{co}[\Gamma_s]$  and every point  $x \in S$  is an extreme point of  $\text{co}[S]$  we see that for every extreme  
1138 point  $(x, v)$  of  $\text{co}[\Gamma_s]$ ,  $x$  is an extreme point of  $D$ . Let  $D_k^+ = P_{\mathbb{R}^n}(F_k^+)$  be the orthogonal projection from  $F_k^+$  to  $\mathbb{R}^n$ ,  
1139 then  $D_k^+$  is a convex polytope contained in  $D$  whose vertices are all in  $S$ . The projection  $P_{\mathbb{R}^n}$  also maps relative  
1140 boundary of  $F_k^+$  to boundary of  $D_k^+$ , and the relative interior  $F_k^+$  to interior of  $D_k^+$ . Also on  $D_k^+$ ,  $p_+(x) = \ell_k^+(x)$ .  
1141 Thus  $p_+(\cdot)$  is affine on  $D_k^+$ .

1142 Similarly, for each  $F_j^-$ , we define  $D_j^- = P_{\mathbb{R}^n}(F_j^-)$ . Then the vertices of  $D_j^-$  belong to  $S$  and  $p_-(x) := \ell_j^-(x)$  is  
1143 affine on  $D_j^-$ .  
1144

1145 (iii): It is easy to see that  $\hat{D}_k^+ \cap \hat{D}_j^+ = \emptyset$  and  $\hat{D}_k^- \cap \hat{D}_j^- = \emptyset$  for  $k \neq j$ . Next we show that  $D = \cup_{k=1}^m D_k^+ = \cup_{j=1}^l D_j^-$ .

1146 If  $\cup_{k=1}^m D_k^+ \neq D$ , there is an interior point  $x \in D \setminus \cup_{k=1}^m D_k^+$ . By definition  $(x, p_+(x)) \in \partial \text{co}[\Gamma_s]$  and we may  
1147 assume that  $(x, p_+(x))$  lies in the relative interior of an  $n$ -face  $F \subset \partial \text{co}[\Gamma_s]$ . If  $F$  is one of the  $F_j^-$ 's, this implies  
1148  $p_+(x) = p_-(x)$ . This cannot happen inside  $D$ . If  $F$  is one of the  $F_r^0$ 's, then  $D_r^0 := P_{\mathbb{R}^n}(F_r^0)$  is an  $n-1$ -dimensional  
1149 polytope. If  $E$  is the  $(n-1)$ -dimensional plane in  $\mathbb{R}^n$  containing  $D_r^0$ , then  $D$  must lie on one side of  $D_r^0$ . Therefore  
1150  $D_r^0 \subset \partial D$ , hence  $x$  is a boundary point of  $D$ . This contradicts our assumption that  $x$  is an interior point of  $D$ .  
1151 Thus  $D = \cup_{k=1}^m D_k^+$ . Similarly, we can show that  $D = \cup_{j=1}^l D_j^-$ .

1152 The other conclusions also follow from the above arguments.  $\square$

1153 *Proof.* (Theorem 4.11) Since  $\text{co}[S] = \cup_{k=1}^m D_k^+$  and on each  $D_k^+$ , there is an affine function  $\ell_k^+ : \mathbb{R}^n \rightarrow \mathbb{R}$  such  
 1154 that  $\ell_k^+(x) = p_k^+(x)$  for  $x \in D_k^+$  and  $\ell_k^+(x) > f_K(x)$  for  $x \in S_k^+$ , where  $S_k^+$  is the set of extreme points of  $D_k^+$  given by  
 1155 Lemma 4.9 which is a subset of  $S$ . Let  $C_k^+ > 0$  be the constant given by Lemma 4.3 so that  $|D\ell_k^+(x)| < C_k^+ L \leq C_s L$ .

1156 If we can show that  $\text{co}[\lambda|\cdot - x_s|^2 - f_K^{-M}] = \lambda r_s^2 - \ell_k^+(x)$  for  $x \in D_k^+$ , the proof is finished. As in the proof of  
 1157 Theorem 4.5, we have to consider different cases. If  $x \in \mathbb{R}^n$  or  $x \in \mathbb{R}^n \setminus K$  or  $x \in K \setminus S$ , the proof for the inequality  
 1158  $\lambda r_s^2 - \ell_k^+(x) \leq \lambda|x - x_s|^2 - f_K^{-M}(x)$  is the same as that in the proof of Theorem 4.5. The only new case we have to  
 1159 consider is for  $x \in S \setminus S_k^+$ .

1160 But for  $x \in S \setminus S_k^+$ , the above inequality is

$$1161 \quad (8.27) \quad \lambda r_s^2 - \ell_k^+(x) \leq \lambda|x - x_s|^2 - f_K(x) = \lambda r_s^2 - f_K(x),$$

1162 which is equivalent to  $\ell_k^+(x) \geq f_K(x)$  as  $S \subset \partial B(x_s; r_s)$ . We also know from Lemma 4.9 that  $\ell_k^+(x) > f_K(x)$  for  
 1163  $x \in S \setminus S_k^+$ . Therefore on each  $D_k^+$ , (8.27) holds as  $p_+(x) = \ell_k^+(x)$  on  $D_k^+$ . The proof for the lower transform is  
 1164 similar. The proof is finished.  $\square$

1165 *Proof.* (Corollary 5.4) For the proof of this result, we first follow the proof of Theorem 2.5 so that the points  
 1166  $x^i$ 's for the convex envelope are in  $\bar{\Omega}$ . Then we follow the proof of [55, Theorem 3.7] to show that  $x^i$ 's can only be  
 1167 in  $K$ . The rest of the proof then follows from that of Theorem 2.5.  $\square$

1168 **Acknowledgements.** The authors are extremely grateful to the anonymous referees, whose constructive  
 1169 comments on earlier versions of the manuscript have contributed to produce a better version of the paper. The  
 1170 authors would also like to thank the Isaac Newton Institute for Mathematical Sciences for support and hospitality  
 1171 during the programme 'Variational methods and effective algorithms for imaging and vision' when part of the work  
 1172 on this paper was undertaken. This work was partially supported by EPSRC Grant Number EP/K032208/1. KZ  
 1173 wishes then to thank The University of Nottingham for its support, whereas EC is grateful for the financial support  
 1174 of the College of Science, Swansea University, and AO acknowledges the partial financial support of the Argentinian  
 1175 Research Council (CONICET) through the project PIP 11220170100100CO, the National University of Tucumán  
 1176 through the project PIUNT CX-E625 and the FonCyT through the project PICT 2016 201-0105 Prestamo Bid.  
 1177 The authors finally would like to thank Simone Parisotto for delight discussions on the numerical simulations of  
 1178 surface reconstructions from real data.

1179

## REFERENCES

- 1180 [1] Srtm and landcover download site. <http://rmd.neoknet.com/srtm1/>. Accessed: 2018-05-04.  
 1181 [2] A. ALMANSA, F. CAO, Y. GOUSSEAU, AND B. ROUGÉ, Interpolation of digital elevation models using AMLE and related methods,  
 1182 IEEE Trans. Geoscience and Remote Sensing, 40 (2002), pp. 314–325.  
 1183 [3] L. AMBROSIO, N. FUSCO, AND D. PALLARA, Functions of Bounded Variation and Free Discontinuity Problems, Clarendon Press,  
 1184 UK, 2000.  
 1185 [4] F. ANDREU, C. BALLESTER, V. CASELLES, AND J. M. MAZÓN, The Dirichlet problem for the total variation flow, J. Functional  
 1186 Anal., 180 (2001), pp. 347–403.  
 1187 [5] G. ARONSSON, Extension of functions satisfying Lipschitz conditions, Ark. Math., 6 (1967), pp. 551–561.  
 1188 [6] Z. BELHACHMI, D. BUCUR, B. BURGETH, AND J. WEICKERT, How to choose interpolation data in images, SIAM J. Appl. Math.,  
 1189 70 (2009), pp. 333–352.  
 1190 [7] G. BELLETTINI, V. CASELLES, AND M. NOVAGA, The total variation flow in  $\mathbb{R}^N$ , J. Diff. Equations, 184 (2002), pp. 475–525.  
 1191 [8] M. BERTALMIO, G. SAPIRO, V. CASELLES, AND C. BALLESTER, Image inpainting, in SIG-GRAPH, 2000.  
 1192 [9] M. BILDHAUER, M. FUCHS, AND J. WEICKERT, Denosing and inpainting of images using TV-type energies: Theoretical and  
 1193 computational aspects., Journal of Mathematical Science, 219 (2016), pp. 899–910.  
 1194 [10] K. BREDIES, K. KUNISCH, AND T. POCK, Total generalized variation, SIAM J. Imaging Science, 3 (2010), pp. 492–526.  
 1195 [11] M. D. BUHMANN, Radial Basis Functions, Cambridge Univ. Press, UK, 2004.  
 1196 [12] J. CAI, R. CHAN, AND B. MORINI, Minimization of an edge-preserving regularization functional by conjugate gradient type  
 1197 methods, in Image Processing Based on Partial Differential Equations, X. Tai, K. Lie, T. F. Chan, and S. Osher, eds.,  
 1198 Springer, 2005, pp. 109–122.  
 1199 [13] V. CASELLES, J. MOREL, AND C. SBERT, An axiomatic approach to image interpolation, IEEE Trans. Image Processing, 7 (1998),  
 1200 pp. 376–386.

- 1201 [14] R. H. CHAN, C.-W. HO, AND M. NIKOLOVA, Salt-and-pepper noise removal by median-type noise detectors and detail-preserving  
1202 regularization, IEEE Trans. Image Processing, 14 (2005), pp. 1479–1485.
- 1203 [15] T. F. CHAN AND S. H. KANG, Error analysis for image inpainting, J. Math. Imag. Vis., 26 (2006), pp. 85–103.
- 1204 [16] T. F. CHAN AND J. SHEN, Nontexture inpainting by curvature-driven diffusions, J. Vis. Commun. Image Represent., 12 (2001),  
1205 pp. 436–449.
- 1206 [17] T. F. CHAN AND J. SHEN, Image Processing and Analysis: Variational, PDE, Wavelet, and Stochastic Methods, SIAM, USA,  
1207 2005.
- 1208 [18] M. DEBERG, M. VANKREVELD, M. OVERMARS, AND O. SCHWARZKOPF, Computational Geometry, Springer-Verlag, Berlin, Ger-  
1209 many, 2nd ed., 2000.
- 1210 [19] R. A. DEVORE AND G. G. LORENTZ, Constructive Approximation, Springer-Verlag, Berlin, Germany, 1993.
- 1211 [20] J. DUCHON, Interpolation des fonctions de deux variables suivant le principe de la flexion des plaques minces, R.A.I.R.O. Analyse  
1212 Numérique, 10 (1976), pp. 5–12.
- 1213 [21] J. DUGUNDJI, Topology, Allyn and Bacon, USA, 1970.
- 1214 [22] H. EDELSBRUNNER, Algorithms in Combinatorial Geometry, Springer-Verlag, Berlin, Germany, 1987.
- 1215 [23] G. E. FASSHAUER, Meshfree Approximation Methods with Matlab, World Scientific Press, Singapore, 2007.
- 1216 [24] H. FEDERER, Geometric Measure Theory, Springer Verlag, Berlin, Germany, 1969.
- 1217 [25] R. FRANKE, A critical comparison of some methods for interpolation of scattered data. Naval Postgraduate School, TR NPS-53-  
1218 79-003, 1979.
- 1219 [26] R. FRANKE, Scattered data interpolation: Tests of some methods, Mathematics of Computation, 38 (1982), pp. 181–200.
- 1220 [27] D. GESCH, G. EVANS, J. MAUCK, J. HUTCHINSON, AND W. CARSWELL JR, The national map elevation. U.S. Geological Survey  
1221 Fact Sheet 3053, 2009.
- 1222 [28] P. GETREUER, Contour stencils: Total variation along curves for adaptive image interpolation, SIAM J. Imaging Science, 4 (2011),  
1223 pp. 954–979.
- 1224 [29] P. GETREUER, Total variation inpainting using Split Bregman, Image Processing On Line, 2 (2012), pp. 147–157.
- 1225 [30] M. GIAQUINTA, G. MODICA, AND J. SOUCEK, Functionals with linear growth in the calculus of variations I, Comment. Math.  
1226 Univ. Carolinae, 20 (1979), pp. 143–156.
- 1227 [31] E. GIUSTI, Minimal Surfaces and Functions of Bounded Variation, Birkhäuser Verlag, Switzerland, 1984.
- 1228 [32] P. HENRICI, Discrete Variable Methods in Ordinary Differential Equations, John Wiley & Sons, USA, 1967.
- 1229 [33] J.-B. HIRIART-URRUTY AND C. LEMARÉCHAL, Fundamentals of Convex Analysis, Springer-Verlag, Berlin, Germany, 2001.
- 1230 [34] R. JENSEN, Uniqueness of Lipschitz extensions: Minimizing the Sup norm of the gradient, Arch. Rational Mech. Anal., 123  
1231 (1993), pp. 51–74.
- 1232 [35] J. LELLMANN, J. MOREL, AND C. SCHÖNLIEB, Anisotropic third-order regularization for sparse digital elevation models, in Scale  
1233 Space and Variational Methods in Computer Vision, A. Kuijper, K. Bredies, T. Pock, and H. Bischof, eds., Berlin, Heidelberg,  
1234 2013, Springer Berlin Heidelberg, pp. 161–173.
- 1235 [36] S. LODHA AND R. FRANKE, Scattered data techniques for surfaces, in Scientific Visualization, G. Nielson, H. Hagen, and F. Post,  
1236 eds., vol. 18, Dagstuhl '97, 1999, IEEE Computer Society Press, pp. 181–222.
- 1237 [37] A. OBERMAN, The convex envelope is the solution of a nonlinear obstacle problem, Proc. Amer. Math. Soc., 135 (2007), pp. 1689–  
1238 1694.
- 1239 [38] A. OKABE, B. BOOTS, K. SUGIHARA, AND S. N. CHIU, Spatial Tessellations, John Wiley & Sons, UK, 2nd ed., 2000.
- 1240 [39] S. PARISOTTO AND B. SCHÖNLIEB, Matlab codes for the Image Inpainting Problem. GitHub repository, MATLAB Central File  
1241 Exchange, September 2016.
- 1242 [40] M. J. D. POWELL, Approximation Theory and Methods, Cambridge University Press, USA, 1981.
- 1243 [41] R. T. ROCKAFELLAR, Convex Analysis, Princeton University Press, USA, 1970.
- 1244 [42] L. RUDIN, S. OSHER, AND E. FATEMI, Nonlinear total variation based noise removal algorithms, Physica D, 60 (1992), pp. 259–268.
- 1245 [43] G. SAPIRO, Geometric Partial Differential Equations and Image Analysis, Cambridge University Press, New York, USA, 2001.
- 1246 [44] O. SAVIN, C1 regularity for infinity harmonic functions in two dimensions, Arch. Ration. Mech. Anal., 176 (2005), pp. 351–361.
- 1247 [45] C. SCHÖNLIEB, Partial Differential Equation Methods for Image Inpainting, Cambridge University Press, USA, 2015.
- 1248 [46] P. SOILLE, Spatial distributions from contour lines: An efficient methodology based on distance transformations, Journal of Visual  
1249 Communication and Image Representation, 2 (1991), pp. 138–150.
- 1250 [47] M. L. STEIN, Interpolation of Spatial Data: Some Theory for Kriging, Springer-Verlag, USA, 1999.
- 1251 [48] L. N. TREFETHEN, Spectral Methods in MATLAB, SIAM, Society for Industrial and Applied Mathematics, USA, 2000.
- 1252 [49] L. N. TREFETHEN, Approximation Theory and Approximation Practice, SIAM, Society for Industrial and Applied Mathematics,  
1253 USA, 2013.
- 1254 [50] J. WEICKERT, Anisotropic Diffusion in Image Processing, B.G. Teubner, Germany, 1998.
- 1255 [51] H. WENDLAND, Scattered Data Approximation, Cambridge University Press, USA, 2005.
- 1256 [52] K. ZHANG, Compensated convexity and its applications, Anal. Nonlin. H. Poincaré Inst, 25 (2008), pp. 743–771.
- 1257 [53] K. ZHANG, E. CROOKS, AND A. ORLANDO, Compensated convexity transforms and numerical algorithms. In preparation.
- 1258 [54] K. ZHANG, E. CROOKS, AND A. ORLANDO, Compensated convexity, multiscale medial axis maps and sharp regularity of the  
1259 squared distance function, SIAM J. Math. Anal., 47 (2015), pp. 4289–4331.
- 1260 [55] K. ZHANG, E. CROOKS, AND A. ORLANDO, Compensated convexity methods for approximations and interpolations of sampled  
1261 functions in euclidean spaces: Theoretical foundations, SIAM J. Math. Anal., 48 (2016), pp. 4126–4154.
- 1262 [56] K. ZHANG, A. ORLANDO, AND E. CROOKS, Compensated convexity and Hausdorff stable extraction of intersections for smooth

- 1263 manifolds, Math. Models Methods Appl. Sci., 25 (2015), pp. 839–873.  
1264 [57] K. ZHANG, A. ORLANDO, AND E. CROOKS, Compensated convexity and Hausdorff stable geometric singularity extractions, Math.  
1265 Models Methods Appl. Sci., 25 (2015), pp. 747–801.